The effect of surface structure on the optical and electronic properties of nanomaterials

Trevor David Hull

Submitted in partial fulfillment of the

requirements for the degree

of Doctor of Philosophy

in the Graduate School of Arts and Science

COLUMBIA UNIVERSITY

2019

ABSTRACT

The effect of surface structure on the optical and electronic properties of nanomaterials

Trevor D. Hull

Surface passivation of semiconductor quantum dots is essential to preserve their efficient and robust light emitting properties. By using a lattice matched (mismatch = 0.5%) lead halide perovskite matrix, we achieve shell-like passivation of lead sulfide QDs in crystalline films, leading to efficient infrared light emission. These structures are made from a simple one-step spin coating process of an electrostatically stabilized colloidal suspension. Photoluminescence and transient absorption spectroscopy indicate rapid energy transfer between the perovskite matrix and the QDs, suggesting an interface with few trap states. In addition to housing the efficient infrared QD emitters, lead halide perovskites themselves have good carrier mobilities and low trap densities, making these solution-processable heterostructures an attractive option for electrically pumped light emitting devices.

The highest performing quantum dots for visible light applications are CdE (E=chalcogenide) core/shell heterostructures. Again, surface passivation plays a huge role in determining the brightness and robustness of visible QD emitters. Multilayer shell passivation is usually used to produce the highest quantum yield particles. Surface trap states are shown to be detrimental to luminescence output, even in thick-shelled particles. Spherical quantum wells allow for thicker shells and with good surface passivation, show promising reduction of biexciton auger recombination, as measured by a time correlated single photon counting (TCSPC) microscope. TCSPC methods were used to diagnose and identify QD architectures for LED applications and explore fundamental recombination dynamics using photon antibunching measurements, and statistical analysis of blinking traces.

Introducing new surfaces onto graphitic substrates can be a useful for introducing new electronic properties, patterning device-specific geometries, or appending molecular catalysts. Metal nanoparticles were used to act as a catalyst for the gasification and etching of graphite and graphene. Several methods of controlling the initiation, propagation, and density of these trenches were explored. Patterning defects helped control where initiation occurred, while faceting existing defect sites could also enable more facile initiation and control the direction at the beginning of etching, due to the wetting mechanism of particle movement. Patterning the metal also was shown as a promising avenue to limit unwanted gasification and promote etching in specific, patterned regions. Surface functionalization using reactive gases was performed and characterized with outlook for future experiments.

TABLE OF CONTENTS

Acknowledgements

My time spent at Columbia was, begrudgingly, a period of learning and growth, in many unexpected ways. It is difficult to prepare for big life experiences, even when smart people tell you exactly what to expect.

Without getting too sentimental, I'd like to thank and acknowledge the contributions that many have made to help me across the finish line. I would not be the person I am, for better or worse, without this not-quite-exhaustive list of colleagues, collaborators, and mentors. First, to everyone who gave me good advice I did not listen to, thank you for trying.

Thank you to my advisor, Professor Jon Owen, for teaching me how to think deeply and critically about science, pushing me to produce and communicate the best version of my work, and ensuring the surplus value produced by my labor was compensated with wages. Thank you for believing in me and letting me work on unique and exciting projects. I will always have your voice in my head making sure I'm careful about science.

Thank you to my colleagues in the Owen lab, who made the long hours distilling octadecene more tolerable. I joined the lab at the same time as Albanian superstar Iva Rrëza, and we've been through all the ups and downs of the program together. I can't imagine I would've made it through without your insights, sympathy, and straight-talk. You are brilliant and passionate, and I'm excited to see what your future holds.

Dr. Octavi Semonin has perhaps done more than anyone in shaping the way I approach problems, scientific and otherwise. I enjoyed getting to know him personally, and learning from him. The PbS/perovskite project doesn't happen without Tavi. You are a role model, mentor, and friend. Dr. Ilan Jen-La Plante was another terrific example to young scientist Trevor, and

someone who directly contributed to my ability to tackle scientific and life challenges. Her positive attitude and bright outlook helped science seem more fun. These two taught me how to be a cool, young, smart, urban professional and I'm happy to say I'm now cooler than they are (not actually true).

Zachariah Norman was a patient teacher, despite his best efforts to make everyone think otherwise, he has a kind soul. Mark Hendricks was always thinking two steps ahead, but was still ready to advise younger students. Not many people have the combination of charisma and scientific chops as Alex Beecher, despite his record of abysmal opinions in the New York Times. Michael Campos and Peter Chen taught me more than memes, I'm sure, but I can't think of anything in particular right now. My worldview of the nanocrystal field - its chemistry, physics, and personalities - comes largely from them. As did some great metal recommendations and lessons in ping pong ball aerodynamics.

When I first arrived in New York, Leslie Hamachi was immediately friendly and helpful, easing my transition from rocky-mountain-boy to city-slicker. That kindness never left, and she was always willing to help with advice in lab. She was one of the hardest working scientists I've ever seen. I've shared laughter with Matthew Greenberg, has one of the most unique minds I have ever met. I promise I mean that in a good way, and seeing the scientific process unravel at the same speed as jokes about was a pleasure. Natalie Saenz has brought a cheerfulness to the lab that it has not seen before and likely will never see again. I hope your excitement for science is not diminished over the course of your Ph.D. Anindya Swarnakar was great fume hood partner, a talented singer, and a methodical scientist.

Brandon and Ellie will get separate paragraphs because I refuse to contribute to their co-dependence. The lab is in good hands, and I hope you two have learned more than cynicism from me.

Brandon McMurtry is a fine scientist and always brings those delicious chocolate covered macadamia nuts back from Hawaii, really just a top-10 guy. He seems to tackle challenges with the same coolness he has mixing (sometimes awful) gin drinks. Keeping calm is a valuable skill in the Owen lab.

Ellie Bennett is also a fine scientist even though she has never brought me any tasty treats from Hawaii. She can easily see through distractions to the main point, always cutting to the most important pieces of information and data. Clarity is a valuable skill in the Owen lab.

Thank you to the collaborators who graciously offered their expertise. M. Tuan Trinh, Steffen Jokusch, Eric Stach, Andrew Gamalski, Corey Dean, En-Min, Olivia Ghosh, Justin Johnson.

Thank you to my friends and comrades in GWC-UAW, for teaching me grace under pressure, correct chanting cadences, and how to stand up for what's right. We will win this fight!

Lastly thank you to my family, whose love and support are instrumental to everything I've ever achieved. I am spoiled for good role models among my siblings, their partners, and their children (AKA the future). I continue to benefit from their examples of kindness, patience, and joy.

My Dad has always been a steady, calming presence in my life. Solving problems, performing backbreaking labor late into the night, driving long hours, helping others, and teaching me to integrate without a single complaint. His quiet strength is only eclipsed by his humor. I'll never in

my life be able to go on a hike without asking passersby “Is the elevator up ahead?” and I am so appreciative of every minute we’ve spent together.

My Mom treats everyone as a friend, I hope I’ve absorbed an eighth of the kindness she has in her heart. After raising 6 children she went back to school, earned a masters degree, built a library, and got elected to the Magna Metro Township council. I’m inspired by her drive to improve our community and its people, and how she’s continually seeking new knowledge (fire fighting! Inland ports! Politics!) to make the world a better place. The Trish Renaissance is exciting to watch, and is great for the people of Magna. I love you so much, and would be nothing without your love.

For Audrey, Austin, Beckham, Brady, Brynlee, Caden, Carson, Connor, Davey, David, Devon, Faith, Lisa, Maddox, Mason, Mia, Payton, Rachel, Shannan, Sydney, Tom, Tony, and Trish.

Chapter 1. Lead Sulfide Quantum Dot/Lead Halide Perovskite Heterostructures from a Single Colloidal Suspension

TABLE OF CONTENTS

1.1. Introduction

1.1.1. Electrical applications of semiconductor nanocrystals

Semiconductor nanocrystals (NCs) are ideal materials for efficient light emitting applications that require narrow line-widths and tunability[1–3]. To preserve their best optoelectronic properties, NC solids need fully-coordinated surface atoms to prevent non-radiative traps[4,5], and moderate carrier mobility to facilitate electrical pumping of the NC emitters[6]. Several approaches have been used to solve this problem, using short conductive ligands[7], encompassing PbS in CdS matrix[8], and focusing on the downconversion properties of QDs[9] instead of building electrical devices.

PbS quantum dots (QDs) are among the most studied materials, after CdE (E=chalcogenide). Nanocrystalline PbS and PbSe are tunable across a broad range of infrared wavelengths, and are synthesized at relatively mild temperatures[10,11]. One factor limiting the use of PbS in IR emitting applications is the lack of a suitable shell material. High quantum yield CdSe nanocrystals often have multiple layers of CdS and ZnS shells, which have relatively compatible crystal structures and wide bandgaps. Promising work has been done on synthesis of PbS cores with ZnS[12], and CdS shells[13,14], with varying results, however these still are limited by charge carrier injection, as discussed above. This work suggests a new method, encapsulation of PbS QDs in a conductive $CH_3NH_3PbBr_3$ matrix, developed concurrently to similar work done in the Sargent lab.[15,16]

1.1.2. Epitaxy of perovskite and Lead sulfide

The crystal structure of PbS[17] is remarkably similar to that of lead halide perovskites[18] – widely studied for photovoltaic[19], LED[20], and lasing[21] applications because of their good carrier mobility and long diffusion lengths. This makes $CH_3NH_3PbBr_3$ perovskite a good match to form

a conductive, epitaxial matrix for PbS NCs, with cubic lattice constants differing by only 0.54% (PbS = Fm3m, 5.932Å; $CH_3NH_3PbBr_3$ = Pm3m, 5.902 Å). Recent work has shown that PbS in perovskite solids have high solid state NIR PLQY[15] as well as record power conversion efficiency in an IR LED[16], however, thorough examination of the PbE – Perovskite interface, charge carrier transfer process, and cocrystal morphology requires further study.

The macroscopic epitaxy of $CH_3NH_3PbBr_3$ with PbS is demonstrated in Figure 2, an optical microscope image of edge-aligned single crystal perovskites (orange) templated by the atomic structure of the underlying PbS lattice (gray). Frames of a video of crystal growth are provided in Additional figures section, showing merging of individual crystallites with no visible defects.

Figure 1

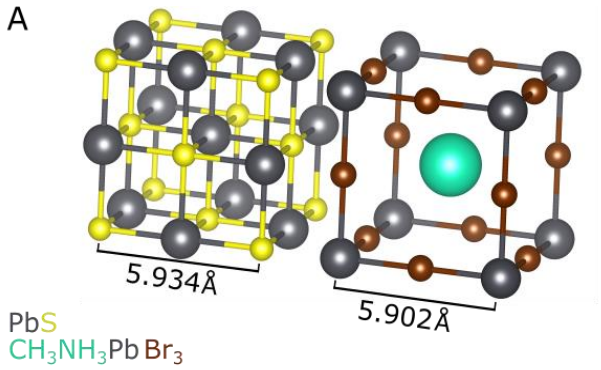

Mismatch	PbS	PbSe
$CH_3NH_3PbBr_3$	**-0.54%**	-3.7%
$CH_3NH_3PbI_3$	5.2%	2.0%
$CsPbBr_3$	-1.01%	-4.1%

Left: Crystal structure of PbS (left) and $CH_3NH_3PbBr_3$ perovskite (right) with lattice constants[1,2]. Sulfur is yellow, lead is gray, bromine is brown, and the disordered methylammonium cation is rendered as a green sphere. *Right:* Table of calculated mismatch between lead chalcogenide structures and lead halide perovskites.

PbSe was also used to template the growth of $CH_3NH_3PbI_3$ crystals (Figure 2), however, due to a difference in crystal structure (P4mm), thicker crystals, and excess yellow PbI_2 present, the alignment of crystals is less clear. Mixing of halides, (e.g. Br & I) may be use a useful

strategy for tuning the lattice structure to better match either PbS and PbSe, and has been used by Ning *et al.* [15] this may be a fruitful area for future study.

Figure 2

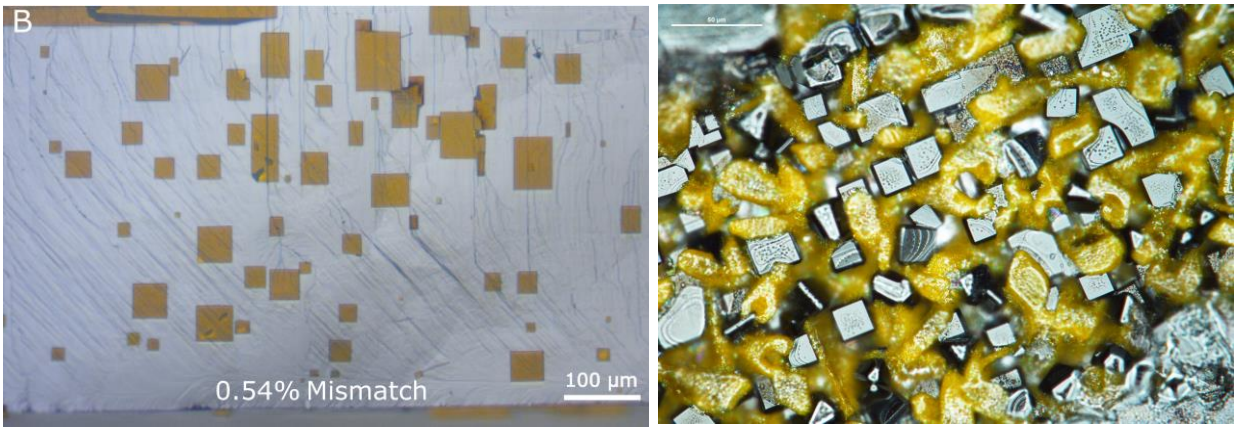

Left: Orange $CH_3NH_3PbBr_3$ crystals grown on top of PbS, showing clear alignment of crystal edges. *Right:* $CH_3NH_3PbI_3$ grown on top of PbSe, showing some alignment of crystal edges. The yellow material is excess PbI_2 that has crashed out of solution but not crystallized into perovskite.

1.2. Colloidal Solutions of $PbS_n([PbBr_3][CH_3NH_3])_m$

1.2.1. Synthesis of PbS QDs

PbS Quantum dots were synthesized using thiourea precursors as previously reported.[10] Briefly, solution of $Pb(O_2CR)_2$ was dissolved in octadecene and heated to 90-120°C under nitrogen. 10-50mM solution of thiourea (with appropriate rate of conversion for the desired size) was injected and allowed to react until completion. The reaction mixture was then combined with hexanes upon cooling to room temperature. Methyl acetate was added to crash out the QDs and remove polar organic impurities. The solution was centrifuged a 2000 rpm, and this anti-solvent precipitation was repeated 3-5 times.

1.2.2. Ligand Exchange

Native $Pb(O_2CR)_2$ ligands were than replaced with lead halide salts using a phase transfer exchange from pentane or hexanes to N-methylformamide based on a procedure developed by Dirin *et al*[22] but modified to maximize electrostatic stability while maintaining excess perovskite precursor in solution to form the conductive matrix on crystallization. The exchange occurs rapidly, depending on the concentration of the PbS QDs and the concentration of perovskite precursor (more QDs take more time to transfer, more ions enable more rapid phase transfer). Often there is an emulsion at the interface, likely some lead halide/oleate adduct.

The resulting PbS solution in polar solution was found to contain residual oleate species by ^1H NMR. $PbS_n([PbBr_3][NH_3CH_3])_m$ QDs were precipitated using methyl acetate anti-solvent and centrifugation before being redispersed in N-methylformamide. After the cleaning procedure was repeated three times the NMR spectrum was clear of alkene proton signals, suggesting complete removal of oleate species from the sample. The cleaning procedure also removed excess lead halide and ammonium halide salts from solution, leading to precipitates that were no longer soluble in highly polar organic solvents. The color of the precipitate varied from bright orange – resembling the $CH_3NH_3PbBr_3$ perovskite solid – to dark brown – resembling PbS QDs – depending on the concentration of halide salts.

1.2.3. *Stability of colloids*

Reintroduction of halide salts produced clear, dark solutions, indicating that the ionic strength of the solution plays an important role in the stability of the electrostatically stabilized QDs. Even the brightly orange colored precipitates formed clear, dark solutions, suggesting the full dissolution of perovskite precursor salts. According to the DLVO theory of colloidal stability, increased ionic strength should decrease the solubility of electrostatically

stabilized colloids by shielding the electric field created by surface charges, thereby decreasing the repulsive electronic double layer interactions.[23] If the surface ions (e.g. $PbBr_3^-$) are highly labile, however, the increased shielding may be compensated for by an increase in surface charge due to a higher concentration of anions binding to the NC surface. Assuming an equilibrium between anions bound to nanocrystal surface sites and free anions in solutions, surface charge can be increased by pushing equilibrium towards surface bound anions. In a similar manner, Dirin *et al*. suggest using solvents that are poor at solvating anions, such as propylene carbonate, to increase the surface charge by reducing the lability of surface anions.[22] This method is useful for increasing colloid stability, but makes introduction of additional halide salts, which will become the conductive matrix in the solid state, difficult. Since halide salts in solution were removed, additional CH_3NH_3Br and $PbBr_2$ were added to the solution after ligand exchange. The second addition of halide salts allowed for precise control over perovskite precursor concentration and the relative loading of QD emitters in the cocrystal.

Table 1 - Solvent Properties

	Dielectric constant	E_TN	DN	AN
N-methyl formamide	182	0.72	27	32.1
N,N-dimethyl formamide	29	0.4	26.6	16
Propylene Carbonate	64	0.47	15.1	18.3
Dimethyl sulfoxide	46.7	0.44	29.8	19.3
Acetonitrile	37.5	0.46	18.9	14.1
Water	80.1	1	54.8	18

The ideal solvent for electrostatically stable colloids will have sufficient dielectric constant to allow the separation of ions so that electric double layers can form on the surface of the particles.[23] This allows the particles to electrostatically oppose each other and yields colloidal

solubility. Table 1 lists several experimental parameters of solvents used in this study. Dimroth's number (E_TN) is a measure of the polarity or ionizing power of a solvent, defined by the wavelength of maximum absorbance of a solvochromatic dye (usually pyridiniophenolate) normalized to water and trimethyl silane as 1 and 0, respectively.[24,25] Donor (DN) and Acceptor (AN) Numbers were developed by Gutmann[26] to help describe the Lewis basicity and acidity of solvents. DN is measured as the negative enthalpy (-ΔH) of formation of an adduct of the solvent molecule in question with $SbCl_5$ in dichloroethane. AN is measured using ^{31}P NMR shifts of triethylenephosphine oxide adducts with Lewis acidic solvent molecules.[27] Solvents with low AN are helpful to prevent anion dissociation. A high Donor Number is preferred to enable cation dissociation. At first glance it appears that Propylene Carbonate (PC) is the ideal choice (as used by Dirin *et al*.[22]) however, perovskite precursors are not soluble in this solvent. DMF is also a good choice, and was often used as an exchange medium (due to the availability of dry DMF), however it has a relatively low dielectric constant, which made the exchange less facile (though possible) and the colloidal stability was reduced. A cosolvent system of propylene carbonate and DMF produced stable colloids but lackluster photoluminescence properties, perhaps due to separation of perovskite domains (soluble in DMF) and QD domains (soluble in PC). N-methyl formamide (NMF) was found to be the best option with additional perovskite precursor salts added to compensate for its high AN passivation of anions, as discussed above. Table 1 lists the relevant information about solvent choice, with some comparisons to other common polar organic solvents.

1.2.4. Air-free ligand exchange

Another important factor affecting the ligand exchange and colloidal stability of the PbS particles with perovskite precursor ligands is exposure to air. PbS samples capped with

Pb(oleate) that had been in left in ambient environment often showed poor exchange, and especially, poor solubility in polar solution - even with excess dissolved ions as discussed previously. It is likely that these samples had experienced some oxidation on the surface, thus preventing binding of $[PbBr_3]^-$ anions to the surface of the particle. Not only did this obviously impact the colloidal stability, but it would likely have been detrimental to the optical performance of the resultant cocrystal.

Samples of PbS that were either fresh or stored in the glovebox showed much greater stability. Unfortunately, the ligand exchange and sample preparation could not be performed in a nitrogen glovebox, because of fears that the methylammonium salts could degrade into acidic products that would be detrimental to the glovebox catalyst. To achieve air-free exchanges samples were generally prepared on a Schlenk line under positive argon pressure with a septum on top of a glass vial. An equal volume of perovskite precursor solution in dry DMF from the Nuckolls lab solvent system, or gas sparged NMF would be added via syringe, and the phase exchange transfer agitation would take place in this vial. Cleaning to remove excess oleate species was done by centrifuging the glass vial, with some padding to prevent glass breakage.

1.3. Crystallization from $PbS_n([PbBr_3][NH_3CH_3])_m$ solution

Due to the high boiling point of N-methylformamide, additional steps were required to ensure the crystallization of the perovskite matrix without impacting the interface with the PbS. For samples made using spin coating, toluene was added a few seconds after the solution was deposited to the spinning substrate to reduce the polarity of the solution and induce crystallization. Samples were then gently annealed (T<50°C) to help dry the substrate. For samples analyzed on TEM grids, even if they were spun coat, samples were loaded into a

vacuum oven and left under vacuum at room temperature overnight or longer. Higher temperature annealing was found to be detrimental to the optical properties of the cocrystals, as discussed later.

1.3.1. Morphology of cocrystals on substrate

This solution of $PbS_n([PbBr_3][NH_3CH_3])_m$ was then spun coat onto glass or sapphire substrates that had been cleaned and treated with oxygen plasma to increased hydrophilicity. This simple one-step spin coating of a single solution containing both the QD emitters and the conductive passivating matrix is advantageous for low-cost processing. The samples appeared orange in color, due to the relatively low loading of PbS NCs and the strong absorbance of $CH_3NH_3PbBr_3$, and showed large perovskite domains.

Figure 3

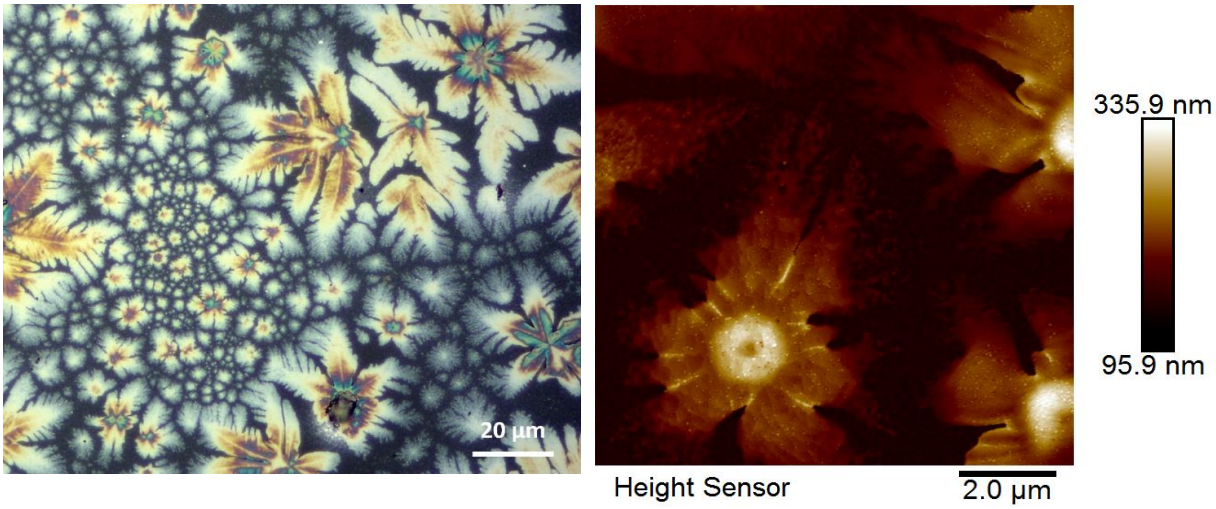

Left: Optical microscope image of cocrystal domains on ITO. *Right:* AFM micrograph of cocrystal domains on ITO. Height bar included indicated domain heights of approximately 240 nm

1.3.2. TEM Micrographs of cocrystals

Transmission electron micrographs taken on the cocrystals revealed monodisperse, spherical NCs forming square assemblies ranging from 4 – 20 NCs, as shown in Figures 4 and 5 . The NCs appear to be mostly separated (i.e. no crystal necking) and have aligned crystal lattices, as detailed in Figure 4, suggesting the presence of an epitaxial matrix surrounding them. The space between the NCs may be amorphous or beam-damaged perovskite. It is worth noting that neither Dirin *et al*[22], or Ning *et al*.[15] did not observe square assemblies in TEM micrographs of their similar samples.

Figure 4

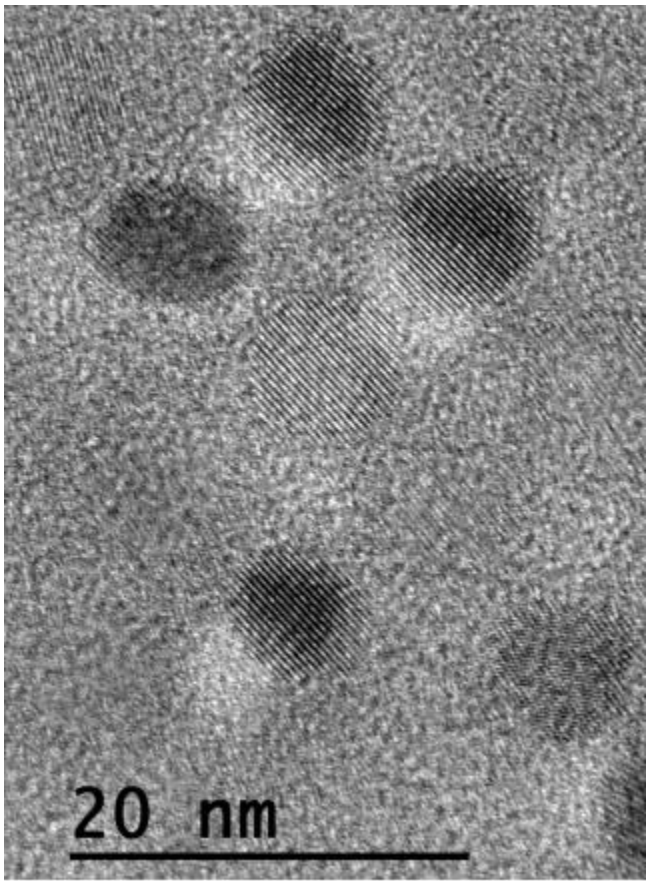

TEM micrograph of PbS NCs in $CH_3NH_3PbBr_3$ crystal matrix. The lattice planes of the NCs are clearly aligned while the spherical particles are separated by the perovskite matrix.

The perovskite matrix is highly unstable under high electron flux, however, forming crystalline, high-contrast degradation products, which can easily be misidentified as embedded NCs. This makes direct imaging of the NC-perovskite interface virtually impossible on a microscope operating at normal electron flux. All inorganic $CsPbBr_3$, used in place of the hybrid organic/inorganic perovskite with the hope of increasing stability for electron microscopy studies, proved equally unstable under normal operating conditions.

Figure 5

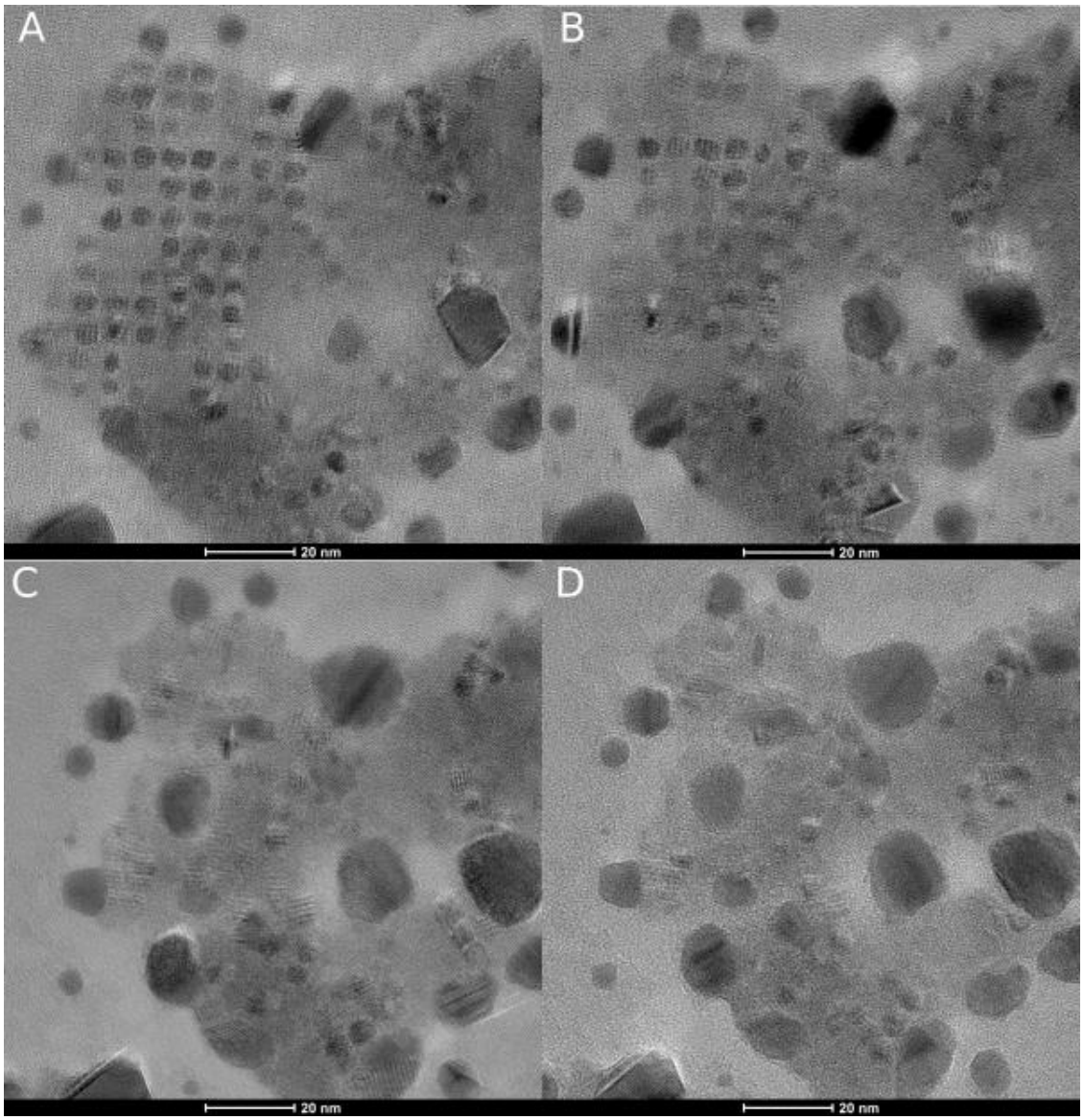

TEM micrographs of $PbS/CH_3NH_3PbBr_3$ co crystal. Taken in succession from A-D

Crystalline degradation products showed a drastic loss in bromine by EDS analysis (Figure 6), suggesting that the instability is due, in part, to loss of halide from the sample. It is not difficult to imagine a residual sample of Pb metal or a Cs/Pb alloy creating a crystalline, strongly diffracting area on the TEM grid. Using a direct electron detector to monitor crystalline structure of the perovskite at low electron flux, we have estimated the threshold to beam damage to be on the order of 1000 $e^-/(Å^2\ sec)$ in $CsPbBr_3$.

In Figure 5 a large square array of PbS nanocrystals is visible on the left side of a larger, diffraction domain, note the larger crystalline objects on the right and bottom of the micrograph. As this area is continually exposed to the electron beam from 5A-D one can see the square array of nanocrystals is obscured, presumably by some degradation product of the perovskite matrix that is surrounding the nanocrystals. The larger crystalline degradation products surrounding the array grow in size, and new degradation crystalline domains grow where there once was clear nanocrystals underneath. These results suggest that the nanocrystals are fully surrounded by electron beam sensitive perovskite material.

Figure 6

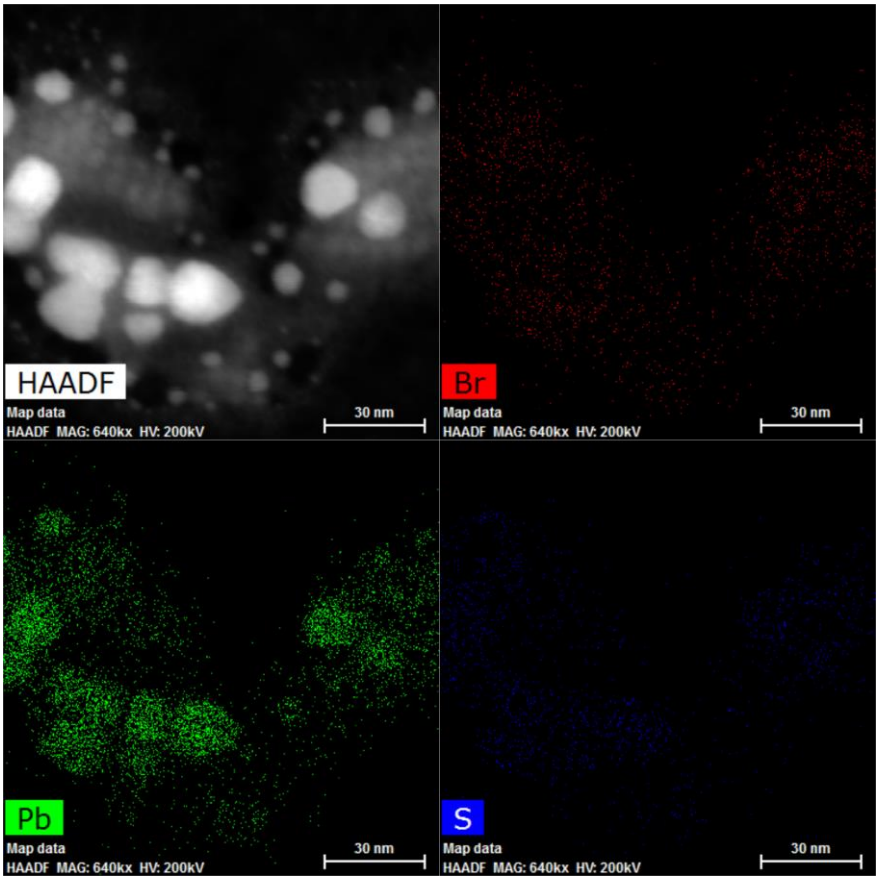

HAADF STEM elemental mapping of PbS/perovskite cocrystal. The degradation products (brightly diffracting in the top left) appear to be mostly Pb metal and diffract electrons efficiently

1.4. Optical Properties

Surface passivation of the PbS quantum dots is achieved by the nearly perfect epitaxial alignment of the lead halide perovskite. The matrix can be thought of as an extended shell, passivating surface traps and isolating cores from their surrounding chemical environment. Given the good carrier mobilities of lead halide perovskites[28], attributed to the unique structural properties of the crystal structure,[29,30] this system should exhibit both effective surface passivation and increased charge transport from a single electrostatically stabilized colloidal dispersion.

1.5. Band structure

Figure 7 shows a proposed band structure for the PbS/$CH_3NH_3PbBr_3$ cocrystals, based on the size dependent band edges of PbS QDs as reported by Jaseniak *et al.*[31] and literature values for $CH_3NH_3PbBr_3$.[32]

Figure 7

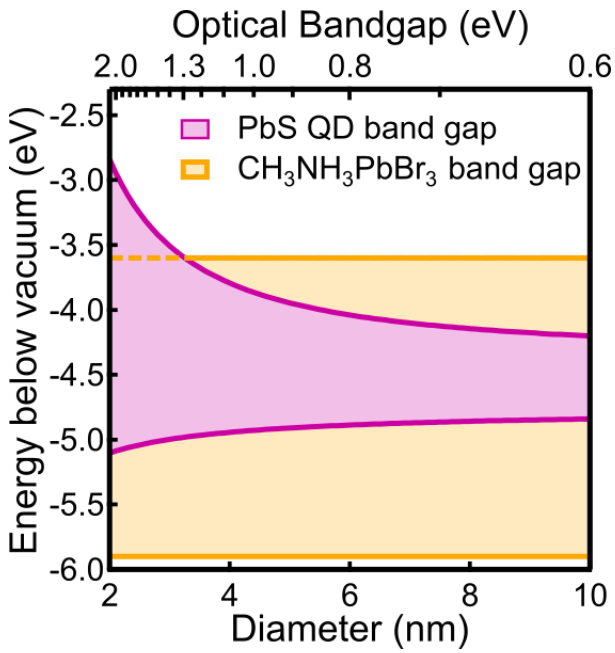

HOMO and LUMO of PbS QDs[31] (purple) as a function of size plotted against valence and conduction bands of $CH_3NH_3PbBr_3$ (orange). The size dependence of the PbS QD HOMO and LUMO allows for the preparation of both type I and type II aligned heterostructures.

Since the electronic structure of QDs depends strongly on the nature of the QD surface chemistry[5,33], it is likely that the absolute position of these bands may change. The local electronic structure of the PbS/Perovskite interface is likewise difficult to predict, given electronic interactions between the two. This proposed band structure, however, is a useful tool for both planning cocrystal structure (e.g. NC size) and for understanding the results of our experiments. As seen in Figure 7, Type-I semiconductor systems, ideal for light emitting

applications, are easy to access across a wide range of nanocrystal emission energies in the infrared in these cocrystals.

Figure 8

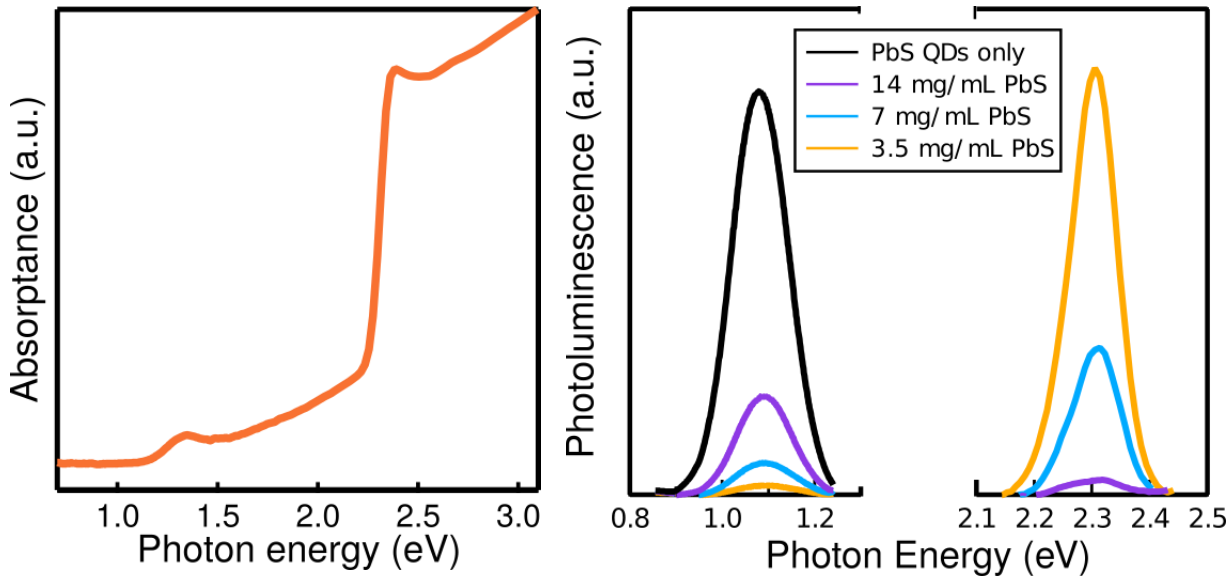

Left: Solid state absorptance spectrum of PbS/perovskite cocrystal with clear features indicating PbS NC (1.3eV) and CH3NH3PbBr3 (2.4eV) light absorption *Right:* Photoluminescence spectra of PbS NCs and perovskite emission from cocrystal as a function of PbS loading.

1.5.1. Absorbance and Photoluminescence

The absorptance spectra of PbS/$CH_3NH_3PbBr_3$ co crystal on glass substrate shown in Figure 8 contain characteristic transition features of both PbS NCs (1.4 eV) and the $CH_3NH_3PbBr_3$ matrix (2.3 eV). Photoluminescence spectra on the same substrates at different QD loadings are also shown in Figure 8, where we observe both QD (~1.1 eV) and perovskite (~2.3 eV) emission. The photoluminescence (PL) signal of the PbS (~1.1 eV) increases as expected due to an increased number of emitters. The $CH_3NH_3PbBr_3$ perovskite emission spectra are more interesting, as an increase in QD loading leads to a *decrease* in perovskite emission. Because the photoluminescence quench is so pronounced, and the same concentration of perovskite precursor solution was used in all samples, the quench in PL intensity suggests that

electron hole-pairs generated in the perovskite are transferred to the NCs instead of recombining. PL excitation spectroscopy confirmed the quench in PL corresponded to energy transfer into PbS NCs. While monitoring the emission of NCs the energy of the excitation beam was tuned between 1.6 eV and 2.8 eV.

Figure 9

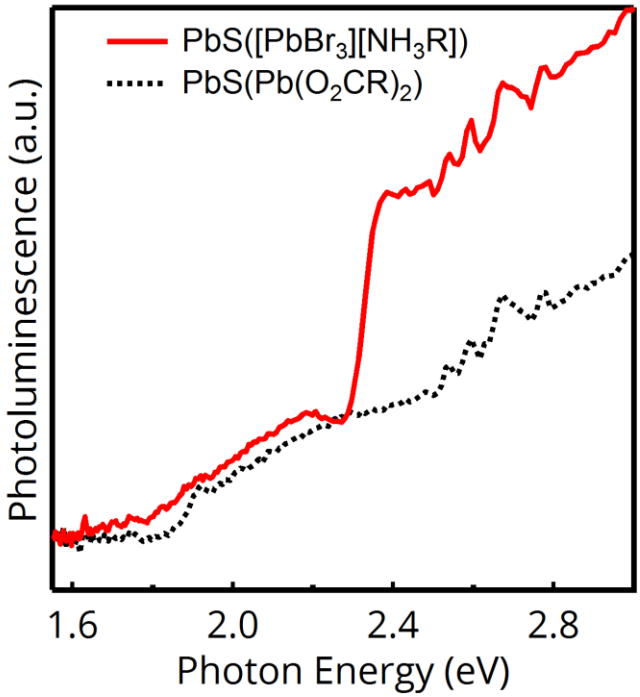

PL excitation spectra monitoring NC emission of PbS with native ligands(black, dashed) and in perovskite matrix (red, solid). Increased intensity at ~2.3 eV corresponds to perovskite band edge.

The spectra of NCs in perovskite and NCs as synthesized (with native lead oleate ligands) in Figure 9 show a distinct rise in PL intensity when the cocrystal is pumped at energies greater than 2.3 eV, corresponding to absorption of perovskite. This indicates carrier transfer from the perovskite to the PbS. The PbS with native lead oleate ligands show no drastic increase at 2.3eV.

1.5.2. Transient Absorption

To probe the dynamics of energy transfer, samples of the cocrystal were spun on sapphire substrates and given to M. Tuan Trinh, a collaborator in Prof. Xiaoyang Zhu's group, to measure using ultrafast transient absorption. Figure 10 shows a heat map of the difference spectra taken below the perovskite band edge.

Figure 10

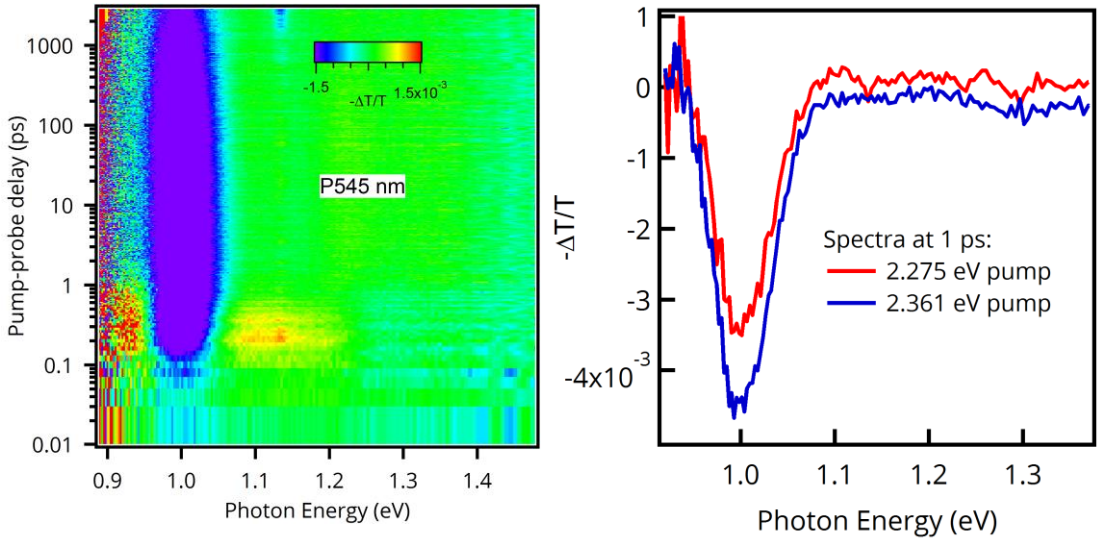

Left: Transient absorption difference spectra heat map taken of cocrystal below perovskite band edge. *Right:* difference spectra taken at 1 ps delay time when pumped above (blue) and below (red) perovskite band edge.

A clear bleach in absorbance is seen in at the quantum dot $1S_e$-$1S_h$ transition (1 eV). Samples were also pumped above the onset of $CH_3NH_3PbBr_3$ absorbance. Increased bleaching of the quantum dot $1S_e$-$1S_h$ transition is seen when pump energies above the perovskite bandgap are used, confirming charge-carrier transfer from matrix to NC.

When this transition is integrated over early time scales (up to 5 ps) normalized traces measured with pump energies above the matrix bandgap are indistinguishable from those with below gap energies (Figure 11). In other words, bleaching due to electron-hole pairs generated in the NCs has the same rise-time as bleaching from perovskite excitation. This suggests that

charge-carrier transfer occurs at time scales faster than instrument response, on the order of 100 fs. If transfer was slower (e.g. ps-ns scale) one would expect to see an increase in the bleaching signal over these time scales as carriers continue to fill electronic states. The rapid rate of carrier transfer into the NCs suggests that defects at the interface of NC and perovskite do not create charge carrier trap states, and that the NCs that receive energy transfer from the matrix are within some distance of an excitation that allows for the charges to diffuse to them in under ~500 fs.

Figure 11

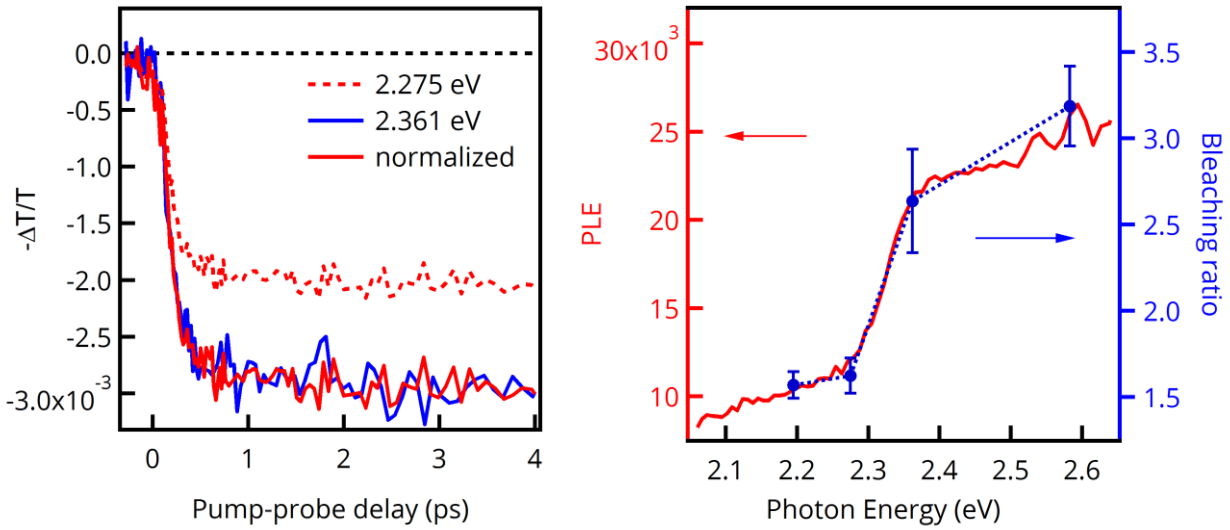

Left: Time trace integrated area of the PbS bleach (0.9-1.1eV) pumped below (red, dashed) and above (blue, solid) perovskite band edge. Normalized (red, solid) trace indicates rapid carrier transfer. *Right:* Plot of PLE superimposed on bleaching ratio, showing increase in PbS bleaching when perovskite begins absorbing.

The increased bleaching above matrix bandgap is confirmed by the bleaching ratio, Figure 11, which is the bleaching signal of the cocrystals divided by the bleaching of a sample of native $Pb(O_2CR)_2$ capped PbS QDs. To normalize for increased absorption of QDs at higher photon energies and fluctuations in laser pump intensity, the bleaching signal of the $PbS/CH_3NH_3PbBr_3$ was divided by the bleaching of a $PbS(Pb(O_2CR)_2)$ solid sample.

The increase of this bleaching ratio corresponds well with the band edge absorption of the perovskite and the PLE data discussed previously. Note that this bleaching ratio is ~1.5 below

the band gap, instead of normalized to 1, indicating excess PbS absorption in the $PbS/CH_3NH_3PbBr_3$ sample due to a higher concentration of dots in the sample. The rapid rate of carrier transfer into the QDs suggests that defects at the interface of NC and perovskite do not create charge carrier trap states.

Figure 12

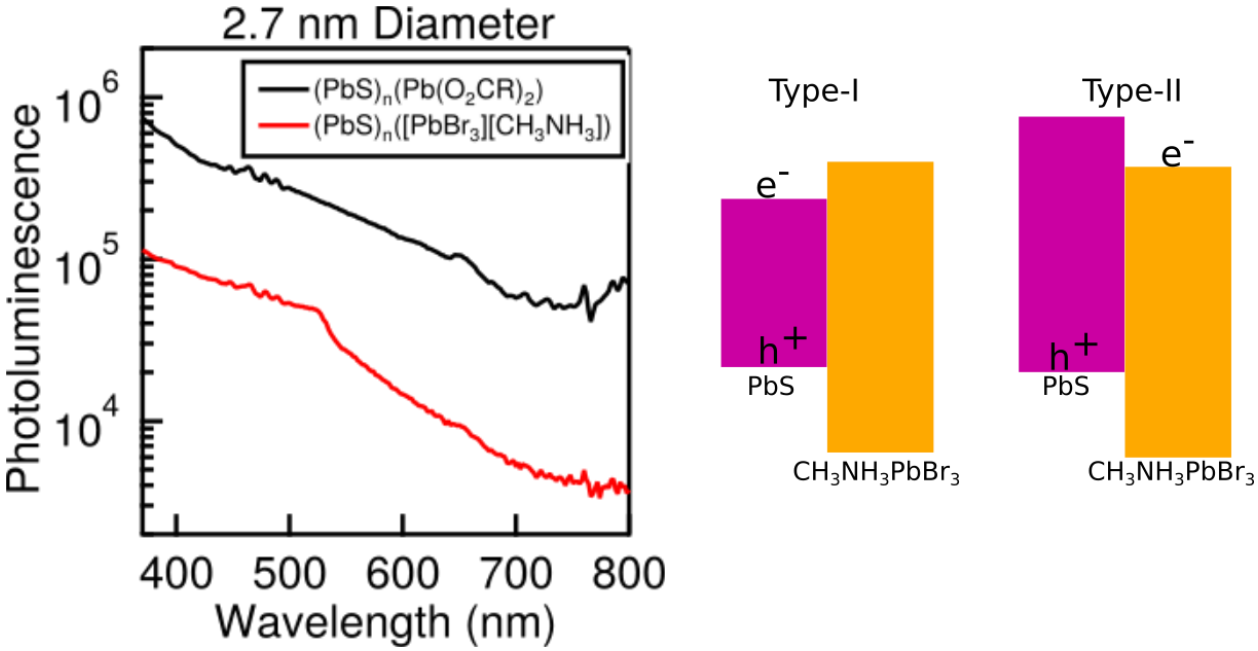

Left: PLE spectra of small, 1.5 eV absorbing PbS, with native oleate ligands and perovskite matrix. PL intensity is quenched across all excitation wavelengths. *Right:* Schematics of Type-I and Type-II energy level diagrams showing localization of charges (Type-I) and separation of charges (Type-II).

When smaller sized QDs are used (diameter = 2.7 nm) PLE studies show an overall quench of the QD luminescence relative to QD only samples, although there is still energy transfer occurring (Figure 12). Type-II arrangement may be accessible in this size regime, according to Figure 7, and the quench is likely from charge separation between the perovskite and the QDs (Figure 12). Photoluminescence lifetimes were also used to study the emissive properties of the cocrystal samples. Small bandgap, Type-I structures preserved the PL lifetime relative to $Pb(O_2CR)_2$ capped QD solids, while large bandgap, Type-II structures saw reduced

relative PL lifetimes (Figure 13). If electron-hole pairs are able to separate in Type-II structures a reduced lifetime is expected. The PL lifetime of the large bandgap QDs was longer than that of small bandgap QDs, which is why we compare to the native ligand system as a control.

Figure 13

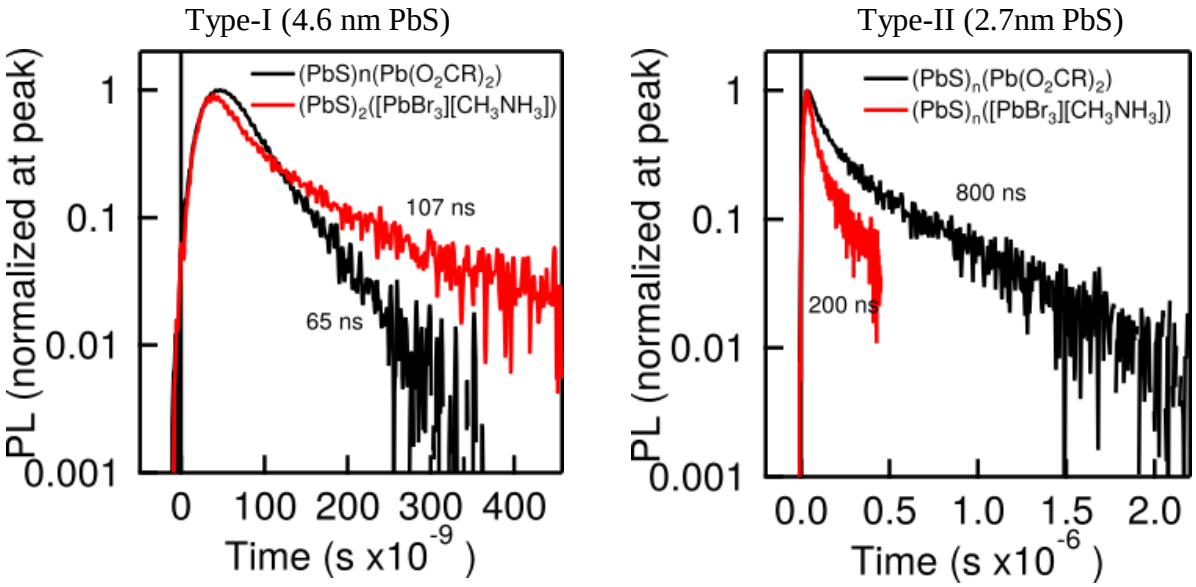

IR PL lifetime decay trace of $PbS([PbBr_3][CH_3NH_3])$ and $(PbS)_n(Pb(O_2CR)_2$ native oleate ligands *Left:* Type-I alignment between PbS and perovskite *Right:* Type-II alignment (higher bandgap PbS)

1.6. Conclusions and Outlook for PbS/perovskite cocrystals

Efficient charge carrier transfer from $CH_3NH_3PbBr_3$ into PbS was demonstrated via photoluminescence excitation spectroscopy and ultrafast transient absorption. This charge injection is made possible by the passivation of PbS QD surfaces by the epitaxially matched $CH_3NH_3PbBr_3$ matrix. With careful choice of solvent and ionic strength, stable colloidal solutions of $PbS_n([PbBr_3][NH_3CH_3])_m$ can be produced, enabling simple spin-coating fabrication of cocrystals. This represents an exciting opportunity to continue development of efficient QD devices and to study the fundamental carrier transfer dynamics between the two materials. NIR

PLQY measurements were attempted with collaborators, however, the samples provided required more optimization for the measurement to yield reliable results. Higher PLQY when pumped above the perovskite band-edge would further confirm the potential for use in IR emissive applications.

Future work should include transient absorption measurements of small PbS QDs to confirm Type-II alignment, measurements of band energies of both perovskite and QDs in the cocrystals, and clear evidence of epitaxial alignment at the nanoscale using TEM.

1.7. Growing Single crystals of lead halide perovskites

In order to better grow large, high quality single crystals of lead halide perovskite containing methylammonium ($CH_3NH_3^+$), Cesium (Cs^+), mixed with lead bromide (Br^-), Chloride (Cl^-), and Iodide (I^-) systematic experiments were required. In general, a solution of the lead halide precursor mixed with the cation were dissolved in a polar organic solvent. This solution was exposed to a volatile, non-polar solvent in a closed chamber. The nature of the solvent and anti-solvent has strong impact on the resulting crystals. Table 2 below illustrates images of some of the results. In general, results either formed large orange crystals, small orange crystals, white needle crystals, yellow fluorescent crystals, or some combination of these. The use of dimethyl formamide as solvent generally lead to high quality orange crystals, with some white needles. The use of formamide as solvent generally lead to yellow fluorescent crystals, with some white needles and some orange crystals. The choice of anti-solvent also played a large role. Acetone failed to produce any perovskite crystals; IPA was a good choice for forming large, high quality perovskite crystals. N-propyl formamide worked similarly to IPA, but worked more slowly, yielding larger crystals.

Table 2

	Dimethyl formamide	N-methyl Formamide	Formamide	Dimethyl Sulfoxide
Acetone	White Needles	White Needles, Dark color	White Needles, Yellow Crystals	Dark Color, White Needles
Isopropyl Alcohol	Orange crystals (0.5M,1M, 1.6M)	Orange crystals, White precipitate	Orange Crystals, Yellow Crystals	White Needles
Dichloromethane	Orange Crystals	Orange crystals, White precipitate	Orange Crystals, Yellow Crystals	Orange Crystals, Yellow Crystals
Nitromethane	Orange Crystals	Orange crystals, White precipitate	Orange Crystals, Yellow Crystals	White precipitate

Crystals of $CsPbBr_3$ were made using the same method, generally using isopropyl or n-propyl alcohol as antisolvent and dimethyl formamide as solvent. $CH_3NH_3PbCl_3$ single crystals could only be grown from diffusion of n-propyl alcohol vapor into a 0.15 M solution of 1:1 lead chloride (98%, Sigma-Aldrich) and methylamine hydrochloride (Sigma-Aldrich) in concentrated hydrochloric acid (37%, Sigma-Aldrich). Single crystals were provided to collaborators who performed IR[34], Raman[35], and transport measurements[28] to better understand their intrinsic materials properties.

1.7.1. Formamide lead bromide crystals

Interestingly, the yellow crystals - which formed when Formamide ($HCONH_2$) was used as antisolvent, and a small amount with DMSO/DCM - formed bright yellow, fluorescent crystals. Single Crystal XRD revealed a layered $(HCONH_2)PbBr_2$ crystal with formamide molecules in a hydrogen bonding network between the $PbBr_2$ layers. (Figure 15).

Figure 14

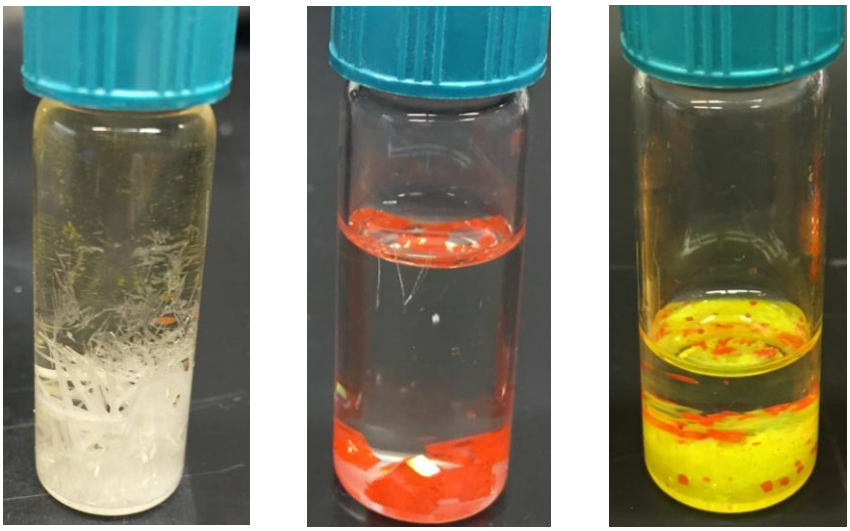

Representative pictures of single crystals grown from solution. *Left:* White needles grown from dimethyl formamide solution with acetone antisolvent. *Middle*: Orange $CH_3NH_3PbBr_3$ perovskite crystals grown from dimethyl formamide solution with nitromethane antisolvent. *Right:* Yellow $(HCONH_2)PbBr_2$ crystals (with some perovskite crystals as well) grown from Formamide solution with dichloromethane antisolvent.

Figure 15

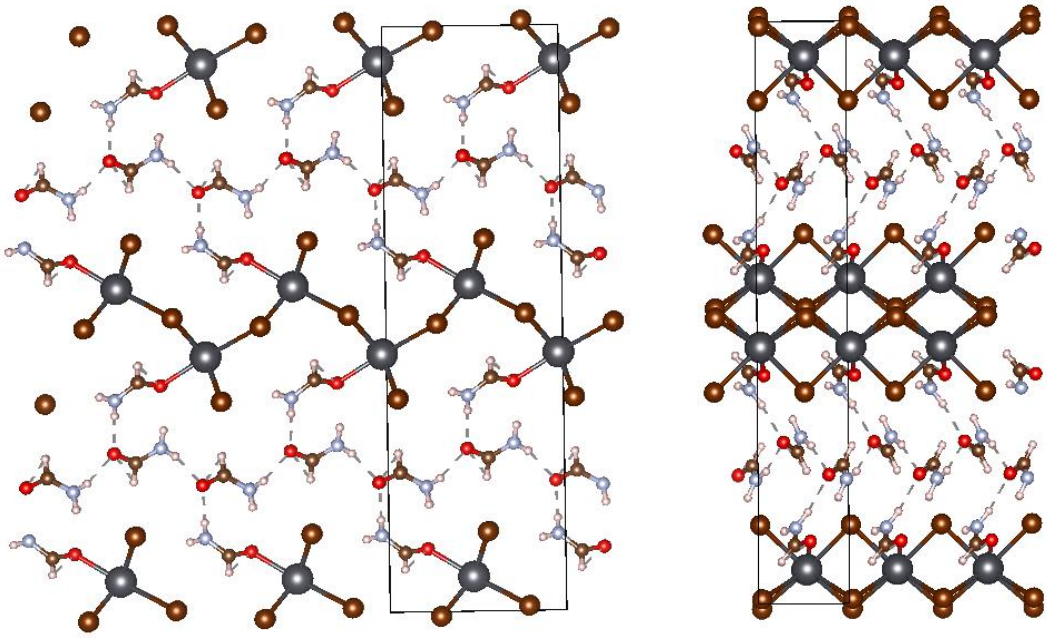

Crystal structure of formamide$_2$PbBr$_2$ along the c and a axis, respectively. Lead (gray) atoms are bound to Bromide atoms (brown) in layers with solvent (formamide) hydrogen bonding interstitial.

1.8. Additional Figures

Figure 16

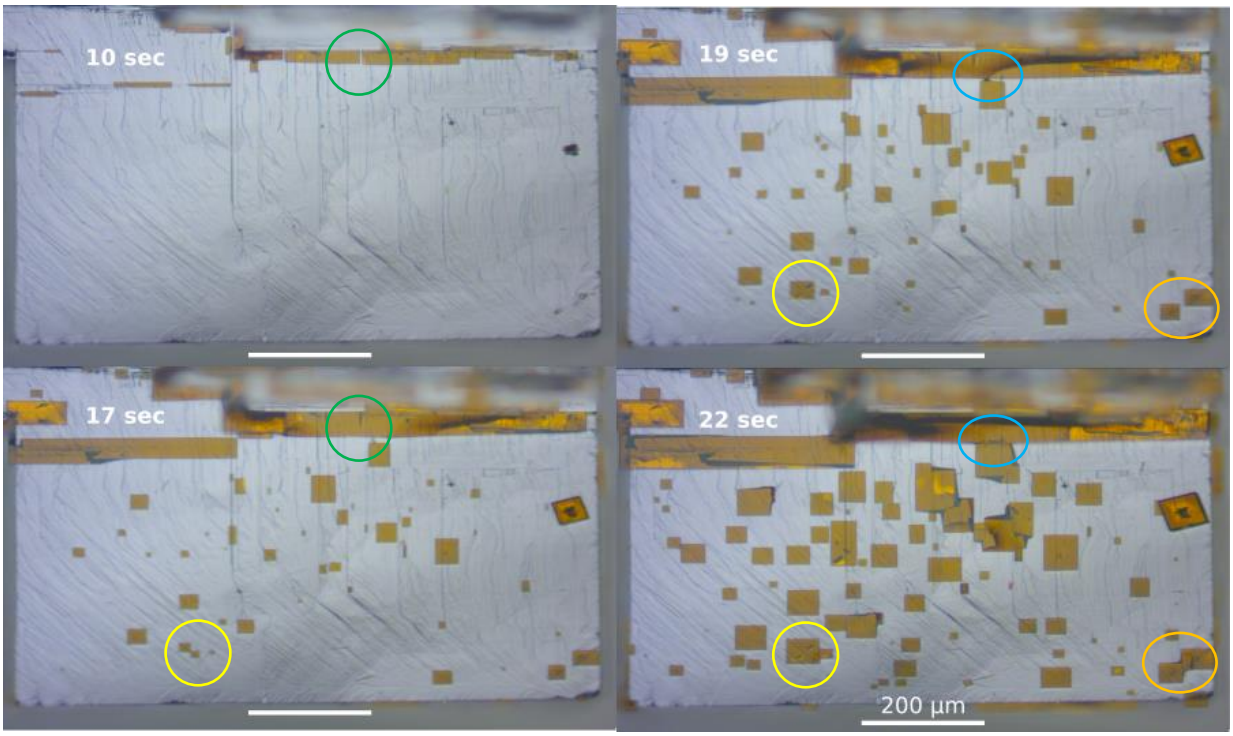

Optical images of single crystal growth of $CH_3NH_3PbBr_3$ (orange). colored circles highlight single crystals growing together

1.9. Experimental

1.9.1. Materials and Methods

Methylamine solution (40% in H_2O), 48% Hydrobromic acid, lead bromide, lead chloride, methylamine hydrochloride, and lead iodide were purchased from Sigma and used without further purification.

PbS synthesis

1.3 eV PbS NCs (PLE) 0.6 g lead oleate and 6.8 g of 1-octene were combined in a 3 neck round bottom flask in an inert glovebox. The solution was heated to 90°C on a Schlenk line under Ar. A solution of 50 mM 2,6-trifluoromethylphenyl, phenyl thiourea in 0.6 g diphenyl

ether was injected. Reaction mixture was cleaned by precipitation using methyl acetate, centrifugation, and redispersion in hexanes.

1.0 eV PbS NCs (Transient Absorption) 2.8 g lead oleate and 33.4 g of 1-octene were combined in a 3 neck round bottom flask in an inert glovebox. The solution was heated to 110°C on a Schlenk line under Ar. A solution of 40 mM 4-fluoromethylphenyl, dodecyl thiourea in 2.5 mL dibutyl ether was injected, the reaction took about 28 minutes to finish. Reaction mixture was cleaned by precipitation using methyl acetate, centrifugation, and redispersion in hexanes.

CH_3NH_3Br synthesis

150 mL methylamine (1.3 eq) in H_2O solution was stirred in a 1 L round bottom flask at 0°C. 150 mL of HBr solution was added dropwise while stirring. After complete addition the solution was stirred for 30 minutes. Salt was recovered from solution with the rotary evaporator and dissolved in ethanol. Solution was heated to 75°C and stirred until dissolved. About 50 mL diethyl ether was added and the sample was placed in the fridge to recrystallize. Recrystallization was repeated until colorless, white crystals were recovered.

Perovskite precursor ligand exchange

PbS nanocrystal solution in hexanes (10-60mM PbS) were added to a vial with 50 mM CH_3NH_3Br and $PbBr_2$ dissolved in N-methylformamide (NMF) or Dimethyl formamide (DMF). Sample was shaken or otherwise agitated until all the dark solution had moved into the bottom, polar NMF phase. The top hexanes layer was carefully decanted off, and the solution was added to a centrifuge tube where 10-50 mL of methyl acetate was added to precipitate the QDs and orange perovskite. The solid was redispersed in NMF and this process was repeated 2x more.

After 3 washes the solid was redispersed in NMF and additional CH_3NH_3Br and $PbBr_2$ was added to improve solubility and create the perovskite crystal.

Transmission Electron Microscopy

Micrographs of $(PbS)_n([PbBr_3][CH_3NH_3])$ co crystals were recorded on FEI TALOS F200X Transmission/ Scanning Electron Microscope operating at 200 kV. Samples were deposited on O_2 plasma treated SiN TEM grids.

Photoluminescence

Visible photoluminescence was obtained on a Horiba Fluoromax-4. Infrared photoluminescence spectra and lifetime on a Horiba Fluorolog-3, courtesy of Dr. Steffen Jockusch.

Absorptance

Absorptance measurements were calculated from transmittance and reflectance measurements made using an integrating sphere on a lambda 950 UV/Vis spectrometer. The absorptance was plotted as $-log\left(\frac{t}{t_g}+\frac{r}{r_o}\right)$ where t and r are the transmittance and reflectance of the sample, respectively, t_g is the transmittance of a blank glass substrate, and r_o is the baseline reflectance of the integrating sphere.

Transient absorption spectroscopy

Transient absorption spectra were taken at Brookhaven National Lab on a home built set up in the lab of Dr. Matt Sfeir. Dr. M. Tuan Trinh made the measurements and analysis.

Single crystal XRD

Yellow, green-fluorescent crystals of $PbBr_2(C_2H_6N_2O)_2$ were grown from a diffusion of dichloromethane into formamide at room temperature. A large block that slowly decomposes under the microscope (.27 x .15 x .10 mm) was mounted with the aid of STP oil treatment and cooled to 100 K on the diffractometer. Complete data (99.6%) were collected to 0.833 Å. 14,510 reflections (# unique 2,127, # observed 2,089 >4σ(F_o) were collected with R_{int} of 0.0762 and R(sigma) of 0.0511 after absorption correction (T_{max} = 0.142; T_{min} = 0.025). The space-group was determined as Cc based upon systematic absences, and the structure was solved using SHELXS by the Patterson method. A higher symmetry solution in C2/c fails. All non-H atoms were located routinely, and the hydrogen atoms were placed in calculated positions and refined with riding coordinates and ADPs. The final refinement (2127 data, 82 parameters, 2 restraints) converged with R_1 ($F_o > 4\sigma(F_o)$) = 3.05%, wR_2 = 6.44%, and S = 1.029. Full = 0.833 Å, Max = 0.720 Å, Highest peak = 1.70, Deepest hole = -2.21

1.10. References

(1) Caruge, J. M.; Halpert, J. E.; Wood, V.; Bulović, V.; Bawendi, M. G. Colloidal Quantum-Dot Light-Emitting Diodes with Metal-Oxide Charge Transport Layers. *Nat. Photonics* **2008**, *2* (4), 247–250. https://doi.org/10.1038/nphoton.2008.34.

(2) Anikeeva, P. O.; Halpert, J. E.; Bawendi, M. G.; Bulović, V. Quantum Dot Light-Emitting Devices with Electroluminescence Tunable over the Entire Visible Spectrum. *Nano Lett.* **2009**, *9* (7), 2532–2536. https://doi.org/10.1021/nl9002969.

(3) Zhang, Z.; Ye, Y.; Pu, C.; Deng, Y.; Dai, X.; Chen, X.; Chen, D.; Zheng, X.; Gao, Y.; Fang, W.; et al. High-Performance, Solution-Processed, and Insulating-Layer-Free Light-Emitting Diodes Based on Colloidal Quantum Dots. *Adv. Mater.* **2018**, *30* (28), 1801387. https://doi.org/10.1002/adma.201801387.

(4) Anderson, N. C.; Hendricks, M. P.; Choi, J. J.; Owen, J. S. Ligand Exchange and the Stoichiometry of Metal Chalcogenide Nanocrystals: Spectroscopic Observation of Facile Metal-Carboxylate Displacement and Binding. *J. Am. Chem. Soc.* **2013**, *135* (49), 18536–18548. https://doi.org/10.1021/ja4086758.

(5) Busby, E.; Anderson, N. C.; Owen, J. S.; Sfeir, M. Y. Effect of Surface Stoichiometry on Blinking and Hole Trapping Dynamics in CdSe Nanocrystals. *J. Phys. Chem. C* **2015**, *119* (49), 27797–27803. https://doi.org/10.1021/acs.jpcc.5b08243.

(6) Mashford, B. S.; Stevenson, M.; Popovic, Z.; Hamilton, C.; Zhou, Z.; Breen, C.; Steckel, J.; Bulovic, V.; Bawendi, M.; Coe-Sullivan, S.; et al. High-Efficiency Quantum-Dot Light-Emitting Devices with Enhanced Charge Injection. *Nat. Photonics* **2013**, *7* (5), 407–412. https://doi.org/10.1038/nphoton.2013.70.

(7) Nag, A.; Kovalenko, M. V.; Lee, J.-S.; Liu, W.; Spokoyny, B.; Talapin, D. V. Metal-Free Inorganic Ligands for Colloidal Nanocrystals: S2–, HS–, Se2–, HSe–, Te2–, HTe–, TeS32–, OH–, and NH2– as Surface Ligands. *J. Am. Chem. Soc.* **2011**, *133* (27), 10612–10620. https://doi.org/10.1021/ja2029415.

(8) Moroz, P.; Liyanage, G.; Kholmicheva, N. N.; Yakunin, S.; Rijal, U.; Uprety, P.; Bastola, E.; Mellott, B.; Subedi, K.; Sun, L.; et al. Infrared Emitting PbS Nanocrystal Solids through Matrix Encapsulation. *Chem. Mater.* **2014**, *26* (14), 4256–4264. https://doi.org/10.1021/cm501739h.

(9) Mangum, B. D.; Landes, T. S.; Theobald, B. R.; Kurtin, J. N. Exploring the Bounds of Narrow-Band Quantum Dot Downconverted LEDs. *Photonics Res.* **2017**, *5* (2), A13–A22. https://doi.org/10.1364/PRJ.5.000A13.

(10) Hendricks, M. P.; Campos, M. P.; Cleveland, G. T.; Plante, I. J.; Owen, J. S. A Tunable Library of Substituted Thiourea Precursors to Metal Sulfide Nanocrystals. *Science* **2015**, *348* (6240), 1226–1230.

(11) Campos, M. P.; Hendricks, M. P.; Beecher, A. N.; Walravens, W.; Swain, R. A.; Cleveland, G. T.; Hens, Z.; Sfeir, M. Y.; Owen, J. S. A Library of Selenourea Precursors to PbSe Nanocrystals with Size Distributions near the Homogeneous Limit. *J. Am. Chem. Soc.* **2017**, *139* (6), 2296–2305. https://doi.org/10.1021/jacs.6b11021.

(12) Boercker, J. E.; Woodall, D. L.; Cunningham, P. D.; Placencia, D.; Ellis, C. T.; Stewart, M. H.; Brintlinger, T. H.; Stroud, R. M.; Tischler, J. G. Synthesis and Characterization of PbS/ZnS Core/Shell Nanocrystals. *Chem. Mater.* **2018**, *30* (12), 4112–4123. https://doi.org/10.1021/acs.chemmater.8b01421.

(13) Nasilowski, M.; Nienhaus, L.; Bertram, S. N.; Bawendi, M. G. Colloidal Atomic Layer Deposition Growth of PbS/CdS Core/Shell Quantum Dots. *Chem. Commun.* **2017**, *53* (5), 869–872. https://doi.org/10.1039/C6CC07403K.

(14) Yang, X.; Ren, F.; Wang, Y.; Ding, T.; Sun, H.; Ma, D.; Sun, X. W. Iodide Capped PbS/CdS Core-Shell Quantum Dots for Efficient Long-Wavelength near-Infrared Light-Emitting Diodes. *Sci. Rep.* **2017**, *7* (1), 14741. https://doi.org/10.1038/s41598-017-15244-5.

(15) Ning, Z.; Gong, X.; Comin, R.; Walters, G.; Fan, F.; Voznyy, O.; Yassitepe, E.; Buin, A.; Hoogland, S.; Sargent, E. H. Quantum-Dot-in-Perovskite Solids. *Nature* **2015**, *523* (7560), 324–328. https://doi.org/10.1038/nature14563.

(16) Gong, X.; Yang, Z.; Walters, G.; Comin, R.; Ning, Z.; Beauregard, E.; Adinolfi, V.; Voznyy, O.; Sargent, E. H. Highly Efficient Quantum Dot Near-Infrared Light-Emitting Diodes. *Nat. Photonics* **2016**. https://doi.org/10.1038/nphoton.2016.11.

(17) Noda, Y.; Ohba, S.; Sato, S.; Saito, Y. Charge Distribution and Atomic Thermal Vibration in Lead Chalcogenide Crystals. *Acta Crystallogr. B* **1983**, *39* (3), 312–317.

(18) Poglitsch, A.; Weber, D. Dynamic Disorder in Methylammoniumtrihalogenoplumbates (II) Observed by Millimeter-Wave Spectroscopy. *J. Chem. Phys.* **1987**, *87* (11), 6373. https://doi.org/10.1063/1.453467.

(19) Liu, M.; Johnston, M. B.; Snaith, H. J. Efficient Planar Heterojunction Perovskite Solar Cells by Vapour Deposition. *Nature* **2013**, *501* (7467), 395–398. https://doi.org/10.1038/nature12509.

(20) Li, G.; Tan, Z.-K.; Di, D.; Lai, M. L.; Jiang, L.; Lim, J. H.-W.; Friend, R. H.; Greenham, N. C. Efficient Light-Emitting Diodes Based on Nanocrystalline Perovskite in a Dielectric Polymer Matrix. *Nano Lett.* **2015**, *15* (4), 2640–2644. https://doi.org/10.1021/acs.nanolett.5b00235.

(21) Zhu, H.; Fu, Y.; Meng, F.; Wu, X.; Gong, Z.; Ding, Q.; Gustafsson, M. V.; Trinh, M. T.; Jin, S.; Zhu, X.-Y. Lead Halide Perovskite Nanowire Lasers with Low Lasing Thresholds and High Quality Factors. *Nat. Mater.* **2015**, *14* (6), 636–642. https://doi.org/10.1038/nmat4271.

(22) Dirin, D. N.; Dreyfuss, S.; Bodnarchuk, M. I.; Nedelcu, G.; Papagiorgis, P.; Itskos, G.; Kovalenko, M. V. Lead Halide Perovskites and Other Metal Halide Complexes as Inorganic Capping Ligands for Colloidal Nanocrystals. *J. Am. Chem. Soc.* **2014**, *136* (18), 6550–6553. https://doi.org/10.1021/ja5006288.

(23) Derjaguin, B. V.; Churaev, N. V.; Muller, V. M. The Derjaguin—Landau—Verwey—Overbeek (DLVO) Theory of Stability of Lyophobic Colloids. In *Surface Forces*; Derjaguin, B. V., Churaev, N. V., Muller, V. M., Eds.; Springer US: Boston, MA, 1987; pp 293–310. https://doi.org/10.1007/978-1-4757-6639-4_8.

(24) Dimroth, K.; Reichardt, C.; Siepmann, T.; Bohlmann, F. Über Pyridinium-N-phenol-betaine und ihre Verwendung zur Charakterisierung der Polarität von Lösungsmitteln. *Justus Liebigs Ann. Chem.* **1963**, *661* (1), 1–37. https://doi.org/10.1002/jlac.19636610102.

(25) Tunuli, M. S.; Rauf, M. A.; Farhataziz. Dimroth's ET(30) as Parameters of Solvent Polarity: A Caveat. *J. Photochem.* **1984**, *24* (4), 411–413. https://doi.org/10.1016/0047-2670(84)80023-4.

(26) Gutmann, V. Solvent Effects on the Reactivities of Organometallic Compounds. *Coord. Chem. Rev.* **1976**, *18* (2), 225–255. https://doi.org/10.1016/S0010-8545(00)82045-7.

(27) Mayer, U.; Gutmann, V.; Gerger, W. The Acceptor Number — A Quantitative Empirical Parameter for the Electrophilic Properties of Solvents. *Monatshefte Für Chem. Chem. Mon.* **1975**, *106* (6), 1235–1257. https://doi.org/10.1007/BF00913599.

(28) Semonin, O. E.; Elbaz, G. A.; Straus, D. B.; Hull, T. D.; Paley, D. W.; van der Zande, A. M.; Hone, J. C.; Kymissis, I.; Kagan, C. R.; Roy, X.; et al. Limits of Carrier Diffusion in N-Type and p-Type CH3NH3PbI3 Perovskite Single Crystals. *J. Phys. Chem. Lett.* **2016**, *7* (17), 3510–3518. https://doi.org/10.1021/acs.jpclett.6b01308.

(29) Zhu, H.; Miyata, K.; Fu, Y.; Wang, J.; Joshi, P. P.; Niesner, D.; Williams, K. W.; Jin, S.; Zhu, X.-Y. Screening in Crystalline Liquids Protects Energetic Carriers in Hybrid Perovskites. *Science* **2016**, *353* (6306), 1409–1413. https://doi.org/10.1126/science.aaf9570.

(30) Joshi, P. P.; Maehrlein, S. F.; Zhu, X. Dynamic Screening and Slow Cooling of Hot Carriers in Lead Halide Perovskites. *Adv. Mater. 0* (0), 1803054. https://doi.org/10.1002/adma.201803054.

(31) Jasieniak, J.; Califano, M.; Watkins, S. E. Size-Dependent Valence and Conduction Band-Edge Energies of Semiconductor Nanocrystals. *ACS Nano* **2011**, *5* (7), 5888–5902. https://doi.org/10.1021/nn201681s.

(32) Schulz, P.; Edri, E.; Kirmayer, S.; Hodes, G.; Cahen, D.; Kahn, A. Interface Energetics in Organo-Metal Halide Perovskite-Based Photovoltaic Cells. *Energy Environ. Sci.* **2014**, *7* (4), 1377. https://doi.org/10.1039/c4ee00168k.

(33) Brown, P. R.; Kim, D.; Lunt, R. R.; Zhao, N.; Bawendi, M. G.; Grossman, J. C.; Bulovi, V. Energy Level Modi Fi Cation in Lead Sul Fi de Quantum Dot Thin Films through Ligand Exchange. *ACS Nano* **2014**, *8*, 5863–5872. https://doi.org/10.1021/nn500897c.

(34) Glaser, T.; Müller, C.; Sendner, M.; Krekeler, C.; Semonin, O. E.; Hull, T. D.; Yaffe, O.; Owen, J. S.; Kowalsky, W.; Pucci, A.; et al. Infrared Spectroscopic Study of Vibrational Modes in Methylammonium Lead Halide Perovskites. *J. Phys. Chem. Lett.* **2015**, *6* (15), 2913–2918. https://doi.org/10.1021/acs.jpclett.5b01309.

(35) Yaffe, O.; Guo, Y.; Tan, L. Z.; Egger, D. A.; Hull, T.; Stoumpos, C. C.; Zheng, F.; Heinz, T. F.; Kronik, L.; Kanatzidis, M. G.; et al. Local Polar Fluctuations in Lead Halide Perovskite Crystals. *Phys. Rev. Lett.* **2017**, *118* (13), 136001. https://doi.org/10.1103/PhysRevLett.118.136001.

Chapter 2. Single particle fluorescence studies of CdE heterostructures: influence of internal and surface structure

TABLE OF CONTENTS

2.1. Introduction

2.1.1. Single particle fluorescence

Understanding the dynamics of light emission has been a central focus of quantum dot (QD) studies as better understanding of parasitic processes has helped develop design principles that create more efficient QD emitters.[1–6] Ensemble measurements, though more practical and more closely tied to real-world applications, must be supplemented by measurements of single particles, to understand how the microstructures affect macro effects. The most striking example of the importance of single particle measurements is the discovery of fluorescent intermittency or "blinking"[7,8], an effect that is not possible to see in ensemble measurements. Single particle measurements represent an exciting opportunity to more deeply understand the dynamic processes that lead to QD optical degradation[9–11] and LED droop[12–14] in specific architectures. For example, there is still debate over the model of blinking[15–18], as simple charging[19] and Auger models[20] do not completely capture the power law statistics found in most samples.

2.2. Measurement and Data Analysis Techniques

2.2.1. Instrumentation and Data format

Single particle measurements were made on a Picoquant Microtime200 Time Correlated Single Photon counting (TCSPC) confocal fluorescence microscope. A 405 nm pulsed laser (also with continuous wave capability) is fiber coupled into the optical unit and directed through a beam splitter to a CCD camera to enable focusing the objective. The remaining laser light is guided to a dichroic filter and into the microscope objective. Fluorescence signal is collected out of the same objective, through the dichroic and a 450 nm long pass filter before hitting a pinhole (30-150 µm) aligned to the focus of the objective to reduce the sampling volume. The filtered fluorescence signal is then collected on two single photon avalanche diodes (SPADs) with an optional 50/50 beam splitter.

Figure 1

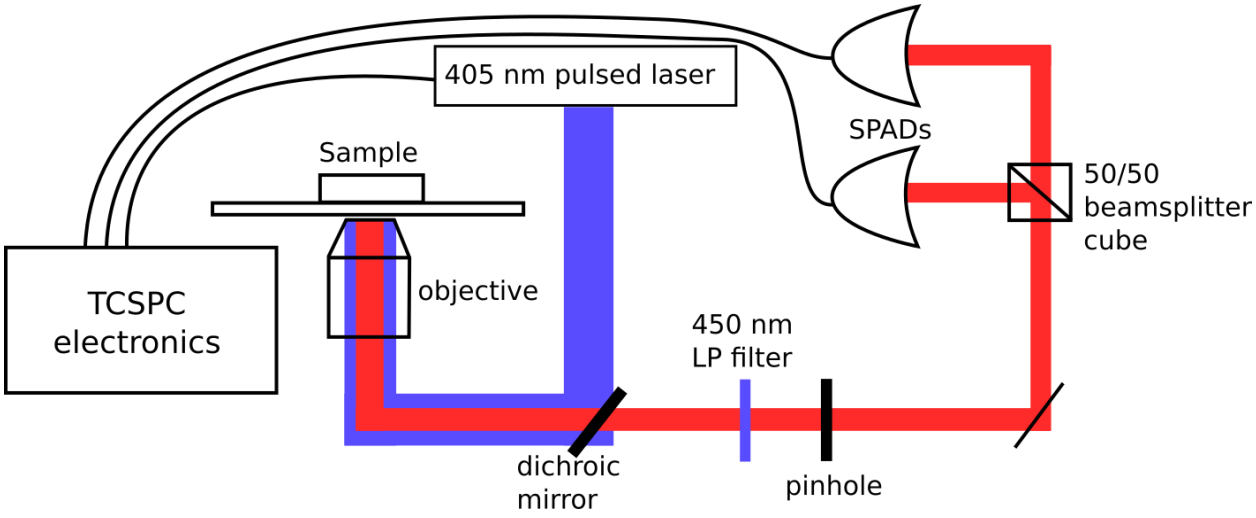

Schematic of Picoquant Microtime200 confocal TCSPC microscope.

The data is recorded in what is known as Time Tagged Time-Resolved mode[21], where the TCSPC electronics begin the timing "stop watch" when a laser pulse is produced, and end the timing when a photon is detected at one of the SPADs (Figure 2). The data is recorded in a Picoquant specific data format called .ptu designed for fast writing from the computer. This file contains an initial header with information about the measurement and hardware, then an array of photon data with the time of the laser pulse, the so-called "nanotime" which is the time between the laser pulse and the detected photon, the identity of the detector, and a special bit used for parsing the photon data. This format is known as T3, while another format T2 measures the beginning of the experiment as the "stopwatch" start and the photon arrival as the stop, ignoring the laser pulses and only counting the absolute time of the photon arrival. Importantly, as we'll see, T3 measurements can easily be converted to T2 format.

Figure 2

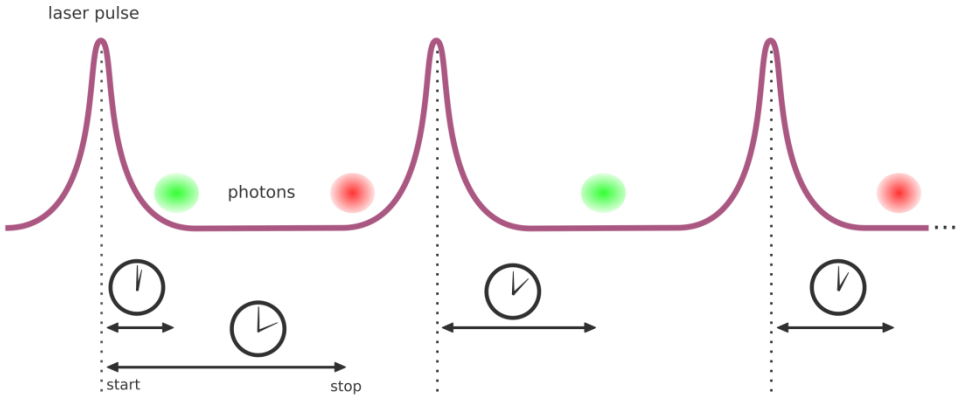

schematic of time-tagged time resolved photon arrival data recording process. Green and red dots are photons arrivals at detector 1 and 2, respectively. The two photons emitted after the first laser pulse may be due to multiple particles or biexciton emission, as discussed below

The product of this data is, essentially, a list of photons and the time they arrived. These data can be used in a variety of ways through binning and correlation to understand the time dynamics of the fluorescent probe. Unfortunately, this setup does not have a spectrometer, so the SPADs

also detect fluorescent photons from dark counts, reflections, SPAD afterglow, and defects on the glass substrate. It is important to keep these effects in mind during the data analysis.

To help understand the data presented in this section, here I will introduce the analytical methods and how they are derived from photon arrival times.

2.2.2. Photoluminescence lifetime:

Photoluminescence lifetime histograms are among the most common applications of TCSPC data. These plots are generated by making a histogram of the nanotimes, i.e. the time between the laser pulse and the detected photon. The basic experiment is to excite a fluorophore, and see how long it takes for it to emit a photon. The data only becomes meaningful when this measurement is repeated millions of times and analyzed statistically. The resulting histogram is fit to a combination of exponential functions, though ideal behavior is monoexpential, indicating one process controlling the photoluminescence output with some characteristic decay time. Generally quantum dots are bi- or tri-exponential, especially on substrates, due to charging, multiexciton behavior, trapping, and other non-radiative processes.[22,23]

Figure 3

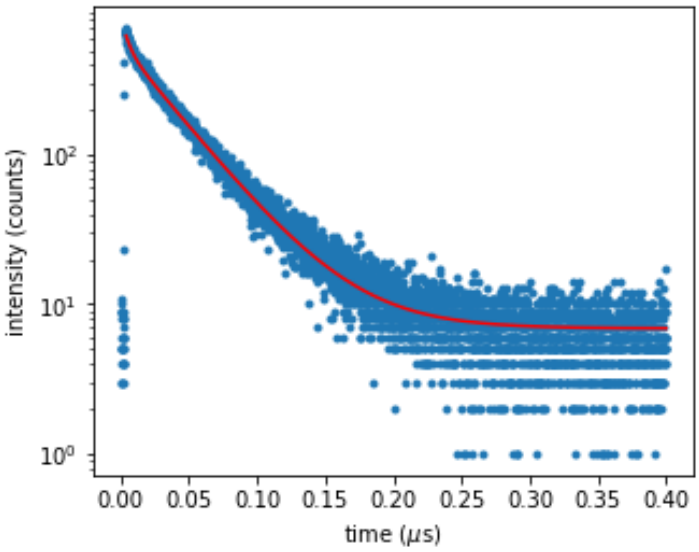

Photoluminescence lifetime decay histogram

2.2.3. Photoluminescence time trace:

Time traces are measures of the intensity of fluorescence over time. Since fluorescence intensity is itself a measure of the number of photons over a given time, we need to create another histogram. This time we are creating bins of some arbitrary width, generally between 10-100 ms, and counting the photons from their arrival time since the beginning of the experiment. These plots contain a Poisson distribution of photon intensities, in addition to fluorescence intermittency or "blinking" behaviors. When a single particle is measured, non-radiative processes cause the intensity to drop to zero, or sometimes to an intensity level between "on" and "off" states, which may be due to improper binning or so called "gray" states that are weakly emissive.[17,24] It's important to note that blinking itself is not *proof* that you are measuring a single particle, though it is useful to help find likely single particles. Blinking is a universal process, all fluorescent particles blink[8], though reduced blinking quantum dots have been designed and intensely researched[1,25]. The arbitrary bin width mentioned earlier is an important

parameter to consider when analyzing time traces. Bins need to be long enough to hold statistical significance, e.g. distinguishing "off" and "on" states, but should not be so long that they obscure faster dynamics, e.g. if the fluorophore switches from "on" to "off" halfway through the bin and produces a "grey" state that exists not due to some intrinsic process, but from the choice of bin width.[24]

Figure 4

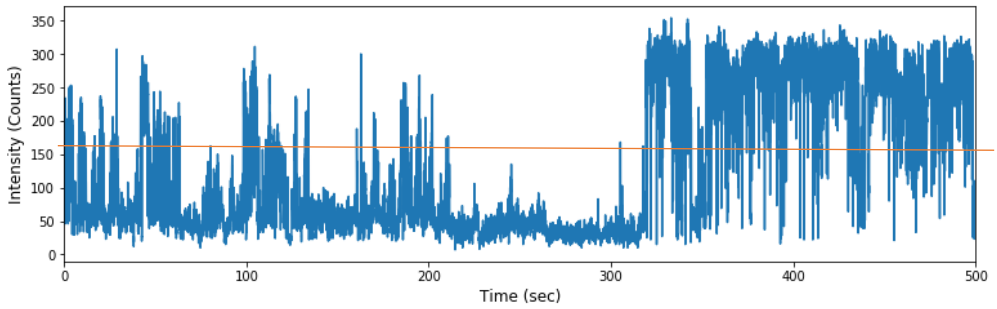

Example fluorescence intensity time trace with clear blinking behavior

2.2.4. Fluorescence Lifetime Intensity Distribution:

Depending on the size of the bin width, more data analysis can be done on the photons *within* each time trace bin. One helpful method is to see how the fluorescence lifetime and intensity behavior correlate to one another. This is commonly represented in fluorescence lifetime intensity distribution (FLID) heat plots[10,11]. These are calculated by calculating the lifetime histogram and fitting within the time trace bins, then plotting that against the intensity of said bin. Several reports have used this technique to draw distinctions between different particle blinking behavior. One can also create thresholds in intensity to analyze the lifetime behavior of a given fluorescent state. Interestingly the "on" state of QDs is nearly always a monoexponential.

2.2.5. Statistical behavior of fluorescence intermittency

Understanding the temporal fluctuations in intensity is important to understanding the behavior of fluorescent particles in real applications where they will, more than likely, be expected to produce fluorescence over some time. While some insight into this behavior can be gleaned by inspecting fluorescence time traces, greater insight is found in statistically analyzing these plots. To do this we will "digitize" these data, by assigning a threshold intensity to define "on" fluorescent states above and "off" dark states below (red line, Figure 4, for example). We can then calculate the probability function of staying in the "on" or "off" state using Equation 1 (Note that *on* can be replaced with *off* to calculate the probability of off states).

Equation 1: $$P(t_{on}) = \frac{N(t_{on})}{N_{on}^{tot}} \frac{1}{\delta t_{on}^{avg}}$$

For QD blinking traces the probability statistics, when plotted against the on/off time t follow power law statistics[20], according to equation 2 and seen in the fit to Figure X. Again, power law statistics *do not* fit Auger or charging models of blinking, and there is still no consensus around the correct model to use for fluorescence intermittency.[15–17,19,20]

Equation 2: $$P(t) \propto t^{-\beta}$$

2.2.6. Power dependence of blinking statistics

While off-state probabilities are generally well described by power law statistics, deviations can occur in on-state behavior due to the contribution of multiple excited charges (multiexcitons)[26]. This introduces an exponential cut-off at longer times, given in Equation 3, presumably due to the non-radiative recombination of multiexcitons dominating other processes.

Equation 3: $$P(t) \propto t^{-\beta} e^{-\frac{t}{\alpha}}$$

Since the probability of generating multiexcitons is proportional to the photon flux,[27] higher laser power generally produces a more distinct exponential cutoff. This behavior can be seen at low laser power, depending on the sample architecture, but is less common.

2.2.7. Second order cross correlation:

Correlating photon arrival times is another useful tool in analyzing TCSPC data.[21] Correlation spectroscopy has been used extensively in biological fields to study rotational dynamics,[28,29] protein ligand interactions,[30] and other useful diffusion information.[31]Using Equation 4, the fluorescence intensity is correlated between detector 1 and detector 2, thus each data point in Figure 5 represents *two* detected photons, and the value on the x-axis is the time delay between them. Correlation were performed using a python script based on an algorithm developed by Laurence *et al.*[32]

Equation 4: $$G^2(t) = \sum_{i=0}^{M-m} \frac{I_1(i\tau)\, I_2(i\tau+m\tau)}{\langle I_1\rangle\langle I_2\rangle\,(M-m)}$$

Here the intensity I over time t is calculated in bins of width τ. M is the total number of bins, and m is an integer such that mτ = Δt. 1 and 2 refer to the two SPAD detectors.

Obviously the most likely time spacing between two photons will be equal to the time between laser pulses, since the likelihood of fluorescence decays exponentially after an excitation. This method, measuring a single, stationary, fluorescent molecule and correlating its fluorescence intensity with linear time delay bins, is often known as antibunching because it is a useful tool for determining if an emitter is indeed a single particle.[33]

Figure 5

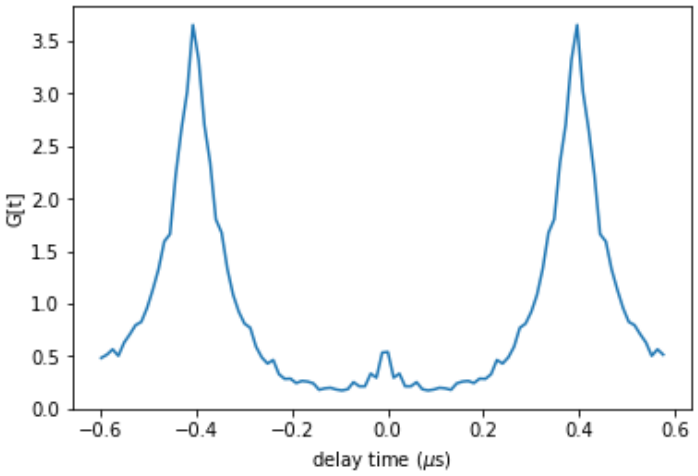

Example correlogram showing clear photon antibunching i.e. near zero signal at 0 delay time.

For most fluorophores, only one electron can be excited at a time, so there should be no correlation with delay times less than the rep-rate of the laser, (if there is more than one particle the greatest correlation amplitude should be at 0 decay time, for the same reasons that decay times of +/- 1 rep rate have high correlation amplitude). QD band edges, however, are degenerate, and higher energy levels are close enough to the band edge to accommodate several electrons at a time[22,34,35], so multiexcitonic contributions can lead to correlation amplitude at 0 delay time[27]. Deconvoluting these effects is important when analyzing single particle fluorescence data of QDs, and offers an opportunity to study the recombination efficiency of multiexciton processes.[36]

2.2.8. Time-gating

Figure 6

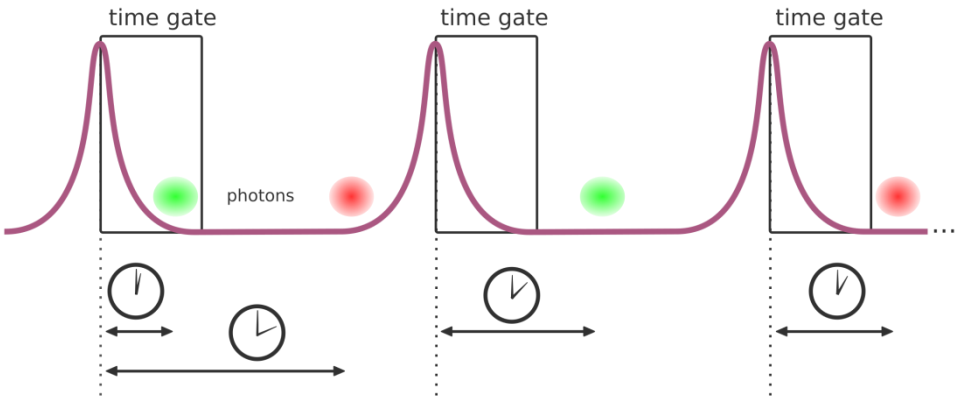

Cartoon illustrating time gating data analysis. The photons within the time gate box will be discarded.

Due to the sensitivity of the single photon counting avalanche diodes (SPADs) single particle fluorescence is a powerful tool for measuring single particles and debris, dust, and other foreign contaminants that fluorescence slightly under laser excitation. Because the particles measured in this work are deposited from solution, aggregation is common, and must be accounted for. This is especially true for larger nanocrystals, where aggregation is common under certain conditions, such as dilute solution. Second order cross-correlation measurements are commonly used to determine the single particle nature of emitters,[33] but an additional data processing step is needed to rule out multiexciton contributions. Because biexciton emission occurs one photon after the other[37,38] applying a time gate, i.e. discarding photons that are recorded sometime after the laser pulse, (see Figure 6) can remove multiexciton contributions from the correlograms.[39] As seen in Figure 7 this leads to clear antibunching, unambiguously proving the measurement was made on a single QD. Ensuring the lifetime decay of the single particle vs ensemble resemble one another is also useful in double-checking the measurement is made on the target fluorophore.

Figure 7

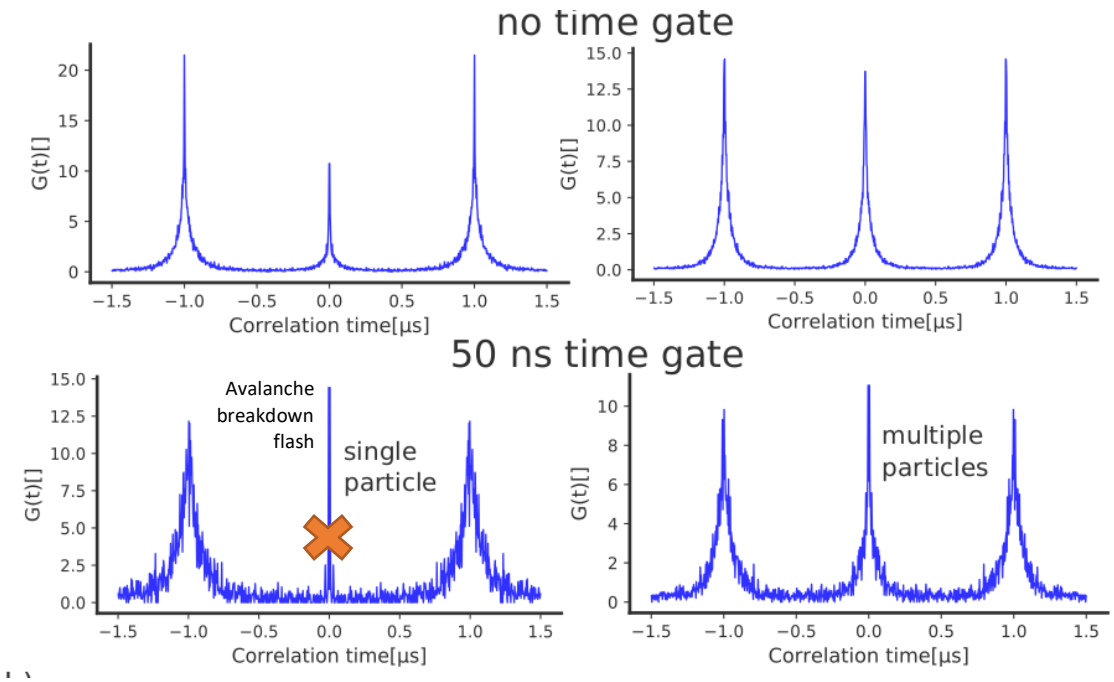

The calculation of time-gated correlograms represents a major limitation of Picoquant Symphotime64 data analysis software. This analytical technique is not required by most biological scientists using the instruments (a majority of purchasers) so not only has this not been implemented in the software, the ability to do them separately does not exist due to the different data acquisition file formats used. Software designed to interconvert these formats (T3 for delay time, T2 for absolute arrival time, though confusingly both use the same .ptu file extension) and, optionally, perform time gating, was created for this study. The data presented in this thesis, including time-gated correlograms, was calculated and manipulated using a different software suite also created by the author for this study, that is more versatile. More information can be found in Appendix 1 and both software source codes can be found at www.github.com/trevhull.

2.2.9. Photon avalanche breakdown

The strong, sharp correlation signal at 0 delay time in the time-gated single QD correlogram in Figure 7 lacks the exponential slope found from photoluminescence decay processes and can easily be determined to be an instrument response, not a signal from the fluorescence of the particles.[39] The signal likely arises from reflections within the optical box, and from the photon avalanche breakdown flash of the SPAD detectors. A small percentage of photon detection events create, through the physical process of the SPAD avalanche detection, an additional photon emitted from the silicon detectors. This photon then can travel through the optical path and register a signal on the second detector.

Since the characteristic delay time of the photons are due to the time the photon is required to travel through the optical path, any avalanche breakdown photon will be correlated to real fluorescence photons (or dark counts, in fact *any* photon detected can create a breakdown flash) the delay time of these photons will *always* be identical, leading to the high correlation amplitude. Time gating cannot remove the signal, in fact it *enhances* it, by removing contributions from actual fluorescence photons. Biexciton contribution can be removed because biexciton photons have a very short lifetime, and always are emitted one after another[37,38,] while avalanche photons do not depend on the time since the laser pulse, only on the time since the last *photon* (i.e. a photon emitted outside of the time gate can emit breakdown photon with characteristic correlation delay time as equally as a photon within a timegate can.)

Efforts to remove this signal include use of fluorescence filters, asymmetric data analysis (the avalanche breakdown itself is slightly asymmetric in our system, since one detector has a larger active area than the other, it is more likely to detect breakdown photons) and background subtraction. None of these methods has proven sufficient, but better background subtraction

methods could be implemented. The most effective reduction of this signal occurs in samples with much higher signal-to-noise, where the correlograms are dominated by QD photoluminescence.

2.3. Spherical Quantum Wells

The spherical quantum well architecture is designed to avoid interfacial strain defects by synthesizing an emissive (CdSe) layer so thin that it conforms to the crystal lattice of the shell (CdS). The thickness of the CdSe layer will influence the energy of the electronic transitions, but must below the critical thickness[40], i.e. the thickness above which strain defects form. This SQW architecture was chosen by the Owen lab to serve as blue-to-red downconverters for a collaboration with a LED manufacturer.

2.3.1. Synthesis

The synthesis of these particles is reported elsewhere.[41,42] For more in-depth understanding of the particle synthesis and performance on LED chips, the reader is referred to the thesis of Iva Rreza. Briefly, a co-solution of thiourea and selenourea precursors were injected into a solution of cadmium oleate in octadecene. The rates of the precursors were chosen to produce a core/shell CdS/CdSe particle with a thin CdSe outer layer. The particles were then shelled using a solution of cadmium oleate, thiourea, and trioctylphosphene, injected via syringe pump over a few hours.

2.3.2. Shell size dependence

The structure of these spherical quantum wells has a number of degrees of freedom. Changes to the core size, emissive quantum well thickness (as long as it is below the critical thickness),

shell thickness, and the composition of all of these things are useful levers for affecting the optical properties of the material. Here we will focus on three samples, only varying in the thickness of the outermost protective shell. The most impressive feature of the SQW, and the reason they were chosen for this application, was the ability to increase the shell size without lowering the photoluminescence quantum yield.[40]

Figure 8

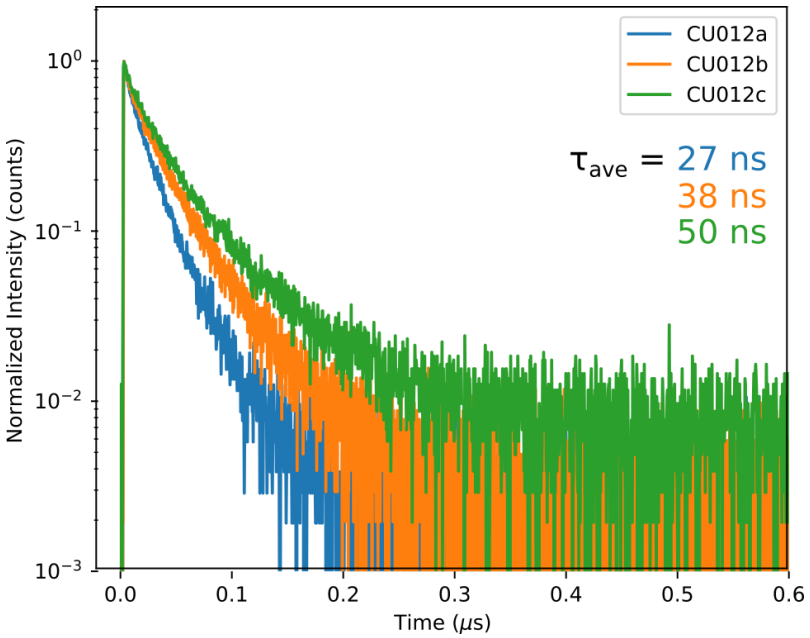

PL lifetime decay histograms of CU012a,b,c series with increasing shell thickness from a to c. Average lifetime values provided

Ensemble, solution phase photoluminescence lifetime traces seen in Figure 8 show a clear trend in the average lifetime of the 3 samples; charges last longer in the sample with the largest shell. This can be helpful in identifying promising device candidates since non-radiative processes and lower quantum yield photoluminescence states generally are fast decaying.[23]

2.3.3. Biexciton Quantum Yield

Single particle measurements were also performed, and clear trends are found in the second order cross correlation calculation of the biexciton quantum yield. Samples of CU012c (the largest SQW samples, particle diameter ~ 11nm) have single particle BXQY around 30% (assuming a single exciton "on" state QY of 1 [27]), whereas the CU012a samples show almost complete antibunching. Quantifying the BXQY of samples CU012a and b becomes difficult due to the sharp photon avalanche breakdown signal in the correlograms at 0 time delay, as discussed previously in section 2.2.9. However, we can conservatively say that the BXQY of CU012a is less than 1%. CU012b correlograms have a strong breakdown signal, but also appear to have some signal from biexciton photons, based on the shape of the center peak. We'll again make a conservative estimate and say the BXQY of this sample is *less than* 10% (which is the value of the two-sided exponential fit).

Figure 9

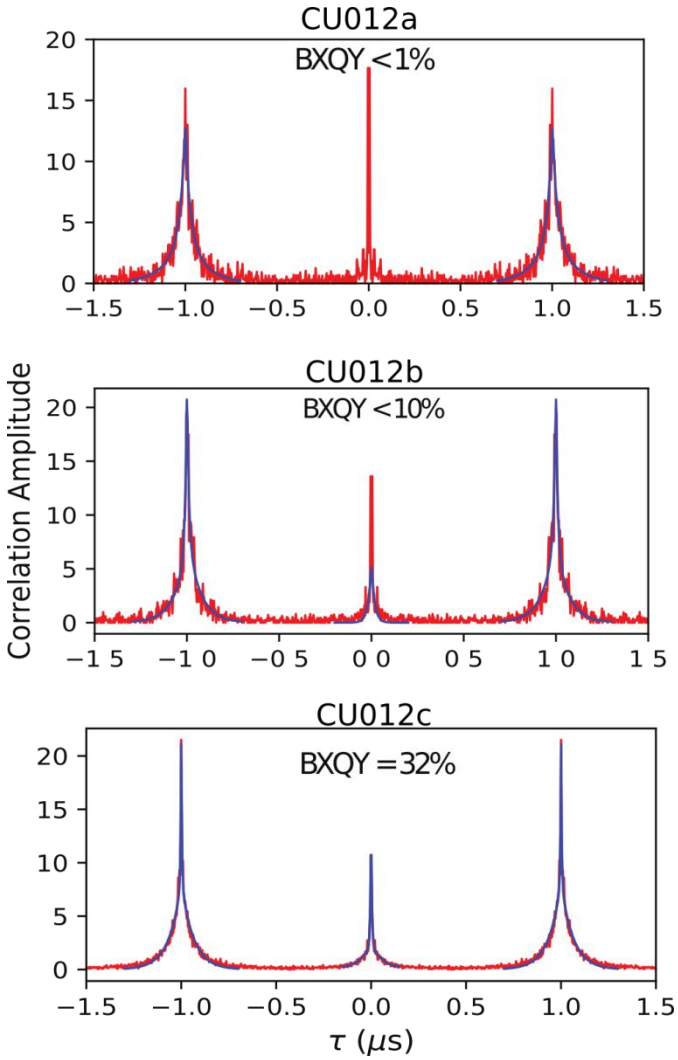

Second order cross correlograms of CU012a,b and c (top to bottom) with included double-sided exponential fits of the +/- 1 rep rate peaks and the central "biexciton" peak.

This trend would be expected based on better isolation of the emissive CdSe layer from potential surface trap states or substrate charges. There may also be an effect of the particle volume. Since multiple excitations are statistically guaranteed at these laser powers[34] these results suggest that CU012c is more efficient at converting multiple excitations into photons than CU012b or a, an indication that non-radiative Auger processes are diminished with larger shell size.

2.3.4. Blinking Statistics

Despite the differences in BXQY, the ensemble PLQY of these samples are comparable (Table 1) which may suggest more complicated, and varying, dominant non-radiative decay pathways, or a discrepancy in blinking behavior. Fluorescence time trace measurements (figure 10, Table 1) and subsequent analysis of the blinking statistics yield further insight into the non-radiative processes of these samples.

Figure 10

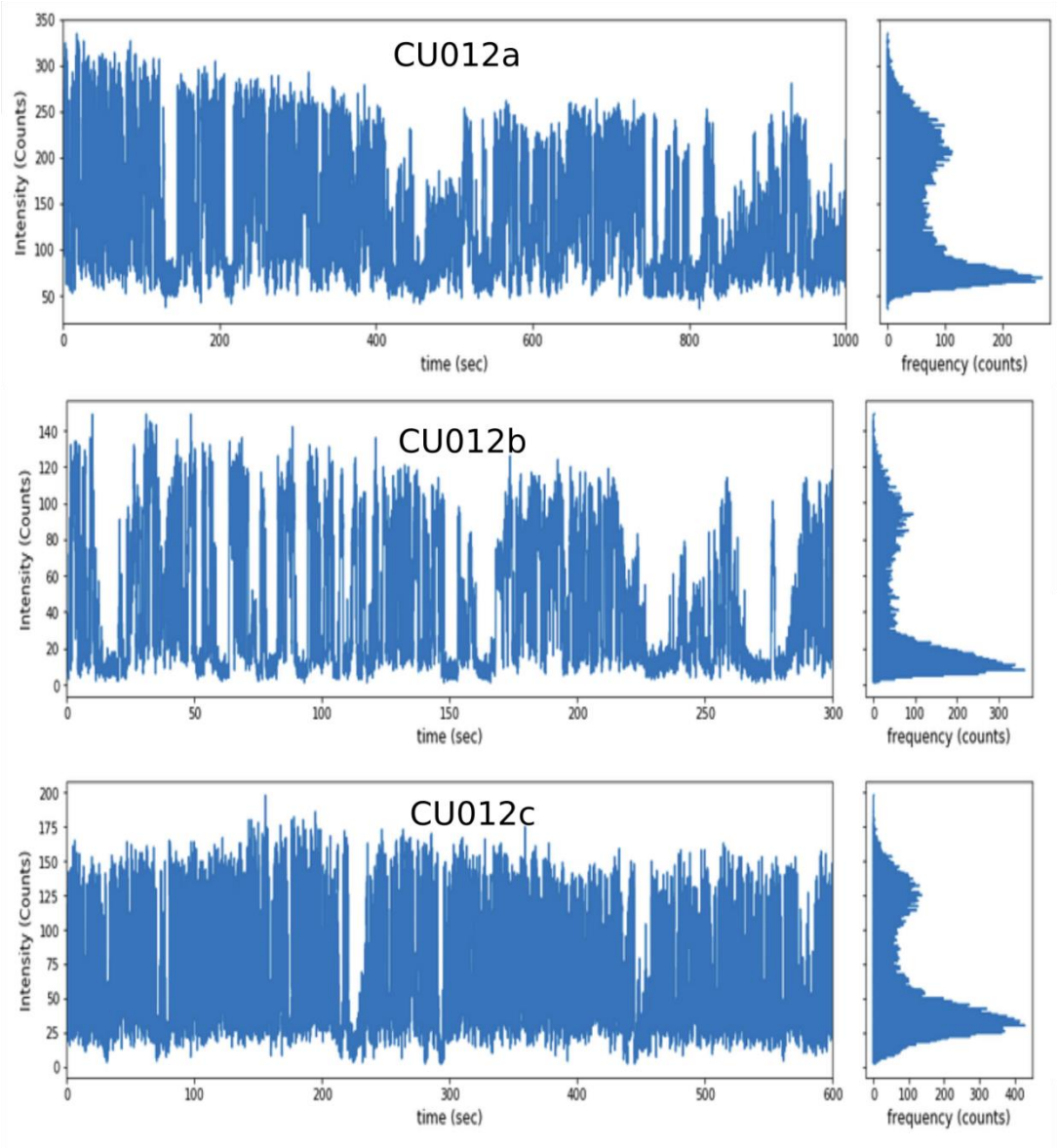

Fluorescence time traces of CU012a, CU012b, and CU012c. bin width = 30 ms.

Representative time traces of the samples can be hard to interpret on their own, however it's clear there is a significant "off" fraction in all samples. The on/off fractions are reported in Table 1, and do not vary greatly, although CU012c has the greatest "on" time. Another noticeable feature of these time traces is significant intensity between the "on" and "off" states, this is sometimes attributed to an intermediate "grey" state or a feature of dynamics [26]

Figure 11

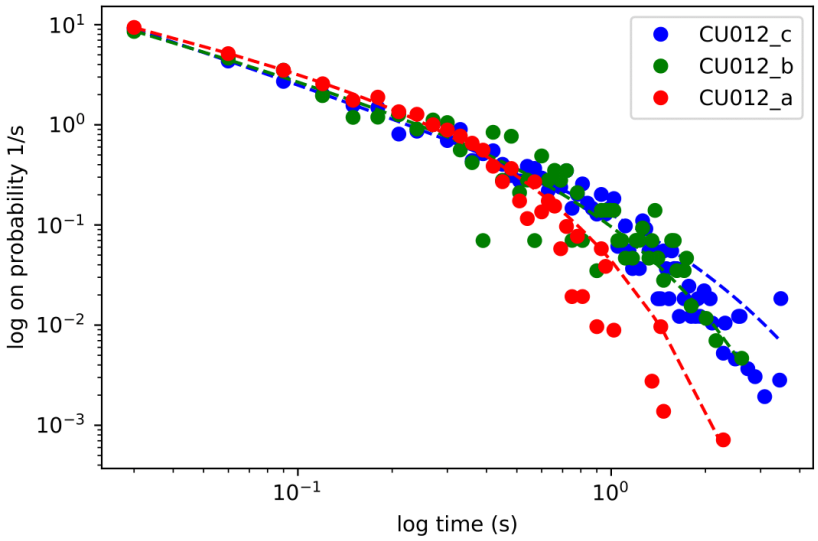

On time probabilities calculated from blinking traces in Figure 10 of CU012,a,b,c samples with increasing shell size from a to c

The "on" state statistics of the three samples (Figure 11) are fit to power law function with an exponential cutoff, Equation 3, a signature of multi-exciton contributions[26] (see discussion above in 2.2.6). Fit values are reproduced in Table 1. Corroborating the BXQY measurements, the "on" time of CU012a is most affected by multiexciton contributions (as seen by the more dramatic curve to lower probabilities, and in the higher value of α. While the exponential cutoff is dependent on the laser power, CU012a was measured at a *lower* laser power, which should *decrease* the effects of multiexciton contributions, and would likely produce a more dramatic

difference. CU012b and c were measured at the same laser power. CU012b and c have similar fit behavior, but CU012c has slightly higher "on" fraction, slightly smaller exponential cutoff, and, interestingly, a slightly higher power law exponent. The "off" probability of CU012b and c are nearly identical, while c has a much steeper "off" time probability, which may indicate faster switching between "on" and "off" states.

Figure 12

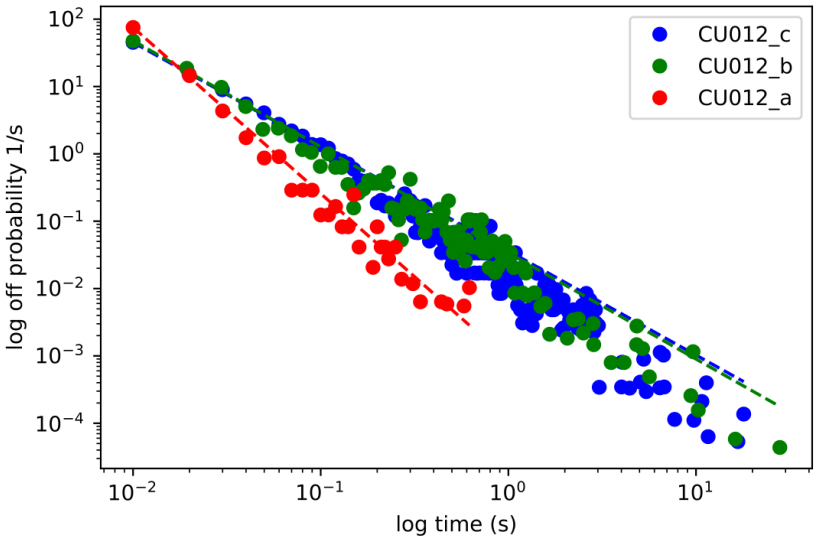

On time probabilities calculated from blinking traces in Figure 10 of CU012,a,b,c samples with increasing shell size from a to c

Taken together, these data point towards CU012c as an optimal candidate for stable, high performing QD downconverter at high LED flux, due to its relative resilience to multiexciton non-radiative and Auger processes. Surprisingly, data from the LED manufacturer collaborator indicates that CU012a performed the best on chip, nearly matching their proprietary standard for accelerated aging tests.[42]. The explanation for this seems to have something to do with the manufacturers additional processing steps, a ZnS shell deposition, and another "barrier layer" encapsulation. The details of these procedures are closely guarded trade secrets; however, we

will attempt to rationalize and analyze the performance of these samples using the single particle photoluminescence analysis tools at our disposal.

Table 1

Sample	Ensemble PLQY	"on" fraction	β on/off	α (sec)	Laser power (mw/cm^2)
CU012a	62%	0.45	0.73/2.47	1.3	24.14
CU012b	83%	0.41	0.89/1.58	0.45	44.92
CU012c	81%	0.49	1.01/1.55	0.48	44.41

2.3.5. Surface Chemistry effects on photoluminescence

Figure 13

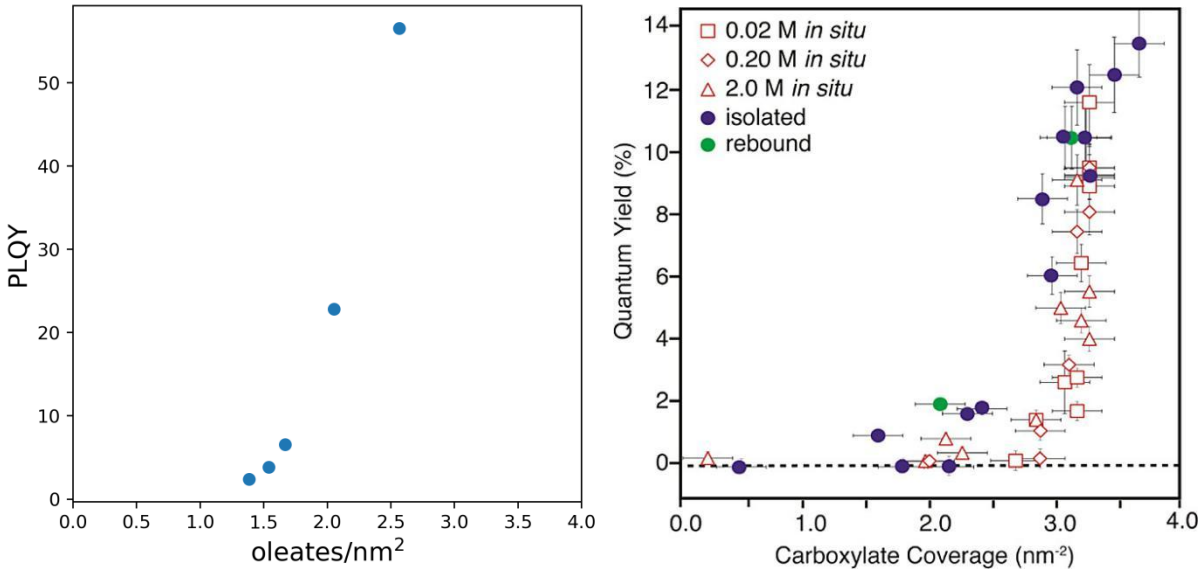

Left: Photoluminescence quantum yield as a function of surface ligand coverage of spherical quantum well. *Right*: PLQY as a function of ligand coverage for bare CdSe. Reprinted with permission from Anderson *et al.* JACS **2013**, 135 (49), 18536–18548. Copyright 2013 American Chemical Society

Before analyzing the behavior of the CU012a sample post-ZnS treatment, it is useful to consider the surface chemistry of QD emitters. The addition of shells to quantum dot emitters enables both a greater isolation of excited charges from their chemical environments, stronger confinement of wavefunctions, and passivation of mid-gap surface states. This has enabled the synthesis of high quantum yield particles with thick protective shells.[1,5,40] These core/shell particles, however, *still have surfaces* on the shells that may contribute to non-radiative recombination. It is interesting to compare the steep drop off in QY as the carboxylate coverage decreases, mirroring the same plot made by Anderson *et al.* on bare CdSe nanocrystals.[43]

2.3.6. Effect of ZnS Shelling

As seen in Figure 14, ZnS shelled SQW CU012a samples are much more stable emitters than before ZnS shelling. The overall lifetime PL decay nearly matches the "on" state, the monoexponential shape suggesting a single decay channel (Figure 16). Likewise, the QY improved to 86% and the "on" fraction of these particles is between 0.9 and 0.95 in all measured samples.

Figure 14

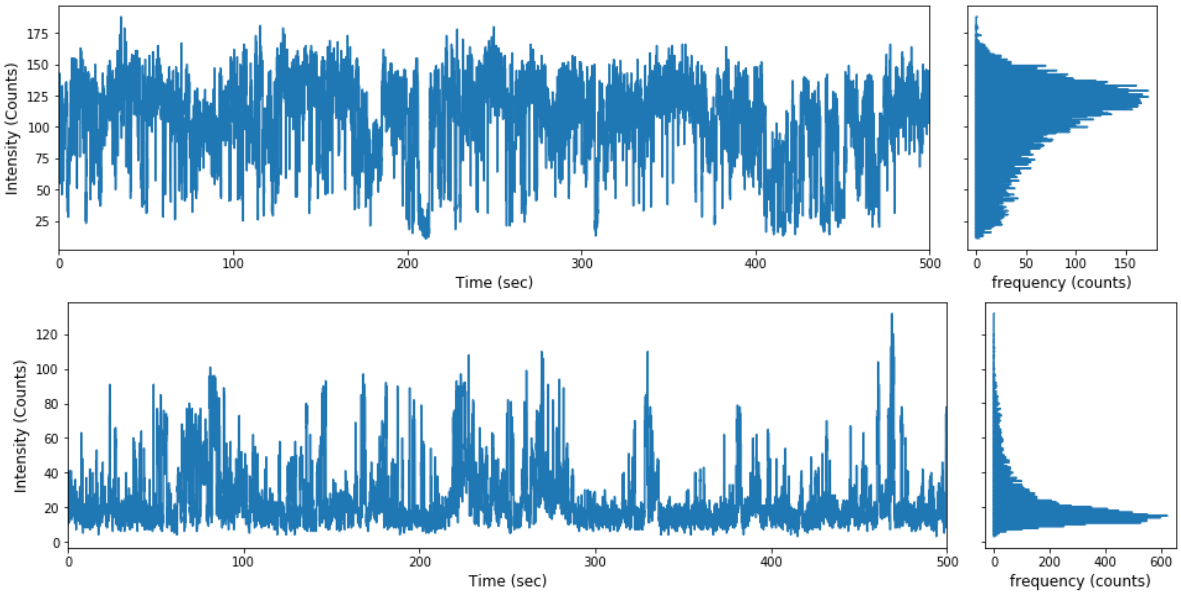

Blinking trace of CU014 ZnS shelled, representative blinking traces highlighting increased particle-to-particle variability

Preliminary results from TCSPC suggest higher particle-to-particle variability in larger SQW samples, such as CU04, where some particles photoluminescence intensity is nearly on par with CU012a, approaching 0.8 on fractions (Figure 14), whereas others are much more susceptible to off states (Figure 15). Likewise the "good" particles appear to have more intermediate fluorescence states (sometimes called grey states[17], or described as "flickering" when not as obviously binary switching[10]) than the smaller CUO12a. on time probability calculations also indicate multiexciton character (Additional Figures), despite a very low laser power. Ideally, a systematic study of the ZnS shelling treatment as a function of particle size and surface chemistry would be performed, however, given the proprietary nature of the chemistry, that study is unlikely to be reported.

Figure 16

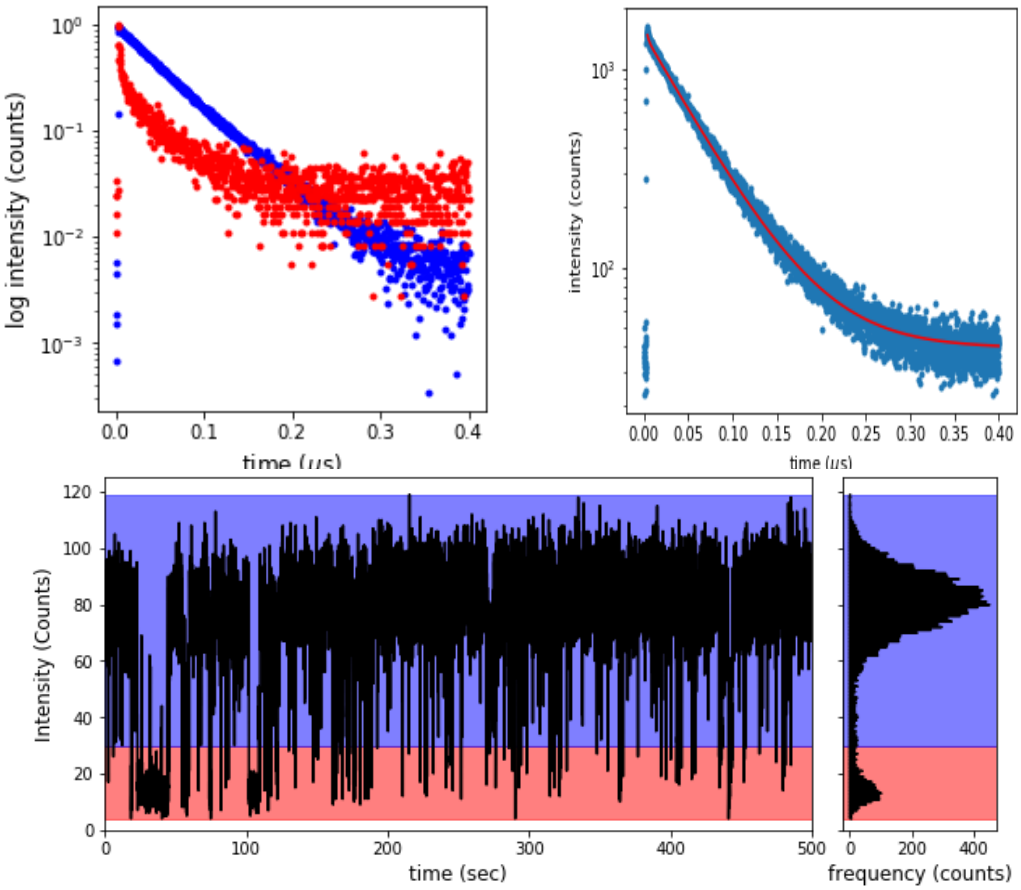

Top left: lifetime decay traces of the "on" (blue) and "off" (red) states of CU012a with ZnS Shell. *Top Right:* overall lifetime decay trace of particle, notice the primarily monoexponential shape *Bottom:* blinking trace with threshold between "on" (blue) and "off" (red)

The lack of visible BX signal in antibunching cannot due to increased Auger recombination, since the particle is so stable on-chip and has a high on-fraction. FLID plots show a clear linear relationship between the fluorescence intensity and lifetime, usually attributed to a blinking mechanism *that is not* due to Auger recombination, but some other trapping mechanism.[10,44] the linear lifetime scaling is attributed to a shallow trap state by Yuan et al, which may suggest an alternative dominant non-radiative mechanism, besides Auger recombination, in these ZnS shelled samples.[44]

Figure 17

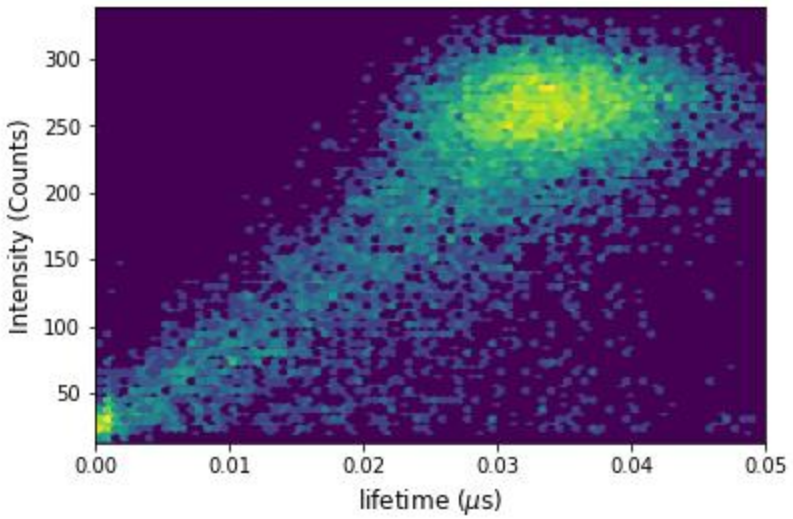

CU012a ZnS shell FLID heat map showing primarily linear lifetime scaling bin width 40 ms

Figure 18

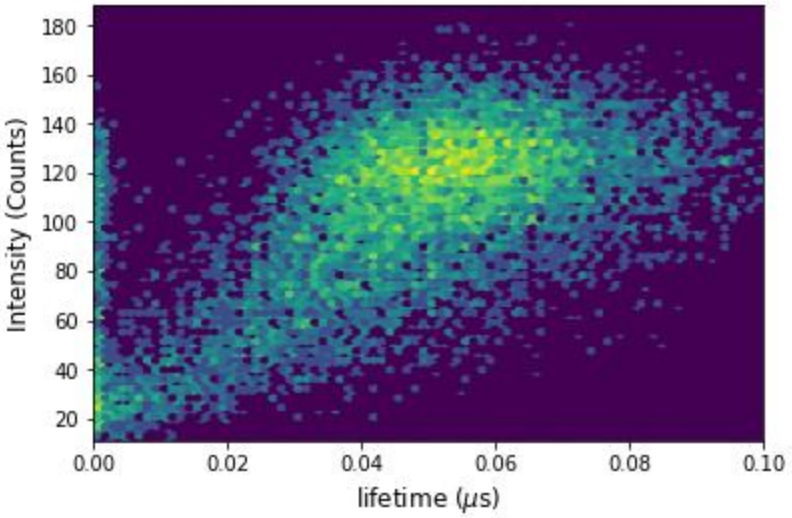

CU04 ZnS shell FLID heat map showing intermediate lifetime scaling bin width 50 ms

Figure 19

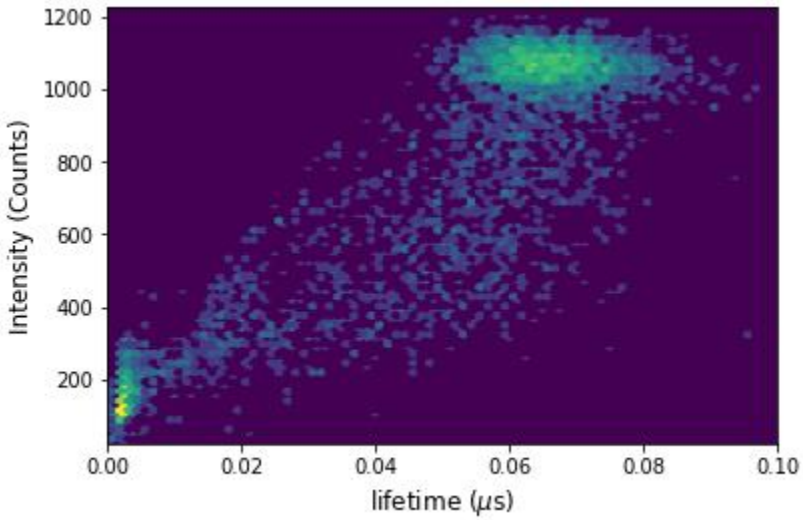

CU012c FLID heat map showing primarily exponential lifetime scaling, bin width 40 ms

2.4. Core/Shells

Ligand removal of core/shell CdSe/CdS particles also produced a sharp decreased in the photoluminescence quantum yield, showing the generality of the importance of the surface chemistry of the CdS shell, although the ligand concentrations were not calculated to see if the observed similarity of Figure 13 to bare CdSe is observed in binary core/shell systems as well.

2.5. Conclusion

TCSPC confocal fluorescence microscopy is a powerful tool for materials science when the proper data acquisition and analysis techniques are developed. The Picoquant Symphotime64 software has been extended through custom python scripts to help enable single particle studies of QDs.

To demonstrate the utility of this method, high performing SQW QD samples developed by colleagues were probed at the single particle level to better understand the influence of structural changes on fluorescence dynamics. The larger shell SQW seemed to more efficiently converting biexcitons into photons than thin shelled particles, thus avoiding Auger processes that would be detrimental in LED downconversion applications.

Proprietary encapsulation methods, however, seemed to change the behavior of these particles. As larger particles were incompatible with the methods, likely due to some unknown difference in surface structure. After incomplete deposition of ZnS, large particles exhibited very complicated fluorescence behavior, perhaps due to “islands” of ZnS, or other trap states introduced in the shelling procedure.

There is still much to learn about the fundamental processes controlling fluorescence intermittency, and thus limiting QD performance, especially at high flux. From this work it is clear that the surface chemistry of core/shell QDs is an important, and perhaps dominant, consideration. While internal architecture, composition, interfaces often get more attention the surface must not be neglected.

2.6. Additional Figures

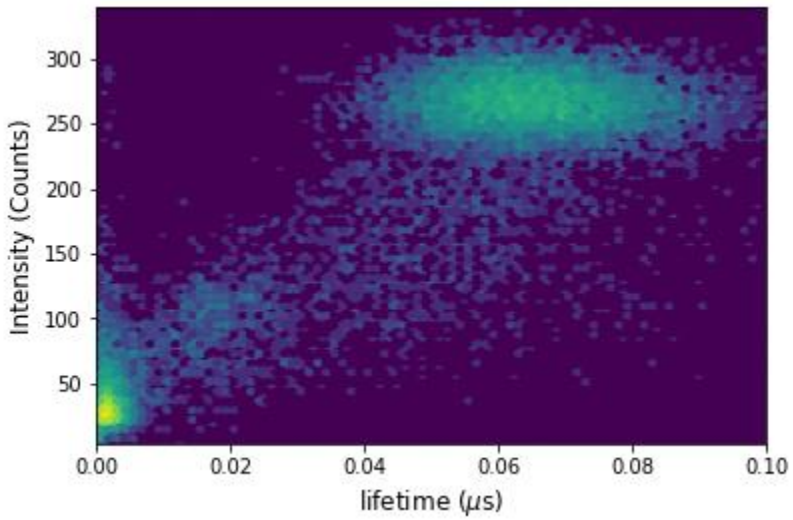

CU012c FLID plot scaled to the same intensity as CU012a/ZnS. Bin width = 10 ms.

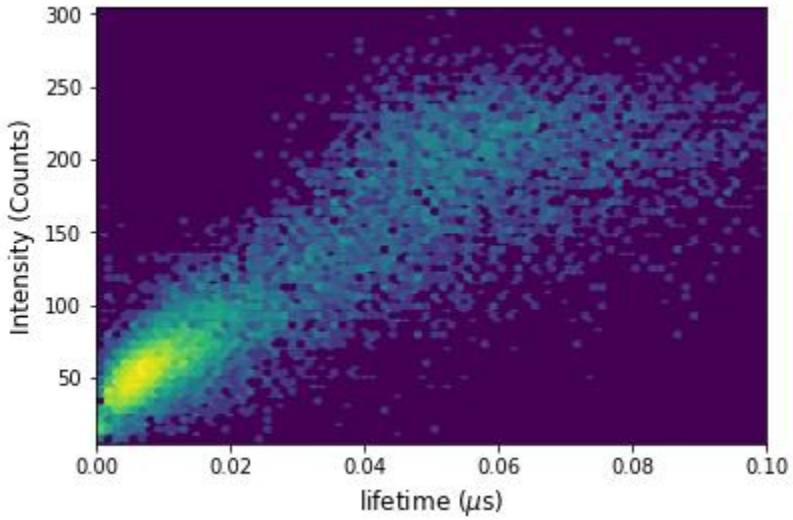

CU012a FLID plot of the same particle/blinking traces produced in the main text. Bin width = 30 ms

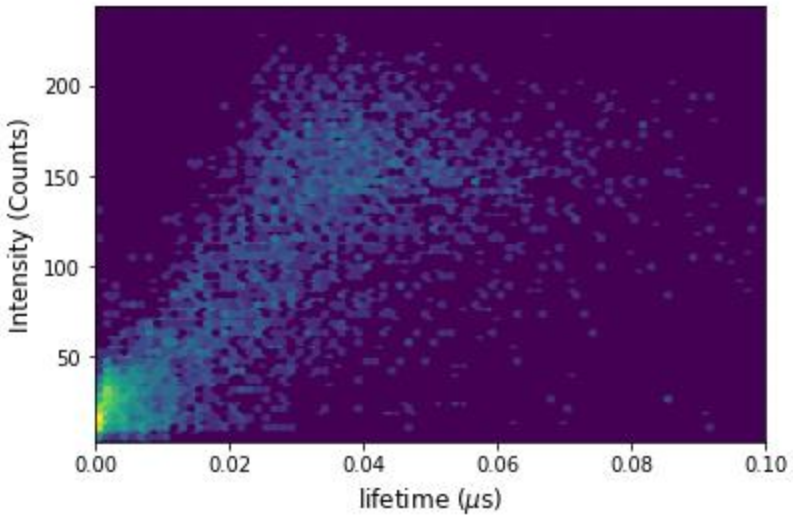

CU012b FLID plot of the same particle/blinking trace produced in the main text. Bin width = 30 ms

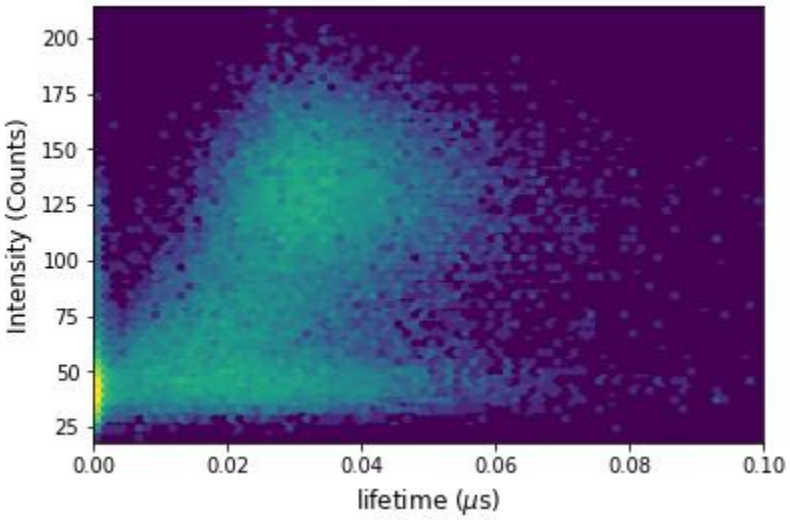

CU012c FLID plot of the same particle/blinking trace produced in the main text. Bin width = 30 ms

Figure 14

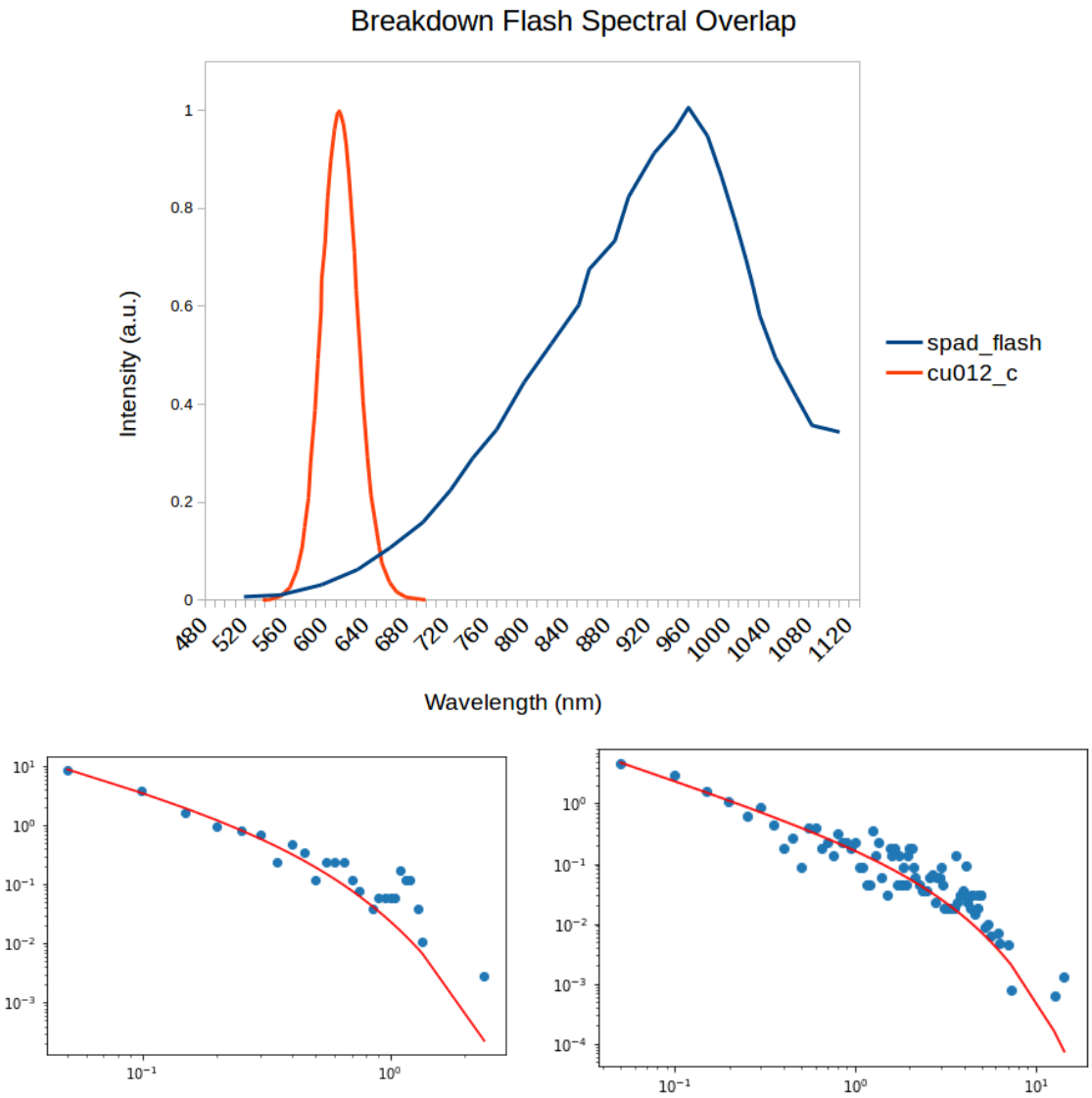

Left: on time probability plot of Figure 14. *Right:* on time probability plot of Figure 15

2.7. Experimental

2.7.1. Materials and Methods

Unless otherwise noted, all chemicals were used as received without further purification.

Ligand stripping

100 μL QD stock solution was stripped of solvent on the rotary evaporator. The QD solid was then dissolved in 500 μL of deuterated benzene (C_6D_6). 100 μL of dimethyl terephthalate standard (50 mM) in C_6D_6 was added as an internal standard. This solution was transferred to an NMR tube. 10 μL of TMEDA solution (of varying concentrations) is added to the NMR tube. After NMR analysis the solution was removed and diluted with 3 mL hexanes for absorbance and Photoluminescence spectroscopy. The diluted solution was then diluted further into 0.5% w/w pmma solution in toluene for TCSPC measurements.

2.7.2. Confocal fluorescence microscopy measurements

Particle deposition

QD solutions were diluted in 0.5% w/w pmma solution in toluene until colorless. Solution was spun coat at 2000 rpm for 1 minute onto #1 circular glass substrates to be loaded into a screwing sample holder for the confocal microscope.

Single particle measurements

Single particle measurements were made on a Picoquant Microtime200 using Symphotime64 software. Samples were excited using a 405nm pulsed laser with tunable rep rate. Fluorescence was collected through the objective, pass a dichroic, and through a 50 μm pinhole

before being split onto two silicon single photon avalanche diodes via a 50/50 beam splitting cube.

Ensemble PL lifetime measurements

Ensemble lifetime measurements were made on dilute solutions of QDs in toluene or hexanes. Samples were loaded into vitricom rectangular glass capillaries (VITROCOM INC HTR1099). capillaries were plugged on both ends using capillary sealant to avoid evaporation of solvent and placed on objective with immersion oil.

Photoluminescence spectroscopy

Photoluminescence quantum yield was obtained on a Horiba Fluoromax-4 with an integrating sphere.

Spherical Quantum Well Synthesis

Spherical quantum well samples were synthesized by colleagues in the Owen lab. For more information please see Hamachi *et al.* and Rrëza *et al.*

CdSe/CdS Core Shell Synthesis

0.22 g of Cadmium oleate was combined with 0.1 g of oleic acid and 11 g of octadecene in a 3 neck round bottom flask. Solution was heated to 240°C under argon and a solution of 12 mg tetramethyl thiourea and 18 mg diphenyl imidazolidine selone in 0.8 g of diglyme was injected. The reaction was finished within 2 hours and was cleaned by slowly adding acetone until the solution appears whispy. This was centrifuged at 7000 rpm for 10 minutes and the solid was redispersed in hexanes, which was then again subjected to methyl acetate and centrifugation

three more times. There was a slight shoulder in the photoluminescence spectra, suggesting a second population.

2.8. References

(1) Ji, B.; Giovanelli, E.; Habert, B.; Spinicelli, P.; Nasilowski, M.; Xu, X.; Lequeux, N.; Hugonin, J.-P.; Marquier, F.; Greffet, J.-J.; et al. Non-Blinking Quantum Dot with a Plasmonic Nanoshell Resonator. *Nature Nanotechnology* **2015**, *10*, 170.

(2) Li, J. J.; Wang, Y. A.; Guo, W.; Keay, J. C.; Mishima, T. D.; Johnson, M. B.; Peng, X. Large-Scale Synthesis of Nearly Monodisperse CdSe/CdS Core/Shell Nanocrystals Using Air-Stable Reagents via Successive Ion Layer Adsorption and Reaction. *Journal of the American Chemical Society* **2003**, *125* (41), 12567–12575. https://doi.org/10.1021/ja0363563.

(3) Liu, Y.; Jiang, C.; Song, C.; Wang, J.; Mu, L.; He, Z.; Zhong, Z.; Cun, Y.; Mai, C.; Wang, J.; et al. Highly Efficient All-Solution Processed Inverted Quantum Dots Based Light Emitting Diodes. *ACS Nano* **2018**, *12* (2), 1564–1570. https://doi.org/10.1021/acsnano.7b08129.

(4) Busby, E.; Anderson, N. C.; Owen, J. S.; Sfeir, M. Y. Effect of Surface Stoichiometry on Blinking and Hole Trapping Dynamics in CdSe Nanocrystals. *J. Phys. Chem. C* **2015**, *119* (49), 27797–27803. https://doi.org/10.1021/acs.jpcc.5b08243.

(5) Chen, Y.; Vela, J.; Htoon, H.; Casson, J. L.; Werder, D. J.; Bussian, D. A.; Klimov, V. I.; Hollingsworth, J. A. "Giant" Multishell CdSe Nanocrystal Quantum Dots with Suppressed Blinking. *Journal of the American Chemical Society* **2008**, *130* (15), 5026–5027. https://doi.org/10.1021/ja711379k.

(6) Kai Zhang, †; Hauyee Chang, †; Aihua Fu, †; A. Paul Alivisatos, †; Haw Yang*, †. Continuous Distribution of Emission States from Single CdSe/ZnS Quantum Dots https://pubs.acs.org/doi/suppl/10.1021/nl060483q (accessed Jun 4, 2018). https://doi.org/10.1021/nl060483q.

(7) Nirmal, M.; Dabbousi, B. O.; Bawendi, M. G.; Macklin, J. J.; Trautman, J. K.; Harris, T. D.; Brus, L. E. Fluorescence Intermittency in Single Cadmium Selenide Nanocrystals. *Nature* **1996**, *383* (6603), 802. https://doi.org/10.1038/383802a0.

(8) Frantsuzov, P.; Kuno, M.; Jankó, B.; Marcus, R. A. Universal Emission Intermittency in Quantum Dots, Nanorods and Nanowires. *Nature Physics* **2008**, *4* (7), 519–522. https://doi.org/10.1038/nphys1001.

(9) Schmidt, R.; Krasselt, C.; Göhler, C.; von Borczyskowski, C. The Fluorescence Intermittency for Quantum Dots Is Not Power-Law Distributed: A Luminescence Intensity Resolved Approach. *ACS Nano* **2014**, *8* (4), 3506–3521. https://doi.org/10.1021/nn406562a.

(10) Galland, C.; Ghosh, Y.; Steinbrück, A.; Sykora, M.; Hollingsworth, J. A.; Klimov, V. I.; Htoon, H. Two Types of Luminescence Blinking Revealed by Spectroelectrochemistry of Single Quantum Dots. *Nature* **2011**, *479* (7372), 203–207. https://doi.org/10.1038/nature10569.

(11) Mulvaney, P.; nicholas. kirkwood@gmail.com; klaus. boldt@uni-konstanz.de; gangchengy@student. unimelb.edu.au; daniel. gomez@rmit.edu.au. Two Mechanisms Determine Quantum Dot Blinking. *figshare* **2017**. https://doi.org/10.26434/chemrxiv.5368474.v1.

(12) Kim, M.-H.; Schubert, M. F.; Dai, Q.; Kim, J. K.; Schubert, E. F.; Piprek, J.; Park, Y. Origin of Efficiency Droop in GaN-Based Light-Emitting Diodes. *Applied Physics Letters* **2007**, *91* (18), 183507. https://doi.org/10.1063/1.2800290.

(13) Zhang, M.; Bhattacharya, P.; Guo, W. InGaN/GaN Self-Organized Quantum Dot Green Light Emitting Diodes with Reduced Efficiency Droop. *Applied Physics Letters* **2010**, *97* (1), 011103. https://doi.org/10.1063/1.3460921.

(14) Iveland, J.; Martinelli, L.; Peretti, J.; Speck, J. S.; Weisbuch, C. Direct Measurement of Auger Electrons Emitted from a Semiconductor Light-Emitting Diode under Electrical Injection: Identification of the Dominant Mechanism for Efficiency Droop. *Physical Review Letters* **2013**, *110* (17). https://doi.org/10.1103/PhysRevLett.110.177406.

(15) Krauss, T. D.; Peterson, J. J. Quantum Dots: A Charge for Blinking. *Nature Materials* **2012**, *11* (1), 14–16. https://doi.org/10.1038/nmat3206.

(16) Crouch, C. H.; Sauter, O.; Wu, X.; Purcell, R.; Querner, C.; Drndic, M.; Pelton, M. Facts and Artifacts in the Blinking Statistics of Semiconductor Nanocrystals. *Nano Lett.* **2010**, *10* (5), 1692–1698. https://doi.org/10.1021/nl100030e.

(17) Ye, M.; Searson, P. C. Blinking in Quantum Dots: The Origin of the Grey State and Power Law Statistics. *Physical Review B* **2011**, *84* (12). https://doi.org/10.1103/PhysRevB.84.125317.

(18) Efros, A. L.; Nesbitt, D. J. Origin and Control of Blinking in Quantum Dots. *Nature Nanotechnology* **2016**, *11* (8), 661–671. https://doi.org/10.1038/nnano.2016.140.

(19) Zhao, J.; Nair, G.; Fisher, B. R.; Bawendi, M. G. Challenge to the Charging Model of Semiconductor-Nanocrystal Fluorescence Intermittency from Off-State Quantum Yields and Multiexciton Blinking. *Phys. Rev. Lett.* **2010**, *104* (15), 157403. https://doi.org/10.1103/PhysRevLett.104.157403.

(20) Kuno, M.; Fromm, D. P.; Hamann, H. F.; Gallagher, A.; Nesbitt, D. J. Nonexponential "Blinking" Kinetics of Single CdSe Quantum Dots: A Universal Power Law Behavior. *J. Chem. Phys.* **2000**, *112* (7), 3117–3120. https://doi.org/10.1063/1.480896.

(21) Wahl, M.; Gregor, I.; Patting, M.; Enderlein, J. Fast Calculation of Fluorescence Correlation Data with Asynchronous Time-Correlated Single-Photon Counting. *Optics Express* **2003**, *11* (26), 3583. https://doi.org/10.1364/OE.11.003583.

(22) Shulenberger, K. E.; Bischof, T. S.; Caram, J. R.; Utzat, H.; Coropceanu, I.; Nienhaus, L.; Bawendi, M. G. Multiexciton Lifetimes Reveal Triexciton Emission Pathway in CdSe Nanocrystals. *Nano Letters* **2018**, *18* (8), 5153–5158. https://doi.org/10.1021/acs.nanolett.8b02080.

(23) Jha, P. P.; Guyot-Sionnest, P. Trion Decay in Colloidal Quantum Dots. *ACS Nano* **2009**, *3* (4), 1011–1015. https://doi.org/10.1021/nn9001177.

(24) Amecke, N.; Heber, A.; Cichos, F. Distortion of Power Law Blinking with Binning and Thresholding. *The Journal of Chemical Physics* **2014**, *140* (11), 114306. https://doi.org/10.1063/1.4868252.

(25) Galland, C.; Ghosh, Y.; Steinbrück, A.; Hollingsworth, J. A.; Htoon, H.; Klimov, V. I. Lifetime Blinking in Nonblinking Nanocrystal Quantum Dots. *Nature Communications* **2012**, *3*, 908. https://doi.org/10.1038/ncomms1916.

(26) Peterson, J. J.; Nesbitt, D. J. Modified Power Law Behavior in Quantum Dot Blinking: A Novel Role for Biexcitons and Auger Ionization. *Nano Lett.* **2009**, *9* (1), 338–345. https://doi.org/10.1021/nl803108p.

(27) Nair, G.; Zhao, J.; Bawendi, M. G. Biexciton Quantum Yield of Single Semiconductor Nanocrystals from Photon Statistics. *Nano Lett.* **2011**, *11* (3), 1136–1140. https://doi.org/10.1021/nl104054t.

(28) Aragón, S. R.; Pecora, R. Fluorescence Correlation Spectroscopy and Brownian Rotational Diffusion. *Biopolymers* **1975**, *14* (1), 119–137. https://doi.org/10.1002/bip.1975.360140110.

(29) Ehrenberg, M.; Rigler, R. Fluorescence Correlation Spectroscopy Applied to Rotational Diffusion of Macromolecules. *Quarterly Reviews of Biophysics* **1976**, *9* (1), 69–81. https://doi.org/10.1017/S003358350000216X.

(30) Briddon, S. J.; Hill, S. J. Pharmacology under the Microscope: The Use of Fluorescence Correlation Spectroscopy to Determine the Properties of Ligand–Receptor Complexes. *Trends in Pharmacological Sciences* **2007**, *28* (12), 637–645. https://doi.org/10.1016/j.tips.2007.09.008.

(31) Hess, S. T.; Huang, S.; Heikal, A. A.; Webb, W. W. Biological and Chemical Applications of Fluorescence Correlation Spectroscopy: A Review. *Biochemistry* **2002**, *41* (3), 697–705. https://doi.org/10.1021/bi0118512.

(32) Laurence, T. A.; Fore, S.; Huser, T. Fast, Flexible Algorithm for Calculating Photon Correlations. *Optics Letters* **2006**, *31* (6), 829. https://doi.org/10.1364/OL.31.000829.

(33) Zwiller, V.; Blom, H.; Jonsson, P.; Panev, N.; Jeppesen, S.; Tsegaye, T.; Goobar, E.; Pistol, M.-E.; Samuelson, L.; Björk, G. Single Quantum Dots Emit Single Photons at a Time: Antibunching Experiments. *Applied Physics Letters* **2001**, *78* (17), 2476–2478. https://doi.org/10.1063/1.1366367.

(34) Klimov, V. I. Spectral and Dynamical Properties of Multiexcitons in Semiconductor Nanocrystals. *Annual Review of Physical Chemistry* **2007**, *58* (1), 635–673. https://doi.org/10.1146/annurev.physchem.58.032806.104537.

(35) Rowland, C. E.; Fedin, I.; Zhang, H.; Gray, S. K.; Govorov, A. O.; Talapin, D. V.; Schaller, R. D. Picosecond Energy Transfer and Multiexciton Transfer Outpaces Auger Recombination in Binary CdSe Nanoplatelet Solids. *Nature Materials* **2015**, *14* (5), 484–489. https://doi.org/10.1038/nmat4231.

(36) Beyler, A. P.; Bischof, T. S.; Cui, J.; Coropceanu, I.; Harris, D. K.; Bawendi, M. G. Sample-Averaged Biexciton Quantum Yield Measured by Solution-Phase Photon Correlation. *Nano Lett.* **2014**, *14* (12), 6792–6798. https://doi.org/10.1021/nl5027953.

(37) Fisher, B.; Caruge, J. M.; Zehnder, D.; Bawendi, M. Room-Temperature Ordered Photon Emission from Multiexciton States in Single CdSe Core-Shell Nanocrystals. *Phys. Rev. Lett.* **2005**, *94* (8), 087403. https://doi.org/10.1103/PhysRevLett.94.087403.

(38) Moreau, E.; Robert, I.; Manin, L.; Thierry-Mieg, V.; Gérard, J. M.; Abram, I. Quantum Cascade of Photons in Semiconductor Quantum Dots. *Phys. Rev. Lett.* **2001**, *87* (18), 183601. https://doi.org/10.1103/PhysRevLett.87.183601.

(39) Mangum, B. D.; Ghosh, Y.; Hollingsworth, J. A.; Htoon, H. Disentangling the Effects of Clustering and Multi-Exciton Emission in Second-Order Photon Correlation Experiments. *Opt. Express, OE* **2013**, *21* (6), 7419–7426. https://doi.org/10.1364/OE.21.007419.

(40) Jeong, B. G.; Park, Y.-S.; Chang, J. H.; Cho, I.; Kim, J. K.; Kim, H.; Char, K.; Cho, J.; Klimov, V. I.; Park, P.; et al. Colloidal Spherical Quantum Wells with Near-Unity Photoluminescence Quantum Yield and Suppressed Blinking. *ACS Nano* **2016**, *10* (10), 9297–9305. https://doi.org/10.1021/acsnano.6b03704.

(41) S. Hamachi, L.; Yang, H.; Plante, I. J.-L.; Saenz, N.; Qian, K.; P. Campos, M.; T. Cleveland, G.; Rreza, I.; Oza, A.; Walravens, W.; et al. Precursor Reaction Kinetics Control Compositional Grading and Size of CdSe 1−x S x Nanocrystal Heterostructures. *Chemical Science* **2019**. https://doi.org/10.1039/C9SC00989B.

(42) Rreza, I.; Owen, J. S. Spherical Quantum Wells for LED Downconversion. *Manuscript in prep*.

(43) Anderson, N. C.; Hendricks, M. P.; Choi, J. J.; Owen, J. S. Ligand Exchange and the Stoichiometry of Metal Chalcogenide Nanocrystals: Spectroscopic Observation of Facile Metal-Carboxylate Displacement and Binding. *Journal of the American Chemical Society* **2013**, *135* (49), 18536–18548. https://doi.org/10.1021/ja4086758.

(44) Yuan, G.; Gómez, D. E.; Kirkwood, N.; Boldt, K.; Mulvaney, P. Two Mechanisms Determine Quantum Dot Blinking. *ACS Nano* **2018**, *12* (4), 3397–3405. https://doi.org/10.1021/acsnano.7b09052.

Chapter 3. Controlling the reactivity of metal nanoparticle surfaces to etch graphite

TABLE OF CONTENTS

3.1. Introduction

Producing functional materials with atomic precision is a long-sought goal of chemists, physicists, and materials scientists.[1–5] Materials most interesting properties, and the relationship to their structure, is often obscured by our lack of understanding of the atomic composition and morphology. Better understanding of structure-function relationships in heterogeneous catalysts, superconductors, solar cells, membranes, and battery anodes will be needed to help address the problems future society will face.

Through catalytic gasification (scheme 1) new edges with atomic straightness over μm lengths have been observed[6–10]. Fine structural control over these length scales is a unique feature that will allow for the tuning of catalyst chemical environment necessary for highly selective reactions. Successful functionalization of graphite edges may produce highly dense active sites, comparable to zeolites or metal-organic frameworks. In addition to understanding the fundamental processes driving the unusual ordering and reactivity of graphite edges, recent work has suggested graphite may be a useful scaffold for attaching molecular catalysts.[11,12] There is strong interest in controlling the structure, especially at nanometer length scales, of graphene for electronic applications,[13–16] but the creation of a new, potentially reactive macromolecule scaffold to do chemistry, catalysis, and functionalization is an exciting source of inspiration for this project.

3.1.1. Understanding the mechanism of etching

The gasification of carbon through metal catalysis is a simple chemical process,[6,17,18] despite the striking and unusual "Pacman" like particle propagation that produces trenches and pits on the surface of graphite.[9,10,19–22] The simplest way to understand the driving force for this is the simple reaction in Scheme 1, catalyzed by a metal nanoparticle. This reaction has been known for nearly 50 years, and the etching of graphite by metal catalysts is nearly as old.[6,7]

Scheme 1: Carbon methanation

1) $\mathbf{2H_{2\,(g)} + C_{(s)} \rightleftharpoons CH_{4\,(g)}}$

While the chemical reaction is easy to write, the behavior of metal catalysts on a substrate at high temperatures is more complex. In the case of graphitic etching, the carbon at step edges of defects are dissolved into the metal nanoparticle. Dissolved carbon then moves through the metal particle to the surface, where it reacts with adsorbed hydrogen atoms, catalytically forming methane gas which evolves off the particle.[23–25]

Figure 1

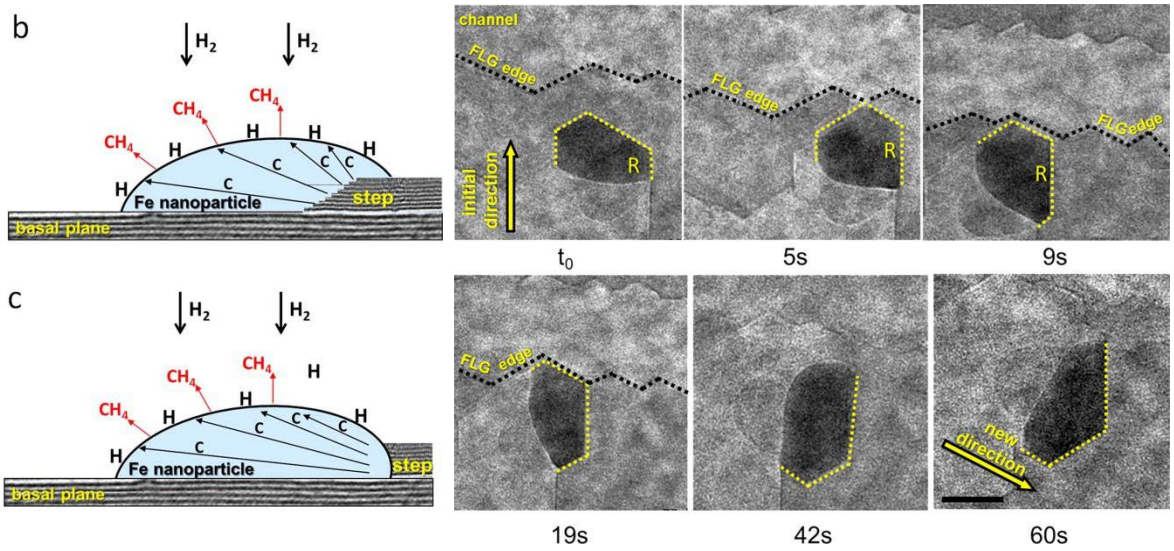

Left: cartoon of catalytic etching mechanism. *Right:* TEM micrographs of iron nanoparticle changing direction upon reaching graphene edge. Adapted with permission from Melinte, *et al* ACS Catalysis **2017**, 5941–5949. Copyright 2017 American Chemical Society.

This reaction provides the thermodynamic driving force for the motion of the particles, as they eject methane, they move forward with the crystal structure of the graphite, dissolving more "fuel" for methanation.

Three important features of this mechanism hint at methods of controlling the etching behavior. First, the dissolution of carbon occurs at step edges, not on pristine graphite. The edges of graphite are much more reactive than the basal plane, thus the *initiation* of etching can be manipulated by controlling the density, location, and geometry of defects and step edges. Second, the propagation of the metal particle relies on available carbon. The micrograph in Figure 1 clearly shows that when the iron nanoparticle approaches the edge of the few-layer graphene, it changes direction, following the carbon edges that fuel its catalytic activity. Again, by controlling the locations of available carbon the propagation of trench development should, in theory, be influenced. Third, the metal geometry adheres to the crystal structure of the graphite, matching the faceting of the hexagonal carbon edges. This will guide some later experiments to

enable more control over trench initiation. Since the propagation of metal nanoparticles is templated by the underlying graphite crystal structure, atomically precise edges can be formed, sometimes continuing over micrometer lengths, creating structures with an unusual degree of order over those length scales.

3.1.2. Experimental design

Samples of highly ordered pyrolytic graphite (HOPG) or flakes exfoliated from HOPG using scotch tape deposited onto silicon chips, were subjected to O_2 plasma treatment to clean the surface of ambient organics and improve wetting of metal salt solutions. Aqueous solutions of the desired metal were then spun coat onto the graphite containing substrate. Samples were loaded into a tube furnace reactor that used mass flow controllers to regulate the flow of inert (Ar or N_2) and reactive gases (usually H_2, sometimes O_2 or NH_3). The exhaust flow from the tube furnace was directed into a nearby fume hood. Samples were heated under gas flow to 500°C for 20 minutes to ensure a reductive atmosphere, remove any surface oxygen species, and begin metal nanoparticle formation. The temperature was then raised to 1000°C for the remainder of the reaction, following the procedure developed by Campos *et al.* [10] . After cooling, samples analyzed by AFM or SEM showed metal nanoparticles and trenches cut into the graphite.

Figure 2

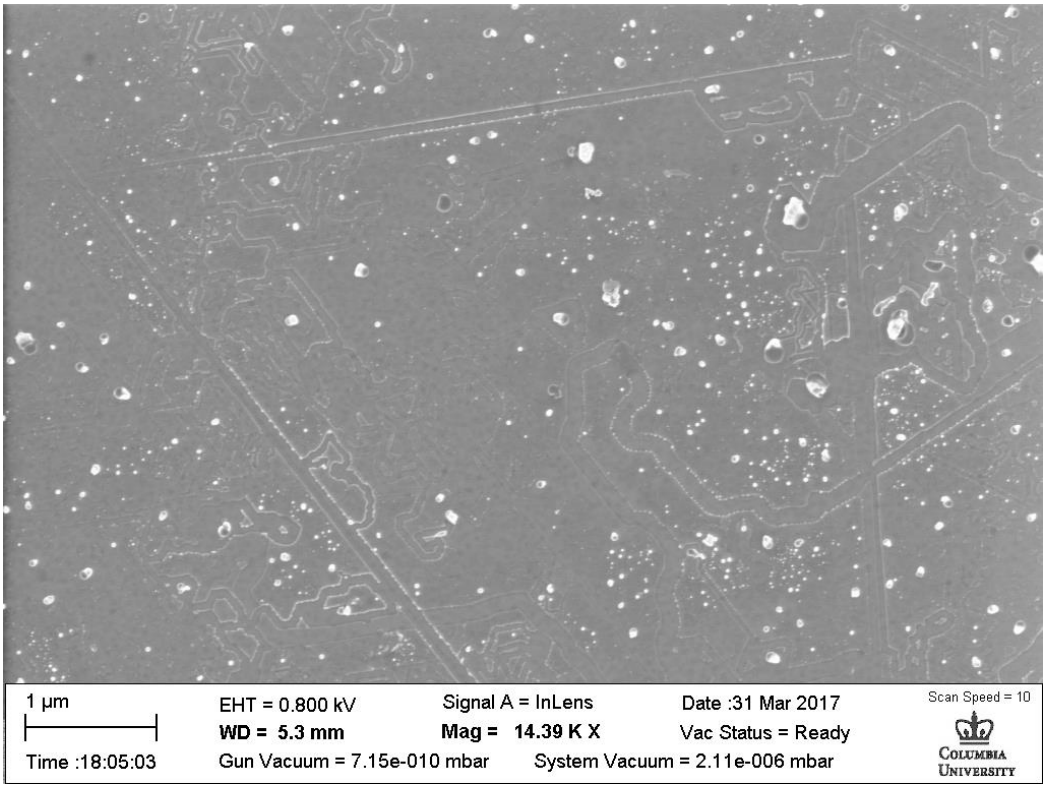

SEM micrograph of Cobalt etched HOPG with channels greater than 1 µm in length

3.2. Controlling etching through particle synthesis

3.2.1. Metal Dependence of etching

Seven different metal salt solutions (10 mM) were deposited via spin coating onto silicon chips with graphite flakes exfoliated from HOPG. The results of the metal etching survey are given in Table 1. The mechanism of etching graphite and conversion is, essentially, the reverse of carbon nanotube or graphite synthesis. As such, some metals, most notably platinum, produced carbon nanotubes upon heating to 1000°C under H_2 gas flow. Presumably the carbon from the graphite was dissolved into the metal (or perhaps methane produced from direct gasification acted as the carbon feedstock) and, instead of being released methane, reformed into nanotubes. Ruthenium, nickel, palladium and copper also show some forms of redeposition of

carbonic materials, although they are less clearly carbon nanotubes as the platinum sample. From these results cobalt, iron, and nickel appeared to be the most promising for clean, controllable etching experiments.

Table 1

Metal Salt dissolved in H_2O	**Result**
$CoCl_2 \cdot 2H_2O$	Small nanoparticles, etching occurs
$CuCl_2 \cdot 2H_2O$	Small nanoparticles, etching occurs, debris/nanotubes possible
$FeCl_3 \cdot 6H_2O$	Large nanoparticles, etching occurs
$NaPtCl_4 \cdot xH_2O$	No etching, carbon nanotube formation
$NiCl_2 \cdot 2H_2O$	Small nanoparticles, etching occurs, possibly some nanotubes
$PdCl_2 \cdot 2ACN$ (solution in ACN)	Large nanoparticles, etching occurs, nanotube formation
$RuCl_3$	Small particles, limited etching, possibly some nanotubes
$Zn(CH_3CO_2)_2 \cdot 2H_2O$	No effect

Especially clear from the AFM micrographs are the appearance of two distinct types of trenches etched by the metal nanoparticles. Very large metal particles obviously cut larger trenches, but they also appear to meander more, better able to avoid the limitations of the graphite crystal structure, while smaller particles often move in nearly atomically precise straight lines, only changing direction at 30° or 60° angles templated by the carbon structure.[10,19] This may be due to energy differences in the dissolution and reaction of carbon atoms, or simply due to the larger size of the particles. Clearly the metal identity plays a complicated role in determining the behavior of etched graphite. Aside from thermodynamic differences (e.g. energy associated with metal carbide formation and stability) the size of metal particles formed is dependent on the identity of the metal. Metals with too high melting point may not be as mobile, or may not be able to deform to the graphite crystal structure as easily.

Figure 3

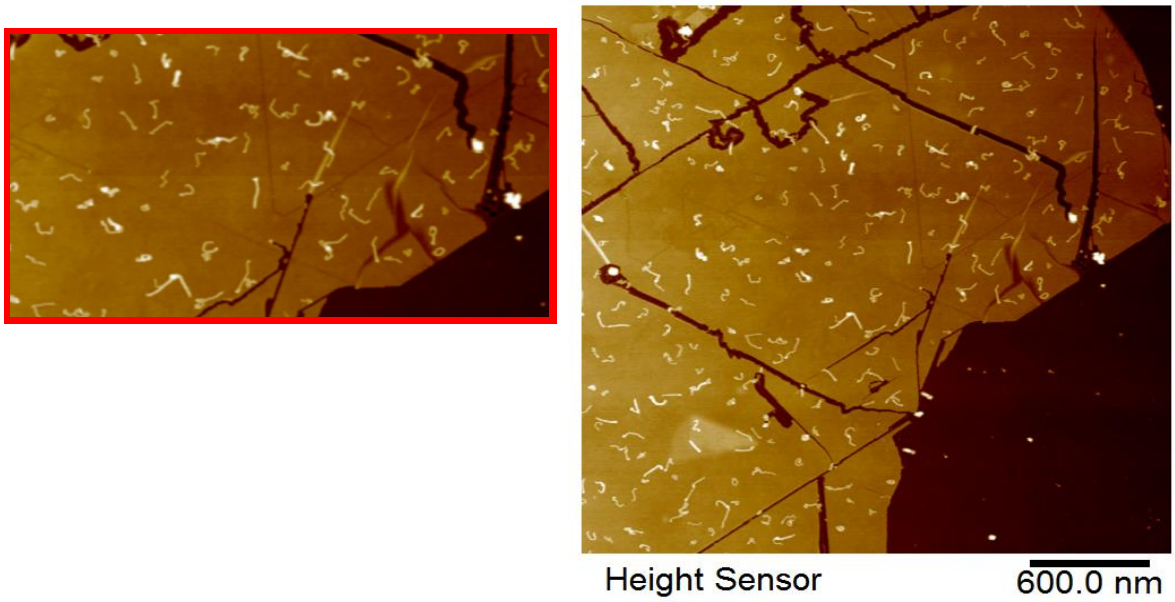

AFM micrograph of cobalt etched trenches on exfoliated graphite flake. *Left:* zoom in of highlighted area to highlight the smaller, straight channels.

3.2.2. Ex-situ nanocrystal synthesis - making monodisperse Cobalt Nanoparticles

Because the mechanism of graphite etching involves the propagation of metal nanoparticle catalysts, the width of the trench is necessarily determined by the size of the nanoparticle. While in original literature reports nanocrystals are formed in-situ from deposited metal salts that agglomerate at elevated temperatures, colloidal synthesis should yield more control over the size of the catalyst particles.

Figure 4

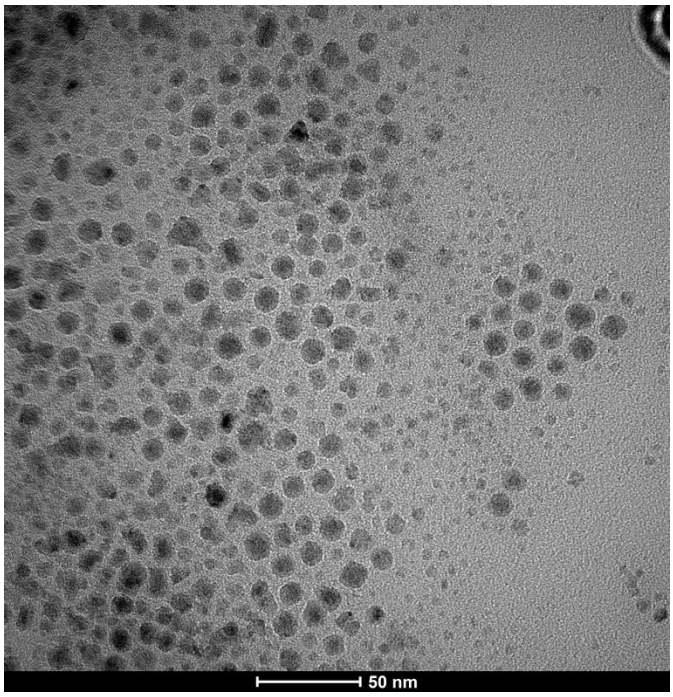

TEM micrograph of polydisperse Co nanoparticles synthesized with additional ODPA but without a solvent annealing after the reaction time

Particles were synthesized from a modified version of the procedure Yin et al.[26] Developed as the first part of their synthesis of hollow CoS nanocrystals. A solution of dicobalt octacarbonyl and oleic acid in o-dichlorobenzene was injected into a flask under argon with trioctylphosphene oxide solvent at reflux (182°C). The reaction mixture was cooled after 15-60 sec. The initial reaction, as run from the literature source, failed to produce colloidally soluble

particles. Octadecyl phosphonic acid (ODPA) was spiked into the TOPO solvent, believing that the literature source used TOPO that contained impurities, while the recrystallized TOPO used in this experiment did not. Addition of ODPA resulted in a dark colloidal solution and a pink supernatant (likely residual cobalt ions). TEM micrographs of the solution mixture reveal highly polydisperse nanocrystals. In order to obtain more monodisperse samples the reaction was allowed to run at reflux for at least 10 minutes.[26,27] The mechanism of this apparent size focusing is not known, and not well described in the literature prep. An updated recommended preparation for cobalt nanocrystal synthesis is in the Experimental section.

Figure 5

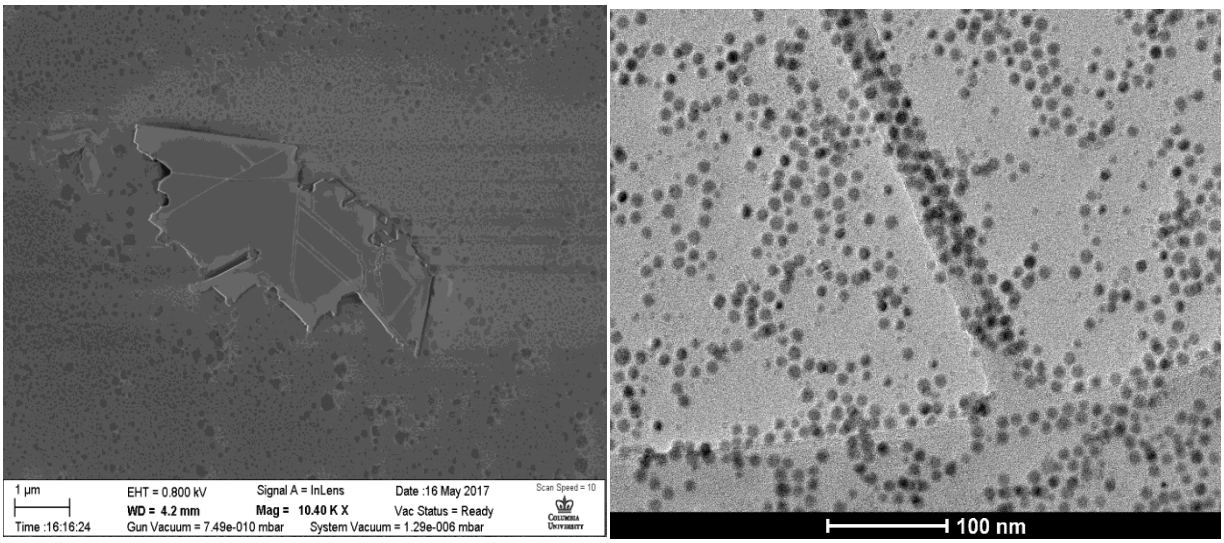

Left: SEM Micrograph of graphite flake etched with colloidally synthesized nanoparticles. *Right:* TEM micrograph of colloidally synthesized nanoparticles.

3.2.3. Etching with colloidal Cobalt nanocrystals

Cobalt metal nanoparticle solutions synthesized by this method were used as etching catalysts. The size control is limited somewhat by the agglomeration of particles at reaction temperatures, but promising SEM micrographs shown in Figure 5 demonstrate this as a tool for

controlling the size and morphology of the graphite edge structures and trenches. The trenches in figure 5 vary in size between 30-40 nm for the narrow trenches, and 70-90nm for the widest trenches, while the colloidally synthesized particles were less than 15 nm in diameter by TEM sizing. Perhaps the greatest benefit of using the colloidal solutions as metal catalysts was in limiting the concentration of metal available to form particles. If lower temperature reaction conditions are able to yield catalytic gasification, colloidal nanoparticle engineering may be more useful.

3.3. Defect patterning to control etching

3.3.1. Patterning holes to control etching initiation

Because the basal plane atoms in graphite are very stable, transition metal catalyst particles begin gasifying graphite carbons at more reactive defect sites and edges. By controlling the defect density and morphology, control over the shape of the trenches should be possible. Patterning of defects may allow for controlled production of arrays, superlattices, and other structures of etched graphene shapes. For example, by patterning holes in the carbon we can deprive the catalyst particle of the carbon atoms that "fuel" the gasification reaction. Patterning defects through standard lithographic techniques has proven to be an effective method of inducing catalyst initiation, as seen in the AFM micrographs seen in Figure 6.

While there are clearly trenches that began at the edge of the patterned hole, there are also areas that initiate and propagate trench formation outside of patterned locations. Large areas of graphite are likely to contain many defects, so starting with pristine graphene and avoiding damage to other areas during lithographic patterning will help avoid excess etching. Reducing the availability of metal catalyst could also help contain the gasification initiation to patterned

areas. Due to the hexagonal crystal structure of the graphite, the trenches emanate from the patterned hole at specific increments of 60° angles, and appear to form faceted regions at the interface of the hole and the substrate.

Figure 6

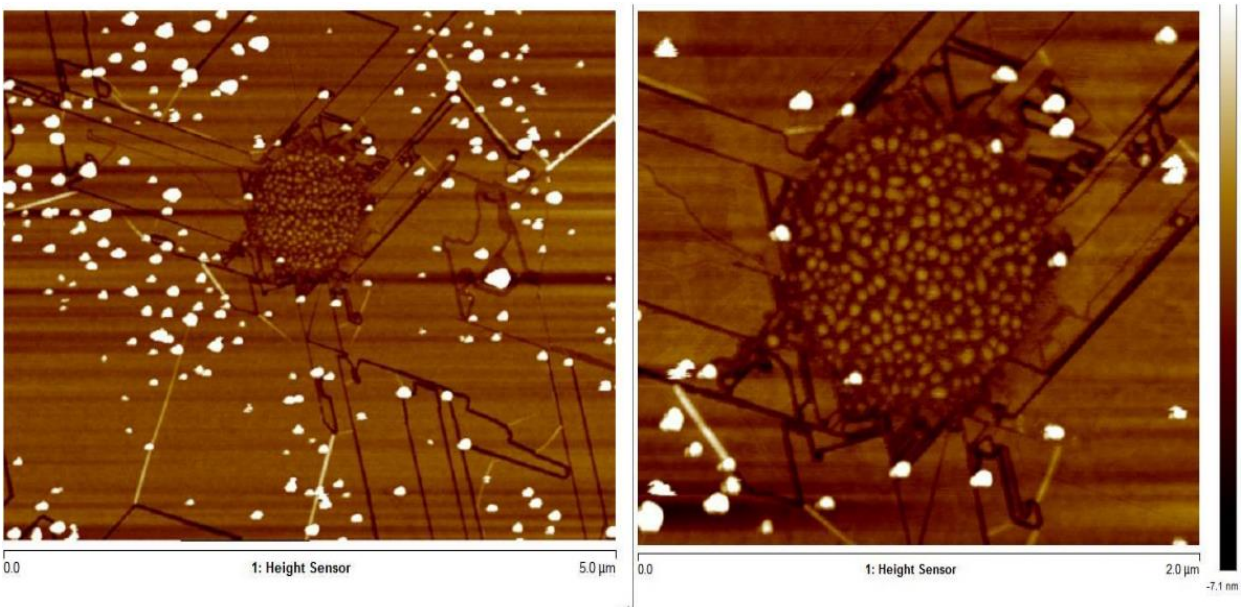

AFM Micrograph of a lithographically patterned hole with metal particle etched trenches emanating outward.

3.3.2. Deposition of metal catalyst into patterned holes

While the patterning of holes created controlled defect sites where metal nanoparticles could easily initiate trench etching, spin coating removes this control knob by depositing metal into various other defects present in the sample. To avoid unwanted trench formation, collaborators in the Dean lab patterned holes in graphene and subsequently deposited cobalt metal through evaporation onto the same mask they used for the lithographic patterning. This was supposed to ensure that *only* the patterned holes would have metal catalysts present to etch.

This sample was then reacted at 1000°C under H_2 flow as previously described. Before and after AFM micrographs are shown in Figure 7.

Figure 7

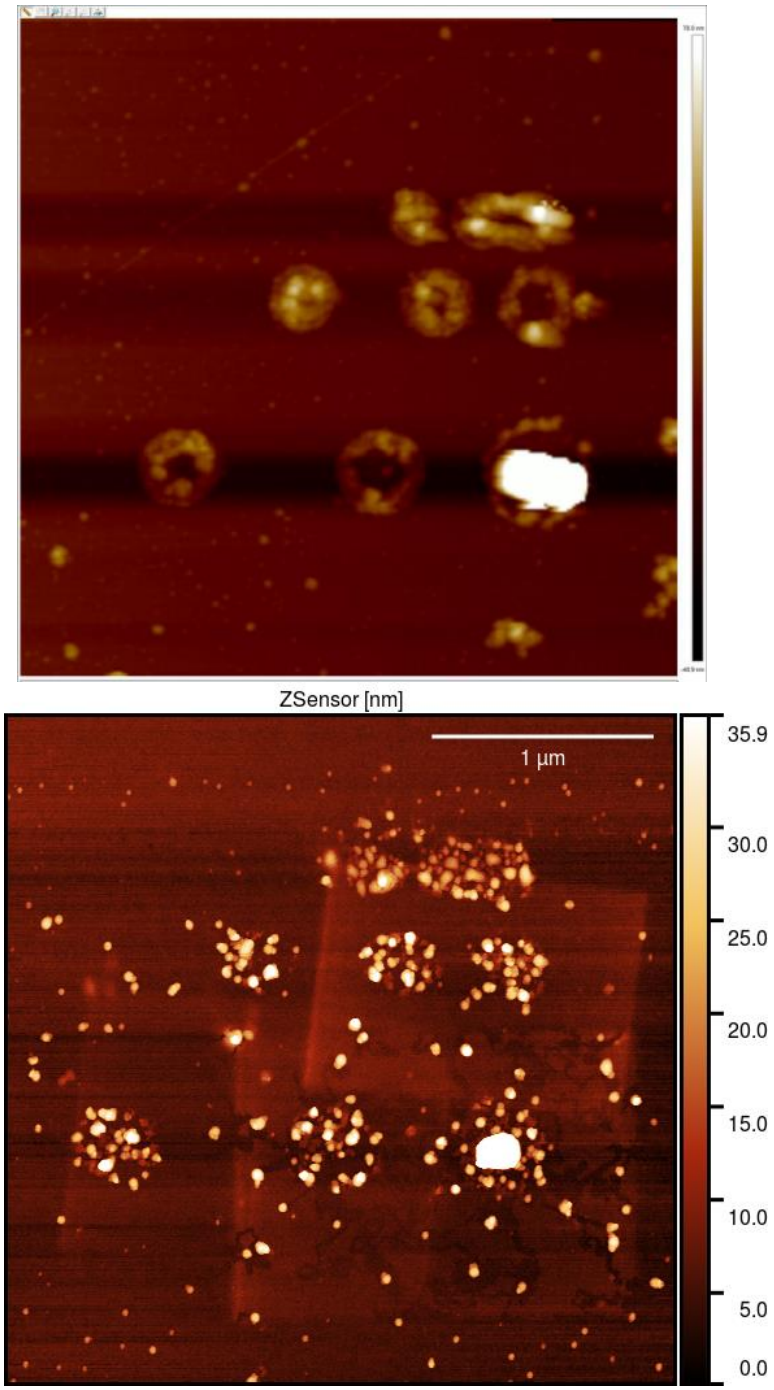

AFM micrographs of lithographically patterned holes used in etching experiments. *Top:* before high temperature hydrogen exposure *Bottom:* after etching

Analysis of this sample showed some metal nanoparticle and corresponding trench formation away from the deposited holes; however, it is clear that metal etching did occur from the metal deposited, with large particles and gasified areas moving outward from the patterned areas. Producing patterned areas with less metal would likely lead to smaller particles, and more controlled etching, however, true size control of the particles is still difficult at these elevated temperatures. The results of this etching using patterned defects and targeted metal deposition are very promising.

3.3.3. Faceting of defects to control etching propagation

Literature studies[2] and our own patterning results suggest that the metal nanoparticle must form a faceted edge aligned with the crystal structure of the graphite when it produces trenches. This suggests that pre-faceted holes may add additional control over direction and location of trench initiation. Defects oxidized at moderate temperatures can produce hexagonal holes by reacting more rapidly with armchair carbon atoms.[3,4] HOPG substrates were exfoliated with scotch tape to produce a pristine surface.

Figure 8

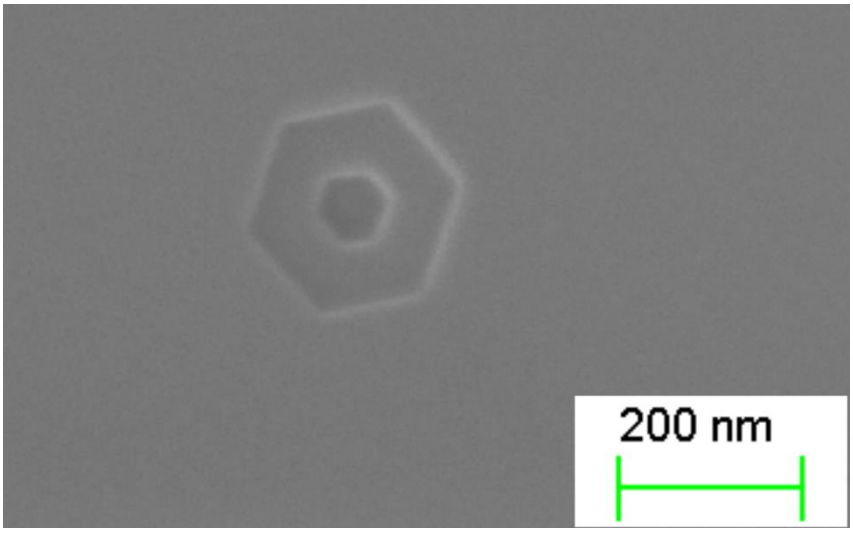

SEM micrograph of hexagonal hole derived from oxidation of a defect upon heating with O_2 gas

Samples were then heated to 500ºC, then 700ºC, in the presence of O_2 gas. Any existing defects in the basal plane of the HOPG were then extended into hexagon shapes, ranging in size from tens of nm to a few micrometers. These faceted defects were then used for trench initiation.

3.3.4. Etching from faceted edges of hexagonal pits

As seen in Figure 9, the metal particles in these faceted holes initiate their trenches at faceted edges and the vertices of the hexagons. Additional micrographs of hexagonal holes producing trenches from the faceted vertices can be found in the Additional Figures section.

Figure 9

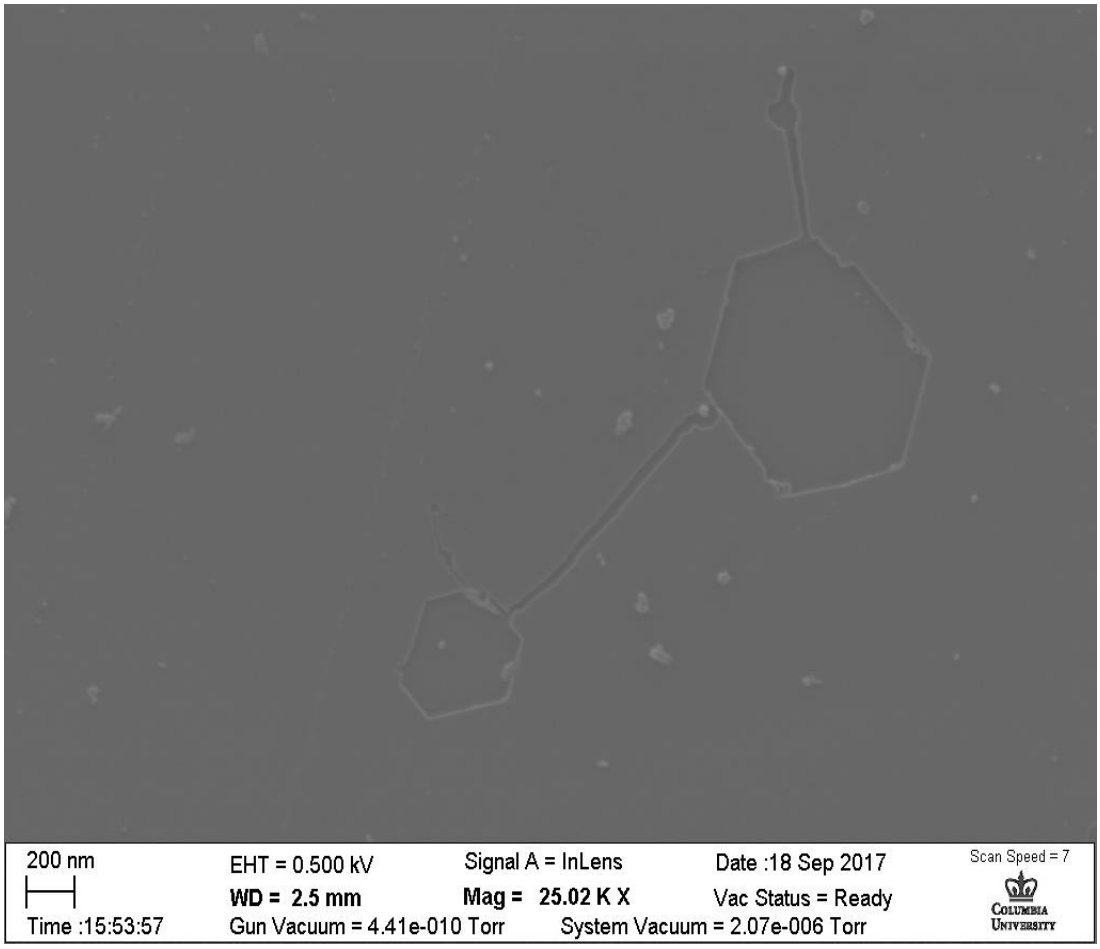

SEM Micrograph of faceted holes etched in O_2 followed by catalytic gasification. Metal particle cut trenches initiate at faceted regions of hexagons.

As we have seen in Figure 9, metal particles form a faceted edge with the graphite structure. Since the motion of the particles propagates via an attractive force or "wetting" between the graphite and metal, providing an already faceted step edge eases the initiation of trench formation. The micrographs in Figure 9 and Addition Figures show very large particles, which can meander throughout the graphite structure after the initiation at the faceted edge, however, smaller particles would be more likely to form straight trenches.

3.4. In-situ functionalization via reactive gases

3.4.1. *Etching with Ammonia Gas*

Figure 10

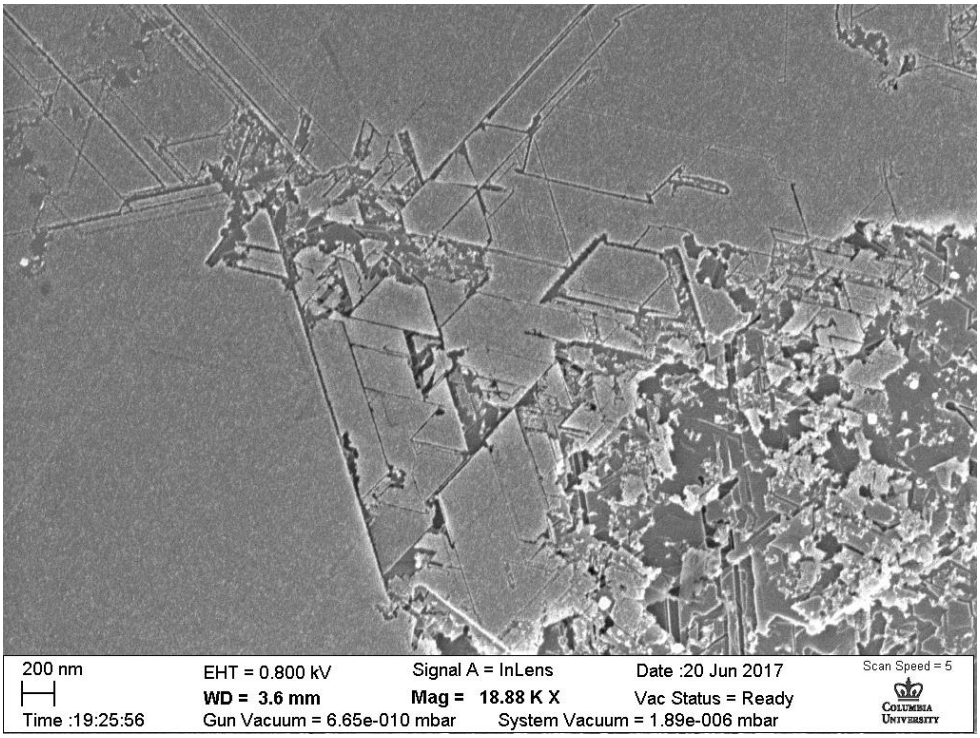

SEM micrograph of HOPG etched with Co in the presence of NH_3 note the trenches on the left and the pitting on the lower right

To introduce more control to functionalizing the edges of graphite, H_2 gas was replaced with NH_3 for the gasification reactions. We hypothesized this could produce etched trenches with Nitrogen functionality instead of the (presumed) hydrogen terminations. Experiments involving Ammonia resulted in two forms of gasification, uncontrolled pitting (likely the result of direct reaction of NH_3 with the carbon) and trench formation (possibly from catalytic nitrogenation, but more likely the result of H_2 produced by NH_3 cracking, scheme 2).

Scheme 2: Ammonia Cracking and carbon gasification

2) $\mathbf{2\ NH_3 \rightleftharpoons 3\ H_2 + N_2}$

3) $\mathbf{NH_3 + C \rightleftharpoons H_2 + HCN}$

3.4.2. XPS

XPS spectra of NH_3 reacted HOPG shows clear N signal, which must come from N atoms incorporated into the structure, as adsorbed ammonia is unlikely given the vacuum of the XPS and the volatility of NH_3 molecules. Although XPS analysis suggested nitrogen incorporation on the graphite surface, a large oxygen signal was also present, casting doubt on the *direct* nitrogenation of the graphite. Nitrogenation of graphite oxide using NH_3 is known[28,29] and researchers who have reported direct nitrogenation have later discovered evidence of necessary oxidation (through a leak in their reactor) before the nitrogenation occurs.

While the tube furnace reactor used in this study was inspected and found not to be leaking prior to these experiments (due to the dangers of gas exposure, especially at high temperature, and the fear of death of the author), the sample preparation did involve exposure to oxygen plasma, to clean the substrate, improve metal salt solution wetting, and to etch the topmost layers of HOPG. It is likely that oxygen moieties were installed during the plasma treatment. Control experiments run without O_2 plasma treatment prior to NH_3 reactions showed no incorporation of N, and nearly no oxygen presence.

Figure 11

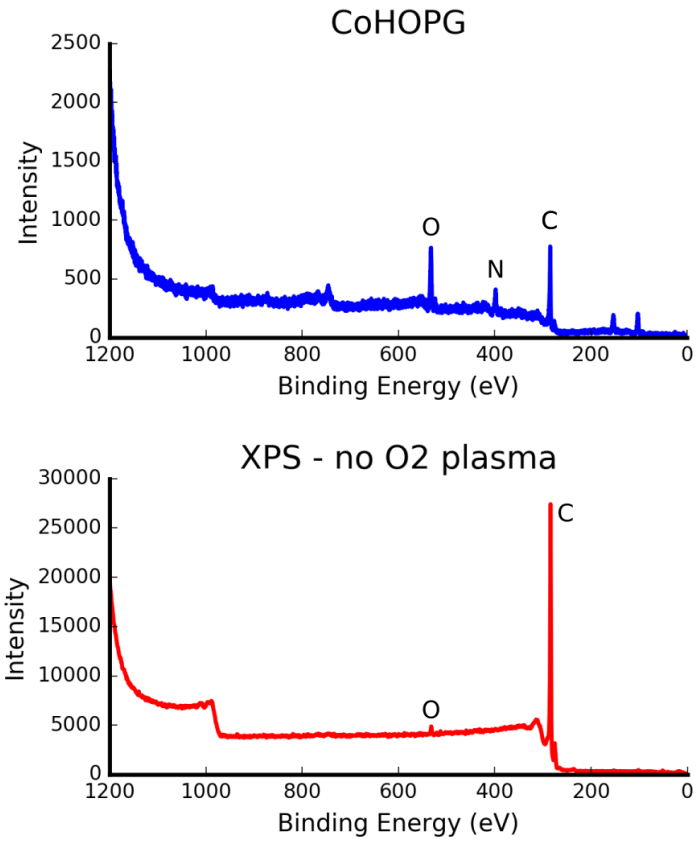

XPS spectra of HOPG etched with Co in the presence of NH_3 gas. *Top:* sample preparation included O_2 plasma treatment and contains strong Oxygen and Nitrogen 1s signals. *Bottom*: sample preparation avoided O_2 plasma and shows no N incorporation

3.4.3. STM Measurements

Collaborators in the Pasupathy lab at Columbia University performed STM measurements on the etched substrates to help better understand the surface structure and functionalization. Figure 12 shows the micrographs of HOPG etched under hydrogenating conditions. The crystal structure near the trench edges clearly confirms that the catalytic gasification proceeds according to the underlying crystal structure of the substrate, maintaining so called “armchair” and “zigzag” edges.

Figure 12

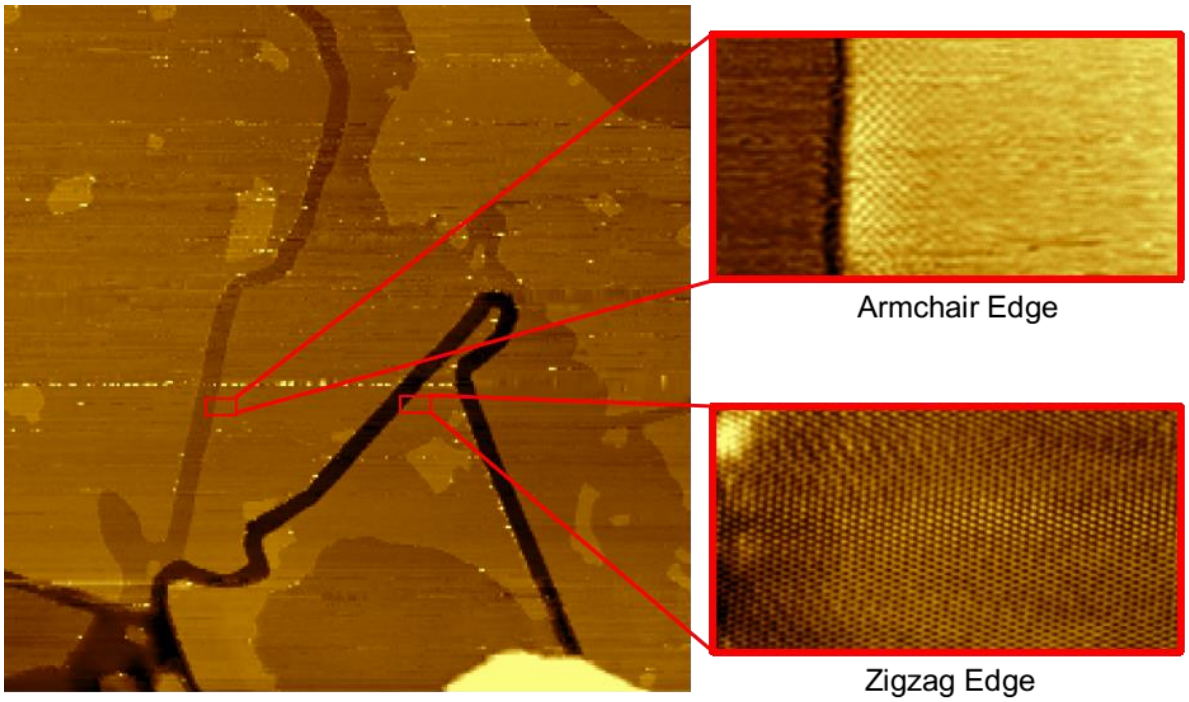

STM measurements of HOPG etched with Co in the presence of H_2 gas. *Right:* zoom ins of crystal structure near the edges of etched trenches confirming the atomic structure is preserved

STM analysis of the substrate with nitrogen XPS signal and saw regions of increased electron density shown in Figure 13, indicating possible nitrogen incorporation. These bright spots, however, were not seen on the straight edges of the etched trenches, and may have incorporated at other defects containing oxygen. While it's possible these bright areas are due to a different atom (, the structure and bonding configurations (as seen in the models in Figure 13) seem much closer to what we'd expect from nitrogen inclusion then, say, oxygen incorporation. Additionally, other reports of nitrogenation of graphite oxide suggest that the nitrogenation occurs by *replacing* oxygen sites.

Figure 13

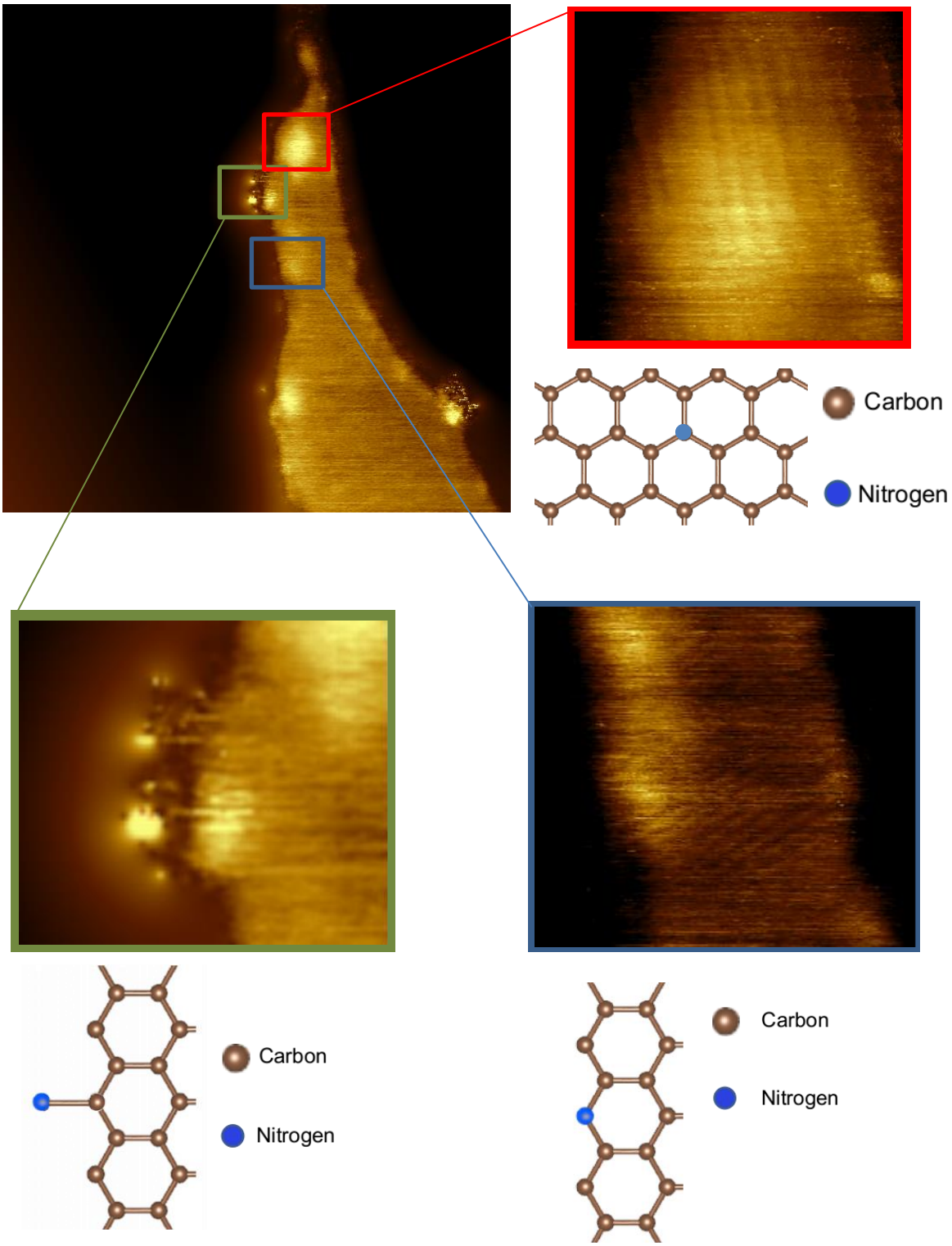

50 nm wide STM micrograph of NH_3 etched HOPG recorded at 150pA, 2V. Bright spots are believed to be Nitrogen atoms incorporated into the graphite at oxygen containing defects. Models with possible bond configuration are shown below zoomed insets.

3.5. Outlook and Conclusions

Catalytic etching of graphitic structures is an exciting avenue to exploring and controlling the microstructure of materials. The already attractive properties of graphitic nanostructures will be greatly enhanced by atomistic knowledge and precise manipulations. The results contained in this work, and in the literature, are promising steps towards fine engineering and understanding of carbon materials, however, limitations remain. The chaotic environments of the reaction in all reported schemes leave doubt about how much control can really be gained. All of the steps towards designing certain features have been curtailed by the intrinsic entropy of defect states, the high mobility of the metal particles, and unselective reactions of heated gas molecules. Some of these may potentially be avoided, e.g. excess defects, or mitigated. The mobility of the metal. The most promising direction, in the authors opinion, is patterned holes in the graphite, faceted by O_2 gasification, then targeted metal deposition before catalytic hydrogenation etching. Logistically this sequence is quite complex, and perhaps should be preceded by greater fundamental understanding of the reaction. Another more manageable direction may be using the etching to enhance the surface area of the graphite, then appending molecular catalysts to newly created edge step sites, instead of relying on naturally occurring locations. This should increase potential catalyst loading without needing atomic control over the morphology of the edges, though that would be useful in this application as well.

3.6. Additional Figures

Figure 14

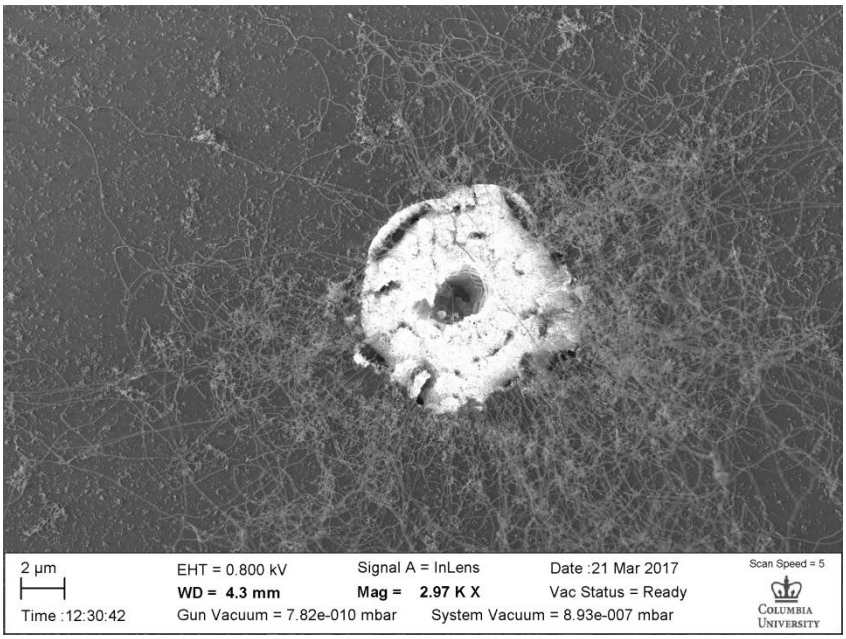

SEM micrograph of carbon nanotubes growing out of a large segment of platinum metal.

Figure 15

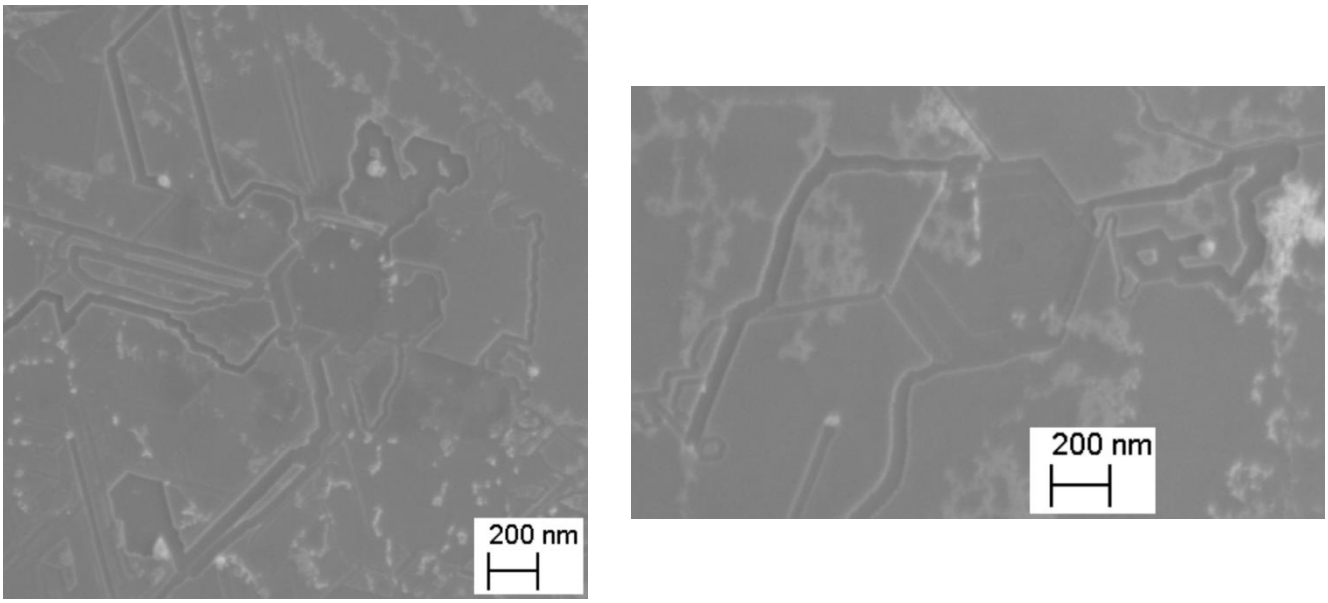

SEM Micrographs of faceted holes etched by O_2 followed by catalytic gasification on exfoliated graphite. Metal particle cut trenches initiate at faceted regions of hexagons

3.7. Experimental

3.7.1. Materials and Methods

Unless otherwise noted, all chemicals were used as received without further purification. 10x10x1 mm HOPG from Alfa-Aesar and Structure probe inc. Were both used after exfoliation of surface layers. Exfoliation onto silicon chips was also performed from these samples using scotch tape. $Co_2(CO)_8$ anhydrous was purchased from Sigma, degassed for 15 minutes, and stored in a N_2 glovebox. Octadecyl phosphonic acid (ODPA), trioctylphosphine oxide (TOPO) were recrystallized by colleagues. o-dichlorobenzene and oleic acid were dried with alumina overnight under Ar then loaded into glovebox and stored in a glovebox with 3Å sieves. Ethanol (EtOH), $CoCl_2•2H_2O$, $CuCl_2•2H_2O$, $FeCl_3•6H_2O$, $NaPtCl_4•xH_2O$, $NiCl_2•2H_2O$, $PdCl_2•2ACN$, $RuCl_3$, $Zn(CH_3CO_2)_2•2H_2O$ were all purchased from Sigma or Strem and used without further purification.

X-ray photoelectron spectroscopy measurements

XPS spectra were recorded using a PHI 5500 using a Mg anode and 1253.6 eV photon energy.

Scanning Tunneling Microscopy measurements

STM measurements were made by collaborators Drew Edelberg and Minghao Cheng in the Pasupathay lab. Measurements of H_2 etched HOPG were made at -100pA and -.5V. Measurements of N incorporated HOPG were made at 150pA and 2V

Transmission Electron microscopy

Micrographs of cobalt nanoparticles were recorded on FEI TALOS F200X Transmission/ Scanning Electron Microscope operating at 200 kV. Samples were deposited on holey carbon on Cu TEM grids

Atomic Force Microscopy

Micrographs were recorded on a Bruker Dimension FastScan AFM. All measurements were made using software defaults

3.7.2. Tube Furnace Reactions

H_2 gas etching

Samples of exfoliated graphite or HOPG with metal solutions deposited were loaded into a tube furnace and sealed. 15% H_2 flow in Argon (150:850 sccm H_2:Ar) purged the system before heating to 500°C. The reactor remained at 500°C for 20 minutes before being heated to 1000°C over 10 minutes. Samples remained at 1000°C for 25 minutes before gas flow ceased and the furnace was cooled.

NH_3 gas etching

Samples of exfoliated graphite or HOPG with metal solutions deposited were loaded into a tube furnace and sealed. 10% NH_3 flow in Argon (100:900 sccm NH_3:Ar) purged the system before heating to 500°C. The reactor remained at 500°C for 20 minutes before being heated to 1000°C over 10 minutes. Samples remained at 1000°C for 25 minutes before gas flow ceased and the furnace was cooled.

O_2 gas etching

Samples of exfoliated graphite or HOPG with metal solutions deposited were loaded into a tube furnace and sealed. 35% O_2 flow in Argon (350:750 sccm O_2:Ar) purged the system before heating to 500°C over 10 minutes. The reactor remained at 500°C for 10 minutes before

O_2 gas flow was stopped and the sample was heated to 700°C over 5 minutes. Samples remained at 700°C for 2 hours in pure Argon flow before gas flow ceased and the furnace was cooled.

3.7.3. Cobalt nanoparticle synthesis

0.1 g recrystallized TOPO and 13 mg recrystallized ODPA (0.05 mmol) was degassed for 20 minutes under Ar at 60°C in a 3 neck round bottom flask with condenser. 15 mL o-dichlorobenzene, and 0.1 mL oleic acid (18mmol) prepared in the glovebox, was added to the flask. The reaction mixture was then heated to reflux (b.p. o-dichlorobenzene ~ 182°C). 0.54 g $Co_2(CO)_8$ (9 mmol) was dissolved in 3 mL o-dichlorobenzene in a glovebox and injected rapidly into the reaction mixture. The reaction was kept at this temperature for at least 10 minutes (recommended 600-1800 seconds) before cooling and combined with an equal volume of EtOH and centrifuged at 7000 rpm for 10 minutes. The resulting supernatant was pink in color. The remaining slid was well dispersed in hexanes.

3.8. References

(1) Beecher, A. N.; Yang, X.; Palmer, J. H.; LaGrassa, A. L.; Juhas, P.; Billinge, S. J. L.; Owen, J. S. Atomic Structures and Gram Scale Synthesis of Three Tetrahedral Quantum Dots. *Journal of the American Chemical Society* **2014**, *136* (30), 10645–10653. https://doi.org/10.1021/ja503590h.

(2) Bieri, M.; Treier, M.; Cai, J.; Aït-Mansour, K.; Ruffieux, P.; Gröning, O.; Gröning, P.; Kastler, M.; Rieger, R.; Feng, X.; et al. Porous Graphenes : Two-Dimensional Polymer Synthesis with Atomic Precision. *Chemical Communications* **2009**, *0* (45), 6919–6921. https://doi.org/10.1039/B915190G.

(3) Qian, H.; Zhu, M.; Wu, Z.; Jin, R. Quantum Sized Gold Nanoclusters with Atomic Precision. *Acc. Chem. Res.* **2012**, *45* (9), 1470–1479. https://doi.org/10.1021/ar200331z.

(4) Gary, D. C.; Flowers, S. E.; Kaminsky, W.; Petrone, A.; Li, X.; Cossairt, B. M. Single-Crystal and Electronic Structure of a 1.3 Nm Indium Phosphide Nanocluster. *J. Am. Chem. Soc.* **2016**, *138* (5), 1510–1513. https://doi.org/10.1021/jacs.5b13214.

(5) Roy, X.; Lee, C.-H.; Crowther, A. C.; Schenck, C. L.; Besara, T.; Lalancette, R. A.; Siegrist, T.; Stephens, P. W.; Brus, L. E.; Kim, P.; et al. Nanoscale Atoms in Solid-State Chemistry. *Science* **2013**, *341* (6142), 157–160. https://doi.org/10.1126/science.1236259.

(6) Baker, R. T. K.; Sherwood, R. D. Catalytic Gasification of Graphite by Nickel in Various Gaseous Environments. *Journal of Catalysis* **1981**, *70* (1), 198–214.

(7) Baker, R. T. K.; Sherwood, R. D.; Derouane, E. G. Further Studies of the Nickel Graphite Hydrogen Reaction.Pdf. *Journal of Catalysis* **1982**, *75*, 382–395.

(8) Díaz-Fernández, D.; Méndez, J.; del Campo, A.; Mossanek, R. J. O.; Abbate, M.; Rodríguez, M. A.; Domínguez-Cañizares, G.; Bomatí-Miguel, O.; Gutiérrez, A.; Soriano, L. Nanopatterning on Highly Oriented Pyrolytic Graphite Surfaces Promoted by Cobalt Oxides. *Carbon* **2015**, *85*, 89–98. https://doi.org/10.1016/j.carbon.2014.12.049.

(9) Oberhuber, F.; Blien, S.; Schupp, F.; Weiss, D.; Eroms, J. Anisotropic Etching of Graphene in Inert and Oxygen Atmospheres: Anisotropic Etching of Graphene. *physica status solidi (a)* **2017**, *214* (2), 1600459. https://doi.org/10.1002/pssa.201600459.

(10) Campos, L. C.; Manfrinato, V. R.; Sanchez-Yamagishi, J. D.; Kong, J.; Jarillo-Herrero, P. Anisotropic Etching and Nanoribbon Formation in Single-Layer Graphene. *Nano Letters* **2009**, *9* (7), 2600–2604. https://doi.org/10.1021/nl900811r.

(11) Sarkar, S.; Bekyarova, E.; Niyogi, S.; Haddon, R. C. Diels−Alder Chemistry of Graphite and Graphene: Graphene as Diene and Dienophile. *J. Am. Chem. Soc.* **2011**, *133* (10), 3324–3327. https://doi.org/10.1021/ja200118b.

(12) Oh, S.; Gallagher, J. R.; Miller, J. T.; Surendranath, Y. Graphite-Conjugated Rhenium Catalysts for Carbon Dioxide Reduction. *Journal of the American Chemical Society* **2016**, *138* (6), 1820–1823. https://doi.org/10.1021/jacs.5b13080.

(13) Celis, A.; Nair, M. N.; Taleb-Ibrahimi, A.; Conrad, E. H.; Berger, C.; Heer, W. A. de; Tejeda, A. Graphene Nanoribbons: Fabrication, Properties and Devices. *J. Phys. D: Appl. Phys.* **2016**, *49* (14), 143001. https://doi.org/10.1088/0022-3727/49/14/143001.

(14) Elías, A. L.; Botello-Méndez, A. R.; Meneses-Rodríguez, D.; Jehová González, V.; Ramírez-González, D.; Ci, L.; Muñoz-Sandoval, E.; Ajayan, P. M.; Terrones, H.; Terrones, M. Longitudinal Cutting of Pure and Doped Carbon Nanotubes to Form Graphitic Nanoribbons Using Metal Clusters as Nanoscalpels. *Nano Letters* **2010**, *10* (2), 366–372. https://doi.org/10.1021/nl901631z.

(15) Raza, H.; Kan, E. C. Armchair Graphene Nanoribbons: Electronic Structure and Electric-Field Modulation. *Physical Review B* **2008**, *77* (24). https://doi.org/10.1103/PhysRevB.77.245434.

(16) Verzhbitskiy, I. A.; Corato, M. D.; Ruini, A.; Molinari, E.; Narita, A.; Hu, Y.; Schwab, M. G.; Bruna, M.; Yoon, D.; Milana, S.; et al. Raman Fingerprints of Atomically Precise Graphene Nanoribbons. *Nano Letters* **2016**, *16* (6), 3442–3447. https://doi.org/10.1021/acs.nanolett.5b04183.

(17) Chu, X.; Schmidt, L. D. Gasification of Graphite Studied by Scanning Tunneling Microscopy. *Carbon* **1991**, *29* (8), 1251–1255.

(18) *Fundamental Issues in Control of Carbon Gasification Reactivity*; Lahaye, J., Ehrburger, P., Eds.; Springer Netherlands: Dordrecht, 1991. https://doi.org/10.1007/978-94-011-3310-4.

(19) Datta, S. S.; Strachan, D. R.; Khamis, S. M.; Johnson, A. T. C. Crystallographic Etching of Few-Layer Graphene. *Nano Letters* **2008**, *8* (7), 1912–1915. https://doi.org/10.1021/nl080583r.

(20) Jin, J. E.; Lee, J.-H.; Choi, J. H.; Jang, H.-K.; Na, J.; Whang, D.; Kim, D.-H.; Kim, G. T. Catalytic Etching of Monolayer Graphene at Low Temperature via Carbon Oxidation. *Phys. Chem. Chem. Phys.* **2016**, *18* (1), 101–109. https://doi.org/10.1039/C5CP03139G.

(21) Wang, R.; Wang, J.; Gong, H.; Luo, Z.; Zhan, D.; Shen, Z.; Thong, J. T. L. Cobalt-Mediated Crystallographic Etching of Graphite From Defects. *Small* **2012**, *8* (16), 2515–2523. https://doi.org/10.1002/smll.201102747.

(22) Stevens, F.; Kolodny, L. A.; Beebe, T. P. Kinetics of Graphite Oxidation: Monolayer and Multilayer Etch Pits in HOPG Studied by STM. *The Journal of Physical Chemistry B* **1998**, *102* (52), 10799–10804. https://doi.org/10.1021/jp982025e.

(23) Melinte, G.; Moldovan, S.; Hirlimann, C.; Baaziz, W.; Bégin-Colin, S.; Pham-Huu, C.; Ersen, O. Catalytic Nanopatterning of Few-Layer Graphene. *ACS Catalysis* **2017**, 5941–5949. https://doi.org/10.1021/acscatal.7b01777.

(24) Melinte, G.; Florea, I.; Moldovan, S.; Janowska, I.; Baaziz, W.; Arenal, R.; Wisnet, A.; Scheu, C.; Begin-Colin, S.; Begin, D.; et al. A 3D Insight on the Catalytic Nanostructuration of Few-Layer Graphene. *Nature Communications* **2014**, *5*, 1–8. https://doi.org/10.1038/ncomms5109.

(25) Baaziz, W.; Melinte, G.; Ersen, O.; Pham-Huu, C.; Janowska, I. Effect of Nitriding/Nanostructuration of Few Layer Graphene Supported Iron-Based Particles; Catalyst in

Graphene Etching and Carbon Nanofilament Growth. *Physical Chemistry Chemical Physics* **2014**, *16* (30), 15988. https://doi.org/10.1039/C4CP01887G.

(26) Yin, Y.; Erdonmez, C. K.; Cabot, A.; Hughes, S.; Alivisatos, A. P. Colloidal Synthesis of Hollow Cobalt Sulfide Nanocrystals. *Advanced Functional Materials* **2006**, *16* (11), 1389–1399. https://doi.org/10.1002/adfm.200600256.

(27) Puntes, V. F.; Krishnan, K. M.; Alivisatos, A. P. Colloidal Nanocrystal Shape and Size Control: The Case of Cobalt. *Science* **2001**, *291* (5511), 2115–2117.

(28) Wang, X.; Li, X.; Yoon, Y.; Weber, P. K.; Wang, H.; Guo, J.; Dai, H. N-Doping of Graphene Through Electrothermal Reactions with Ammonia. *Science* **2009**, *324* (5928), 768–771. https://doi.org/10.1126/science.1170335.

(29) Li, X.; Wang, H.; Robinson, J. T.; Sanchez, H.; Diankov, G.; Dai, H. Simultaneous Nitrogen Doping and Reduction of Graphene Oxide. *Journal of the American Chemical Society* **2009**, *131* (43), 15939–15944. https://doi.org/10.1021/ja907098f.

Appendix: Standard Operating Procedure for Microtime200 Confocal Fluorescence Microscope

TABLE OF CONTENTS

1. Before Measuring

1.1. Power on Microscope

1.1.1. Flip Green switch to power on control panel and TCSPC electronics. Turn adjacent key to turn on laser.

1.1.1.1. **Do not** adjust laser intensity on the Picoquant box, use the screw on top of the laser diode

1.1.2. Turn on the detectors:

1.1.2.1. Remove cover from optical box

1.1.2.2. On control panel, hit top row 1 and 2 to turn on detectors 1 and 2. Watch as the green LED on each detector lights up and shuts off.

1.1.2.3. The LED light under the buttons sometimes doesn't turn on, check the intensity counts to see if the detector is actually on.

1.2. Software

1.2.1. On computer desktop, open SymPhoTime 64

1.2.2. Before any measurements can be made a new workspace must be created to store data

1.2.2.1. Go to File > New Workspace

1.2.2.2. Enter workspace name (software will create folder called workspacename.sptw)

1.2.2.3. Choose a logical naming convention. I used YYYYMMDD_optionaldescription.sptw (e.g. 20190823_blinkingStudy.sptw, or just 20190823.sptw)

1.2.3. Don't include the space character in workspace or file names, use either underscores or capitalLettersLikeThis

1.3. Miscellaneous Notes

1.3.1. You can perform either T3 (lifetime) or T2 (correlation) measurements by changing software settings and unplugging the TCSPC cable (for T2). this is important for SymPhoTime data analysis but is *detrimental* for python data analysis. We will perform all measurements in T3 mode and convert for correlation analysis later.

1.3.2. The air table pressure must be above 1,000 kPa (~140 psi) to float. Floating air table is necessary for stable measurements!

1.3.3. The Microtime200 manual provided by Picoquant is very good. Consult it before doing measurements.

2. Alignment

2.1. Types of alignment

2.1.1. The **fundamental alignment** is very time-intensive, and should only be done as a last resort if something is wrong with the microscope. The Picoquant provided manual has a very good walk through, but try to avoid doing this!

2.1.2. **Daily alignment** is easier, and should be done routinely. The Picoquant manual has a very good walk through if you're confused.

2.2. Alignment using mirror

2.2.1. Prepare a fresh lens paper with a drop or two of ethanol and wipe objective *once* to remove dust.

2.2.2. Add a drop of oil to top of the objective, ensure no air bubbles are in oil.

2.2.3. Use focus knob to lower objective below microscope stage.

2.2.4. place mirror over the objective hole and secure with holding pins. Raise the objective using the focus knob until it touches the mirror.

2.2.5. Place the black-out box over the objective/mirror lens.

2.2.6. Remove cover from optical box.

2.2.7. Have the detector beam cube control rod pulled 1/2 way out so that both detectors are in use.

2.2.8. On the side of the optical box, there are two knobs. Adjust the one closest to the microscope so that "OD3" is on top—this adjusts the filter wheel so that the light passes through an neutral density filter

2.2.9. In the SymPhoTime software, open the "Camera" tab to get an image of the beam (it will probably be completely dark)

2.2.10. Open the excitation shutter on the control panel to allow laser light into the microscope objective.

2.2.11. On the microscope, adjust the fine focus knob until you find the laser reflection (bright white spot) on the ccd camera. A well focused beam should be a tight circle, with no rings.

2.2.12. On SymPhoTime, select “test” tab, then choose “point/time trace” then click “Run”

2.2.13. Adjust the fine focus to maximize signal.

2.3. Pinhole adjustment

2.3.1. Stop any running measurements or tests and ensure the excitation shutter is closed on the control panel.

2.3.2. If needed, replace pinhole by sliding tube towards the microscope and gently unscrewing the pinhole.

2.3.3. After replacing pinhole and sliding back tube so that the laser path is not exposed, begin test measurement on mirror as described in 2.2.

2.3.4. Adjust knobs on top and side facing away from user of pinhole to maximize signal

2.3.5. Adjust focus to maximize signal

2.3.6. Repeat steps 2.3.4-2.3.5 until signal can no longer be maximized.

2.3.7. If there is no signal, the pinhole may be far away from correct alignment. Replace pinhole with largest size available and try again. If problem persists,

check Picoquant manual for instructions on aligning the pinhole/detector lens that are far out of alignment. Patience may be required.

2.4. Detector lens adjustment

2.4.1. To maximize detection, there is a lens in front of both SPAD detectors. These should be adjusted as part of daily alignment.

2.4.2. If the intensity signal of the two different detectors (green and blue lines on SymPhoTime time trace) are different, the detector lenses need to be adjusted.

2.4.3. The Picoquant manual has more detailed instructions. It is a good manual!

2.4.4. Begin test measurement as described in 2.2 and make sure objective is in focus

2.4.5. Adjust one knob at a time. Begin by adjust knob in one direction until the signal goes to zero, use smooth turning motion. Remember the position of the knob (note the white dot on the knob, it can be helpful to remember the position as the "time" on the face of a clock)

2.4.6. Adjust knob in opposite direction until signal recovers to maximum, continue the same direction until intensity goes to zero, use smooth turning motion. Remember the position of the knob.

2.4.7. Move knob position exactly in between the previous to remembered positions (e.g. if the intensity was zero at 9:00 counterclockwise and at 3:00 clockwise, set the knob to 12:00).

2.4.8. Repeat steps 2.4.4-2.4.7 for the second knob on the detector, then begin the same process on the second detector

3. Measuring Solutions

3.1. Pre-measurement

3.1.1. Before any measurements are made ensure that 1) microscope is well aligned 2) the optical box is covered 3) the filter wheel closest to the microscope is set to "Filter 2" on top. This is the 450 nm LP filter and measurements **can not** be made without it in place.

3.1.2. This section will focus on using *volatile* solvents, like hexanes and toluene, often used for nanocrystal solutions by the Owen lab. For water soluble fluorophores the procedure is much easier.

3.1.3. Sample concentration is the most important sample prep design parameter, for lifetime measurements, something close to UV/Vis aliquot concentration is fine (i.e. lightly colored solutions). For FCS measurements, any visible color is way too concentrated!

3.2. Volatile solvent measurements

3.2.1. Fill rectangular vitricom capillary with desired solution. Plug both ends of capillary with capillary clay.

3.2.2. Prepare a fresh lens paper with a drop or two of ethanol and wipe objective *once* to remove dust.

3.2.3. Add a drop of oil to top of the objective, ensure no air bubbles are in oil.

3.2.4. Use focus knob to lower objective below microscope stage.

3.2.5. place capillary over the objective hole and secure with holding pins. Raise the objective using the focus knob until it contacts the capillary. Ensure the center of the objective is in the center of the capillary width.

3.2.6. Place the black-out box over the objective/mirror lens.

3.2.7. Open the excitation shutter on the control panel to allow laser light into the microscope objective.

3.2.8. On the microscope, adjust the fine focus knob until you find the laser reflection (bright white spot) on the ccd camera. A well focused beam should be a tight circle, with no rings.

3.2.9. There should be two major reflections from a capillary. The interface between the top of the bottom of the capillary and the solvent, and the interface between the solvent and the bottom of the top of the capillary. The reflections should be a little more than 1 complete rotation of the fine focus knob. This can be tricky!

3.2.10. To better find the correct focus of the capillaries, select “test” tab, then choose “point/time trace” then click “Run”

3.2.11. Slowly move the focus from below the capillary, through it, and above it, you should see 1) low intensity before the capillary 2) a sharp spike in the time trace intensity corresponding to a reflection on the ccd camera 3) lower intensity (depending on the sample concentration) 4) another spike in intensity and reflection on the ccd camera at the top of the capillary.

3.2.12. Using a live lifetime decay histogram is also useful. Select the “TCSPC” tab above the data instead of the “Time Trace”. You should see the characteristic lifetime decay of your fluorophore (generally longer than the instrument

response) only when you are *within* the capillary. Use this to determine when you are actually measuring your sample.

3.2.13. Place focus *between* the reflections you have found. Most importantly be consistent!

3.2.14. Click “Measurement” tab to perform point/time trace measurement after you have focused and set up the correct laser intensity/rep-rate for your measurement in test mode. You should not perform mapping measurements on liquid.

3.2.15. The laser power and rep rate are important parameters to consider for experiment design. Every measurement requires different conditions. Please check Section 7: Common mistakes and rules of thumb for QD TCSPC Measurements for tips on experiment design.

3.3. Aqueous and non-volatile solvent measurements

3.3.1. Prepare a fresh lens paper with a drop or two of ethanol and wipe objective *once* to remove dust.

3.3.2. Add a drop of oil to top of the objective, ensure no air bubbles are in oil.

3.3.3. Use focus knob to lower objective below microscope stage.

3.3.4. place clean #1 glass slide over the objective hole and secure with holding pins. Raise the objective using the focus knob until it contacts the slide.

3.3.5. Deposit solution on top of glass slide. Ensure solution is covering objective.

3.3.6. Place the black-out box over the objective/mirror lens.

3.3.7. Open the excitation shutter on the control panel to allow laser light into the microscope objective.

3.3.8. On the microscope, adjust the fine focus knob until you find the laser reflection (bright white spot) on the ccd camera. A well focused beam should be a tight circle, with no rings.

3.3.9. There should be one strong reflection (the interface of the top of the slide and the solvent) and one weak reflection (the interface of the oil and the bottom of the slide).

3.3.10. select “test” tab, then choose “point/time trace” then click “Run”.

3.3.11. Focus on the strong reflection, and move up using the focus knob. There should be no drop in intensity or change in lifetime decay.

3.3.12. Place focus within solution. Most importantly be consistent!

3.3.13. Click “Measurement” tab to perform point/time trace measurement after you have focused and set up the correct laser intensity/rep-rate for your measurement in test mode. You should not perform mapping measurements on liquid.

3.3.14. The laser power and rep rate are important parameters to consider for experiment design. Every measurement requires different conditions. Please check Section 7: Common mistakes and rules of thumb for QD TCSPC Measurements for tips on experiment design.

4. Measuring Solids

4.1. Pre-Measurement

4.1.1. Before any measurements are made ensure that 1) microscope is well aligned 2) the optical box is covered 3) the filter wheel closest to the microscope is set to

"Filter 2" on top. This is the 450 nm LP filter and measurements **can not** be made without it in place.

4.1.2. This section will focus on using *volatile* solvents, like hexanes and toluene, often used for nanocrystal solutions by the Owen lab. For water soluble fluorophores the procedure is much easier.

4.1.3. Many solid photoluminescent samples may be measured. We'll focus on solution deposited QDs and other fluorophores since that is the focus of the Owen lab.

4.1.4. Sample concentration is an important sample prep design parameter. For spin coated or drop-casted samples, UV/Vis aliquot concentration is too high. Any visible color is likely too concentrated to find single particles. Dilute UV/Vis concentrations ~100-1000 times in 0.5% w/w polymer (PMMA, polystyrene) and co deposit using spin coater.

4.1.5. If not spin coating, drop-casting a diluted UV/Vis concentration usually works too.

4.1.6. Use only #1 glass microscope slides, since they have the correct thickness. Circular slides fit nicely into our sample holder, which maybe reduces drift. Rectangular slides fit directly onto stage. There is also a sample holder for square slides.

4.2. *QD/fluorophore on glass substrate mapping*

4.2.1. Prepare a fresh lens paper with a drop or two of ethanol and wipe objective *once* to remove dust.

4.2.2. Add a drop of oil to top of the objective, ensure no air bubbles are in oil.

4.2.3. Use focus knob to lower objective below microscope stage.

4.2.4. place glass slide with QDs/fluorophores **on the top side** over the objective hole and secure with holding pins. Raise the objective using the focus knob until it contacts the slide.

4.2.5. Place the black-out box over the objective/mirror lens.

4.2.6. Open the excitation shutter on the control panel to allow laser light into the microscope objective.

4.2.7. On the microscope, adjust the fine focus knob until you find the laser reflection (bright white spot) on the ccd camera. A well focused beam should be a tight circle, with no rings.

4.2.8. There should be one strong reflection (the interface of the top of the slide and the air) and one weak reflection (the interface of the oil and the bottom of the slide).

4.2.9. Focus on the strong reflection on top of the slide

4.2.10. Have the detector beam cube control rod pulled 1/2 way out so that both detectors are in use. This is necessary for antibunching/cross correlation measurements, and can also be useful for finding particles.

4.2.11. select “test” tab, then choose “imaging.”

4.2.12. Click “max range” and check that the “fast” tab is selected. Click “start”

4.2.13. After imaging scan has finished, click “select range” and draw a box around a dark area near bright particles. At this scale any bright spots will be *collections* or aggregates of fluorophore, not single particles. The single particles are emitting light faintly and appear dark.

4.2.14. Repeat 4.2.13 until candidate single particles have been found. After 1 or 2 times zooming in, you should change to “accurate” tab to get better images.

4.2.15. You may also want to adjust the intensity slider using the pop out menu with 11 arrows next to the images to better see regions of lower intensity.

4.3. QD/fluorophore on glass point measurements

4.3.1. When a particle of interest is identified click “point/time trace” then “select point” click on the particle on the map and click “start” while still in test mode.

4.3.2. Analyze lifetime decay trace to ensure the particle has reasonable or expected lifetime (i.e. it is not the laser/instrument response from scattering or dust or something)

4.3.3. Optimize time trace intensity by adjusting focus knob.

4.3.4. Stop test measurement, click “measurement” tab. Click “point/time trace” and click “start”

5. After Measurement

5.1. Removing Sample

5.1.1. After measurements finish, the excitation shutter *should* automatically turn off. Double check the control panel that the excitation shutter is closed.

5.1.2. Remove holding pins from sample.

5.1.3. Lower microscope objective using focus knob until sample is detaches.

5.1.4. Lift sample and wipe bottom with lens paper

5.1.5. Gently wipe objective with dry lens paper, then prepare a fresh lens paper with a drop or two of ethanol and wipe objective *once*.

5.1.6. Lower microscope objective below stage and place black-out box on top.

5.2. Power off Microscope

5.2.1. Save any calculations and shut down SymPhoTime software *before* turning off microscope.

5.2.2. Flip Green switch to power off control panel and TCSPC electronics. Turn adjacent key to turn off laser. **Do Not** adjust anything else.

5.2.3. Data can be saved to a flash drive or cloud storage. The .sptw workstations are just folders that contain .ptu and other Picoquant files. Copy the desired .sptw folder.

5.2.4. Any graph produced in SymPhoTime can be exported as a .dat (similar to .csv, readable by excel, if any problems occur literally change the name to .csv instead of .dat) by right clicking and selecting "Export ASCII".

5.2.5. Maps and images can be exported as bitmaps by right clicking and selecting "export" > "Bitmap" or other options.

6. Data Analysis

6.1. The SymPhoTime software is capable of performing many data analysis techniques, however the python script provided (qdTCSPC.py) is more complete, more flexible, and allows for time gating which is very important for measuring QDs.

6.2. Refer to the source code below or at github.com/trevhull, which contains instructions on using the python script.

7. Common mistakes and rules of thumb for QD TCSPC Measurements

7.1. Sample preparation

7.1.1. If your spin coating solution is not colorless, it is too concentrated.

7.1.2. 0.5% to 1% w/w polymer solution is probably sufficient for co-deposition

7.2. Alignment

7.2.1. Many issues can be resolved by re-aligning the pinhole

7.2.2. Use the Picoquant manual guide for alignment. The laser and mirror work great

7.2.3. Remember to change filter 2 to OD 3 when using the laser and mirror

7.2.4. Remember to change **back** to filter 2 after alignment

7.2.5. If the two detector intensities are not the same level, align the lenses in front of the detectors (see Picoquant manual)

7.2.6. Pray you never have to do a fundamental alignment (see Picoquant manual)

7.3. Lifetime Measurements

7.3.1. The rep rate should reflect a window time at least **4** times greater than the longest lifetime measured (e.g. if longest lifetime component is 100 ns, window must be 400 ns to properly decay, so set laser rep rate no faster than 2.5 MHz)

7.3.2. For PL decays longer than ~10 ns tail fitting is probably fine

7.3.3. Lifetime measurements should be made at count rate of 1-5% of rep rate

7.3.4. In fact, generally choose the lowest count rate that has distinct signal (should appear ~monoexponential on live histogram view)

7.3.5. Lifetime intensity should be between 10^4 and 10^5 counts at peak

7.4. Substrate Measurements

7.4.1. For blinking the laser power should be around 2 au, at least below 10au, depending on the signal/noise of the QD

7.4.2. To find single particles when mapping, you must zoom in and use accurate mode

7.4.3. Streaks in maps are due to blinking, discolored horizontal bars are due to change in the TSCPC resolution (uncheck the "auto" box next to TCSPC resolution)

7.4.4. Generally, look for dark areas, not areas where fluorescence is obvious. The brightest areas are groups of multiple QDs, guaranteed. If you're having trouble look around bright areas for single QDs.

7.5. General troubleshooting tips

7.5.1. Ensuring there were no filters put in place during previous experiments is a helpful troubleshooting step that may save the user pain and frustration.

7.5.2. Remember also that the 450nm long pass filter (Filter 2 on the filter wheel) is required to measure photoluminescence, instead of reflected laser light (but obviously should not be in place when deliberately measuring reflected laser light)

8. qdTCSPC.py Source code

```
#!/usr/bin/env python3
# -*- coding: utf-8 -*-
"""
Created on Tue May 22 13:16:51 2018

@author: Trevor Hull
www.trevorhull.com
github.com/trevhull

"""

#import os
import numpy as np
import matplotlib.pyplot as plt
from phconvert import pqreader
import pycorrelate as pyc
from scipy.optimize import curve_fit
from matplotlib.gridspec import GridSpec
from scipy.integrate import simps
#import PySimpleGUI as sg

def monoexfit(x, a, b, e):
    '''
    (a*(np.exp((-(x/b)))))+e

    '''
    return (a*(np.exp((-(x/b)))))+e

def biexfit(x, a, b, c, d, e):
     return (a*(np.exp((-(x/b)))))+(c*(np.exp((-(x/d)))))+e

def triexfit(x, a, b, c, d, e, f, g):
     return (a*(np.exp((-(x/b)))))+(c*(np.exp((-(x/d)))))+(e*(np.exp((-(x/f)))))+g

def truncpowerfunc(x, a, b, c, d):
    return (a*(x**(-b)))*(d*(np.exp(-x/c)))

def powerfunc(x, a, b):
    return a*(x**(-b))

class ptu:
```

```
    def __init__(self, path, file):

        self.path = path
        self.name = file


    #def loadptu(self):
        filename = self.path + self.name
        timestamps, detectors, nanotimes, self.meta = pqreader.load_ptu(filename)
        nanotimes = nanotimes[detectors !=127]
        timestamps = timestamps[detectors !=127]
        detectors = detectors[detectors !=127]

        self.cins =
int(round(1/self.meta['nanotimes_unit']/self.meta['tags']['TTResult_SyncRate']['value']))


          #This is here because there's some problem in picoquant's record taking where you get
          #photon counts in your lifetime measurement that are impossibly long, i.e. they are longer
          #then the time between laser pulses. I'm not 100% sure why this happens but I think it
          #has something to do with the tcspc resolution. However, you should be careful about the
          #way python converts integers in cins because sometimes if cins = 3999.999 the int
rounding
          #will make it 3999. so make sure cins has round() in it
        self.timestamps = timestamps[nanotimes<self.cins]
        self.detectors = detectors[nanotimes<self.cins]
        self.nanotimes = nanotimes[nanotimes<self.cins]

        # Need some units to get to truetime aka T2, timestamps_unit & nanotimes)unit also
provided by pqreader
        self.truetime =
(((self.timestamps*self.meta['timestamps_unit'])+(self.nanotimes*self.meta['nanotimes_unit'])))
        #longtime is gonna be out cutoff, last value of truetime. might not actually need it for this
program ...
        self.longtime = self.truetime[-1]
        '''
        file_dict = {'longtime': longtime,
              'truetime': truetime,
              'timestamps':timestamps,
              'detectors':detectors,
              'nanotimes':nanotimes,
              'meta':meta}

        self.file_dict = file_dict
        '''
```

```
        return #file_dict

    def window(self, lowerBound, upperBound):
        '''
        Create a new ptu object that only contains photons during some duration
        of the experiment between lowerBound and upperBound
        '''
        newself = ptu(self.path, self.name)

        newself.timestamps = newself.timestamps[(newself.truetime > lowerBound) &
(newself.truetime < upperBound)]
        newself.nanotimes = newself.nanotimes[(newself.truetime > lowerBound) &
(newself.truetime < upperBound)]
        newself.detectors = newself.detectors[(newself.truetime > lowerBound) &
(newself.truetime < upperBound)]
        newself.truetime = newself.truetime[(newself.truetime > lowerBound) & (newself.truetime
< upperBound)]

        newself.longtime = newself.truetime[-1]

        print('data has been truncated between ' + str(lowerBound) + ' and ' + str(upperBound) +'
seconds')

        return newself

    def lifetime(self, fitFunc):
        #meta = self.meta
        bins = int(1/self.meta['nanotimes_unit']/self.meta['tags']['TTResult_SyncRate']['value'])
        nanotimes = self.nanotimes
        lifeIntensity, lifeBin_ = np.histogram(nanotimes, bins)
        lifeBins = lifeBin_[:(len(lifeBin_))-1]*self.meta['nanotimes_unit']*1e6
        #fig = plt.figure(figsize=(3,2))
        #ax1 = plt.subplot(1,1,1)
        #ax1.set_yscale('log')
        #plt.plot(bubin, plint)
        #plt.xlabel('time ($\mu$s)')
        #plt.ylabel('intensity (counts)')
        #plt.show()


        self.lifeBins = lifeBins
        self.lifeIntensity = lifeIntensity

        return# plint, bubin

    def lifePlot(self, fitFunc, lifeBound):
```

```
    '''
    '''
    self.lifetime(fitFunc)
    plt.figure(figsize=(5,4))
    ax1 = plt.subplot(1,1,1)
    ax1.set_yscale('log')
    plt.plot(self.lifeBins, self.lifeIntensity, '.')

    if fitFunc == monoexfit:
        self.fitMono(lifeBound)
    elif fitFunc == biexfit:
        self.fitBi(lifeBound)
    elif fitFunc == triexfit:
        self.fitTri(lifeBound)
    else:
        print('not a valid fit, sorry')

    plt.plot(self.fitBins, fitFunc(self.fitBins, *self.lifepopt), 'r')



    plt.xlabel('time ($\mu$s)')
    plt.ylabel('intensity (counts)')




    plt.show()
    #print(popt)


    return

def calcBlink(self, resolution):
    '''
    '''
    bins = int(self.longtime/resolution)
    blinkY,cins = np.histogram(self.truetime,bins)
    blinkX = cins[:(len(cins)-1)]

    freqX, dins = np.histogram(blinkY, 1000)
    freqY = dins[:(len(dins)-1)]

    self.blinkX = blinkX
    self.blinkY = blinkY
```

```
        self.freqX = freqX
        self.freqY = freqY
        self.blinkRes = resolution


        return #file_dict

    def plotBlink(self, resolution):
        '''
        plot some damn blinking
        '''
        self.calcBlink(resolution)
        plt.figure(figsize=(16,8))
        gs = GridSpec(2, 5)
        # identical to ax1 = plt.subplot(gs.new_subplotspec((0, 0), colspan=3))
        ax1 = plt.subplot(gs[0, :-1])
        ax1.tick_params(labelleft=True)
        plt.xlim(min(self.blinkX),self.longtime)
        plt.xlabel('Time (sec)', fontsize=12)
        plt.ylabel('Intensity (Counts)', fontsize=12)
        plt.plot(self.blinkX, self.blinkY)
        ax2 = plt.subplot(gs[0, -1])
        plt.xlabel('frequency (counts)', fontsize=12)
        plt.plot(self.freqX, self.freqY)
        ax2.tick_params(labelleft=False)
        plt.show()
        return #blinkX, blinkY, freqX, freqY
    '''
    def digitize(self, threshold):
        i = 0

        off = np.zeros(len(self.blinkY))
        for i in range(0,len(self.blinkY)):
            if self.blinkY[i] > threshold:
                off[i] = 1
            else:
                off[i] = 0

        self.digital = off
        self.threshold = threshold
        return #blink_dict
    '''
    def digitize(self, *threshold):
        i = 0

        off = np.empty(len(self.blinkY)) * np.NaN
```

```
#print(threshold)
for j in range(0,len(threshold)):

    '''
    if type(threshold[j]) != tuple:
        print('this is not my beautiful tuple')
        fixThreshold = (min(self.blinkY), threshold[j]), (threshold[j], max(self.blinkY))
        for i in range(0,len(self.blinkY)):
            if (self.blinkY[i] > fixThreshold[j][0]) & (self.blinkY[i] < fixThreshold[j][1]):
                off[i] = j
                #print(j)
            else:
                pass

    if type(threshold[j]) != tuple:
        print('this is not my beautiful tuple')
        fixThreshold = (min(self.blinkY), threshold[j]), (threshold[j], max(self.blinkY))

    '''

    if type(threshold[j]) == tuple:
        print(threshold[j])
        #print(j)
        for i in range(0,len(self.blinkY)):
            if (self.blinkY[i] > threshold[j][0]) & (self.blinkY[i] < threshold[j][1]):
                off[i] = j
                #print(j)
            else:
                pass

    else:
        print('this is not my beautiful tuple')
        #fixThreshold = (min(self.blinkY), threshold[0]), (threshold[0], max(self.blinkY))

        for i in range(0,len(self.blinkY)):
            if self.blinkY[i] > threshold[j]:
                off[i] = 1
            else:
                off[i] = 0

        threshold = ((min(self.blinkY), threshold[0]),(threshold[0], max(self.blinkY)))


self.digital = off
```

```
        self.threshold = threshold

        return #blink_dict



    def countDigital(self, choice):
    #NOTE: YOU NEVER ACTUALLY TYPE IN THIS COMMAND IT ALL GOES TO
digitallot
    #first get some info from our file dictionary
    #then we're gonna make 'timebin' which will hold the on/off time as we're counting, this will
end
    #up in an array later on

        if max(self.digital) == 1:
            timebin = 0
            n = len(self.blinkX)
            #generalized for on or off, depending on what you specify!
            for i in range(n-1):
                #remember you have to digitize before you can count! 1 is on, 0 is off
                if choice == 'off':
                    num = 0
                elif choice == 'on':
                    num = 1

                else:
                    print('bad choice! choose "on" or "off"')


                if (self.digital[i] == num):
                    timebin += 1
                elif (timebin == 0) & (self.digital[i]!=num):
                    pass
                else:
                    yield timebin
                    #print(timebin*0.01)
                    timebin = 0

        elif max(self.digital) == 2:
            timebin = 0
            n = len(self.blinkX)
            #generalized for on or off, depending on what you specify!
            for i in range(n-1):
                #remember you have to digitize before you can count! 1 is on, 0 is off
```

```
            if choice == 'off':
                num = 0
            elif choice == 'grey':
                num = 1
            elif choice == 'on':
                num = 2
            else:
                print('bad choice! choose "on" or "off" or maybe "grey"')


            if (self.digital[i] == num):
                timebin += 1
            elif (timebin == 0) & (self.digital[i]!=num):
                pass
            else:
                yield timebin
                #print(timebin*0.01)
                timebin = 0



    return #file_dict

def digitalPlot(self, choice, fitFunc):

    #blinkX = file_dict['blinkX']
    #digital = file_dict['digital']
    #choice = str(choice)
    choiceTime = np.fromiter(self.countDigital(choice), dtype=int)
    correctTime = choiceTime*self.blinkRes
    #digBins =  int(len(/0.08863636363636365)
    digBins =  int(self.longtime/self.blinkRes)
    statY, tatX = np.histogram(correctTime, bins = digBins)
    statX = (tatX[:(len(tatX)-1)])

    #to properly weight things we need to remove the zeros
    fixStatY = statY[statY!=0]
    probX = statX[statY!=0]

    #let's make an array the right length to save memory for our iteration
    probY = np.zeros(len(fixStatY))
    #So we need to weight each value by the probablity or the time distance (dt)
    #between nearest neighbors a and b
    for i in range(0,len(fixStatY)):
        if i == 0:
            dt = abs(probX[i+1] - probX[i])
```

```
            elif probX[i] == probX[-1]:
                dt = abs(probX[i-1] - probX[i])
            else:
                a = abs(probX[i-1] - probX[i])
                b = abs(probX[i+1] - probX[i])
                dt = (a+b)/2
            #then take the value fixStatY divide by the total # of records sum(fixStatY) * 1 /dt
            probY[i]= ((fixStatY[i]/sum(fixStatY))*(1/dt))


        #let's try and fit the data
        try:
            popt, pcov = curve_fit(fitFunc, probX, probY)
        except RuntimeError:
            print('fit error')
            pass

        ax = plt.subplot(1,1,1)
        ax.set_yscale('log')
        ax.set_xscale('log')
        plt.plot(probX, probY, 'o')
        try:
            plt.plot(probX, fitFunc(probX, *popt), 'r-')
        except UnboundLocalError:
            pass
        plt.show()

        if fitFunc == powerfunc:
            print('P(t) = ' + str(round(popt[0],2)) + '*tau^(-' + str(round(popt[1],2)) +')')
        elif fitFunc == truncpowerfunc:
            print('P(t) = ' + str(round(popt[0],2)) + 'xtau^(-' + str(round(popt[1],2)) + ')*' +
str(round(popt[2],2)) + 'e^(-tau/' + str(round(popt[3],2)) + ')')

        if choice == 'on':
            self.onProbX = probX
            self.onProbY = probY
            self.onpop = popt
        else:
            self.offProbX = probX
            self.offProbY = probY
            self.offpop = popt

        return #popt, probX, probY, digBins

    def calcDig(self, onfitFunc, offfitFunc):
        print('ON')
```

```
    self.digitalPlot('on',onfitFunc)
    print('OFF')
    self.digitalPlot('off',offfitFunc)
    return

def onFrac(self):
    self.onFrac = len(self.digital[self.digital==1])/len(self.digital)
    print(round(self.onFrac, 2))

    return

def offFrac(self):
    self.offFrac = len(self.digital[self.digital==0])/len(self.digital)
    print(round(self.offFrac, 2))

    return

def antibunching(self,samples,timegate):

    rep = self.meta['tags']['TTResult_SyncRate']['value']
    maxCorr = round(1/rep*1e6,1)+(round((1/rep*1e6)/2,1))
    l = -maxCorr*1e-6
    m = maxCorr*1e-6
    sp = samples
    p = (m-l)/sp
    lags = np.arange(l,m,p)
    self.antibunchX = (lags[:len(lags)-1])* 1e6

    correctNanotimes = self.nanotimes*self.meta['nanotimes_unit']
    a = self.truetime[(self.detectors==0)&(correctNanotimes>(timegate/1e9))]
    b = self.truetime[(self.detectors==1)&(correctNanotimes>(timegate/1e9))]

    self.G = pyc.pcorrelate(a, b, lags, 1)
    self.H = pyc.pcorrelate(b, a, lags, 1)
    self.antibunchY = (self.G + self.H)/2


    return self.antibunchY, self.antibunchX

def plotAB(self, samples, timegate):
    self.antibunching(samples, timegate)
    plt.plot(self.antibunchX, self.antibunchY)
    plt.xlabel('delay time ($\mu$s)')
    plt.ylabel('G[t]')
    plt.show()
```

```
def BXratio(self, bound):
    rep = round(1/self.meta['tags']['TTResult_SyncRate']['value']*1e6,1)
    lcbound = 0 - (bound/2)
    rcbound = 0 + (bound/2)
    lrbound = rep - (bound)
    rrbound = rep + (bound)

    cent = self.antibunchY[(self.antibunchX > lcbound) & (self.antibunchX < rcbound)]
    xcent = self.antibunchX[(self.antibunchX > lcbound) & (self.antibunchX < rcbound)]

    right = self.antibunchY[(self.antibunchX > lrbound) & (self.antibunchX < rrbound)]
    xright = self.antibunchX[(self.antibunchX > lrbound) & (self.antibunchX < rrbound)]

    area = simps(cent, xcent)
    rarea = simps(right, xright)
    self.bx = area/rarea
    #print(self.bx)
    return self.bx

def printBX(self, bound):
    self.BXratio(bound)
    print(self.bx)



#COME BACK AND WORK ON THIS
def loopBX(self, maxGateTime, inc, samples):
    '''
    maxGateTime



    '''
    i = 0

    rep = 1/(self.meta['tags']['TTResult_SyncRate']['value'])*1e6
    #maxCorr = rep+(rep/2)
    bound = rep/4

    tg = np.zeros((int(maxGateTime/inc)))
    bxarray = np.zeros((int(maxGateTime/inc)))
    for i in range(int(maxGateTime/inc)):
        I, plags = self.antibunching(samples, (i*inc))
        #bx = self.BXratio(bound)
        bxarray[i] = self.BXratio(bound)
```

```
            tg[i] = (i*inc)


        self.GDT = tg
        self.RTG = bxarray
        #plt.plot(tg,bxarray)

        plt.plot(self.GDT, self.RTG, 'o')

        plt.show()
        return #file_dict

    def crosstalk(self,samples, timegate):
        self.antibunching(samples, timegate)

        #l,m = antibunching_G(file_dict, samples, timegate)
        #n, o = antibunching_H(file_dict, samples,timegate)
        p = np.append(self.H[self.antibunchX<0],self.G[self.antibunchX>0])
        plt.figure(figsize=(3,3))
        plt.plot(self.antibunchX,p)
        plt.xlabel('correlation time ($\mu$s)')
        plt.ylabel('coincidences')
        plt.show()

        return #l,m,n,o,p

    def calcFlid(self, fitFunc):
        #nanotimes = file_dict['nanotimes']
        #truetime = file_dict['truetime']
        #blinkX = file_dict['blinkX']
        lifetime_resolution = 1

        self.flid = np.zeros(len(self.blinkX))
        i=0
        #banotimes = nanotimes[nanotimes<2500]
        while (i+1)*lifetime_resolution < len(self.blinkX):
            dtrins = self.nanotimes[(self.blinkX[(i*lifetime_resolution)]< self.truetime) &
(self.truetime < self.blinkX[(i +1)*lifetime_resolution])]
            #ax = plt.subplot(1,1,1)
            #ax.set_yscale('log')
            #print(i)
            #dbins = len(self.blinkX)
            dbins = int(round(len(self.blinkX)/10))
            #ax = plt.subplot(1,1,1)
            #ax.set_yscale('log')
            #plt.xlim
```

```
            #plt.show(plt.hist(dtrins, dbins, histtype = 'step'))
            a, bi = np.histogram(dtrins, dbins)
            bbins = bi[:(len(bi)-1)]*self.meta['nanotimes_unit']*1e6


            fa = a[bbins > 0.004]
            fbins = bbins[bbins > 0.004]
            try:
                popt, pcov = curve_fit(fitFunc, fbins, fa, bounds = (0,[100, 0.2, 100])) #4.44194979
0.14768228 39.53100168  0.05597095

            except RuntimeError:
                #print("Found an error")

                pass
            if fitFunc == biexfit:
                self.flid[i] = ((popt[0]*popt[1]) + (popt[2]*popt[3]))/(popt[0]+popt[2])
                #self.flid[i] = tave
            else:
                #tave = popt[1]
                self.flid[i] = popt[1]
            #plt.hist(dtrins, dbins, histtype = 'step')
            #plt.plot(fbins, *popt(fbins))
            #plt.show()
            #self.flid = flid
            i+=1
        return #

    def heatFlid(self, xlim):
        #self.flid = file_dict['flid']
        #blink_y = file_dict['blink_y']
        extent = [min(self.flid),xlim,min(self.blinkY),max(self.blinkY)]
        plt.hexbin(self.flid,self.blinkY,extent=extent,gridsize=80,bins='log')
        plt.xlim(0,xlim)
        plt.ylim(min(self.blinkY),max(self.blinkY))
        plt.xlabel('lifetime ($\mu$s)', fontsize=12)
        plt.ylabel('Intensity (Counts)', fontsize=12)
        plt.show()
        return

    def blinkLifetime(self):
        '''
        calculate lifetime histograms in a specified intensity range.
        Requires blinking trace and digitization.

        TODO:
```

```
        o generalization
        o separate calculation from plotting
        o calculate bins instead of name it


    '''
    #check which bins are 'on' (==1) and 'off' (==0) and assign each photon
    #in those bins the on/off 1/0 of the bin so we can gather up all nanotimes
    #for the lifetime fitting
    self.nanodigital = np.zeros(len(self.nanotimes))
    i = 0
    j = 0
    while self.blinkX[i] < self.blinkX[-1]:
        if self.truetime[j] > self.blinkX[i]:
                i+=1
        else:
            #if self.digital[i] == 0:
                #print('low')
            self.nanodigital[j] = self.digital[i]
            j+=1

           # if self.digital[i] == 1:
                #print('high')
            #    self.nanodigital[j] = 1
             #   j+=1

    #Calculate lifetime histograms
    #"ON" histogram
    dbins = 1000

    if max(self.nanodigital) == 1:

        self.onY, onX_needsTrim = np.histogram(self.nanotimes[self.nanodigital == 1],
dbins)#='auto')
        self.onX = onX_needsTrim[:(len(onX_needsTrim))-1]*self.meta['nanotimes_unit']*1e6

        #"OFF" histogram
        self.offY, offX_needsTrim = np.histogram(self.nanotimes[self.nanodigital == 0],
dbins)#='auto')
        self.offX = offX_needsTrim[:(len(offX_needsTrim))-1]*self.meta['nanotimes_unit']*1e6

    elif max(self.nanodigital) == 2:

        self.onY, onX_needsTrim = np.histogram(self.nanotimes[self.nanodigital == 2],
dbins)#='auto')
        self.onX = onX_needsTrim[:(len(onX_needsTrim))-1]*self.meta['nanotimes_unit']*1e6
```

```
        self.greyY, greyX_needsTrim = np.histogram(self.nanotimes[self.nanodigital == 1],
dbins)#='auto')
        self.greyX = greyX_needsTrim[:(len(greyX_needsTrim))-
1]*self.meta['nanotimes_unit']*1e6

        #"OFF" histogram
        self.offY, offX_needsTrim = np.histogram(self.nanotimes[self.nanodigital == 0],
dbins)#='auto')
        self.offX = offX_needsTrim[:(len(offX_needsTrim))-1]*self.meta['nanotimes_unit']*1e6



    return #onY, onX_corrected, offY, offX_corrected

  def plotBlinkLifetime(self, choice):
    '''
    print the blinking, frequencies, and lifetimes you calculated using BlinkLife

    '''
    #plotting:
    self.blinkLifetime()



    plt.figure(figsize=(16,4))
    gs = GridSpec(1, 8)
        # identical to ax1 = plt.subplot(gs.new_subplotspec((0, 0), colspan=3))
    ax1 = plt.subplot(gs[0, :4])
    plt.xlim(0,self.longtime)
    plt.ylim(0,max(self.blinkY + (self.blinkY*0.05)))
    plt.xlabel('time (sec)', fontsize=12)
    plt.ylabel('Intensity (Counts)', fontsize=12)
    #off
    ax1.axhspan(self.threshold[0][0],self.threshold[0][1], color='r', alpha = 0.5)
    #on
    ax1.axhspan(self.threshold[-1][0],self.threshold[-1][1], color='b', alpha = 0.5)

    if max(self.nanodigital) == 2:
      ax1.axhspan(self.threshold[-2][0],self.threshold[-2][1], color='g', alpha = 0.5)

    plt.plot(self.blinkX, self.blinkY, 'black')
    #plt.plot(self.blinkX[self.blinkY < 60], self.blinkY[self.blinkY < 60], 'r.')
    #plt.axhline(y=60, color='r', linestyle='--')
```

```
        ax2 = plt.subplot(gs[0, 4:5])
        plt.ylim(0,max(self.blinkY + (self.blinkY*0.05)))
        #plt.xlim(0,500)
        plt.xlabel('frequency (counts)', fontsize=12)
        ax2.axhspan(self.threshold[0][0],self.threshold[0][1], color='r', alpha = 0.5)
        #on
        ax2.axhspan(self.threshold[-1][0],self.threshold[-1][1], color='b', alpha = 0.5)

        if max(self.nanodigital) == 2:
            ax2.axhspan(self.threshold[-2][0],self.threshold[-2][1], color='g', alpha = 0.5)
        plt.plot(self.freqX, self.freqY, 'black')
        ax2.tick_params(labelleft=False)



        ax3 = plt.subplot(gs[0, -2:])
        plt.xlabel('time ($\mu$s)', fontsize=12)
        plt.ylabel('log intensity (counts)', fontsize=12)
        ax3.set_yscale('log')
        plt.plot(self.onX, (self.onY-min(self.onY))/max(self.onY), 'b.')#, histtype = 'step')
        plt.plot(self.offX, (self.offY-min(self.offY))/max(self.offY), 'r.')#, histtype = 'step')
        if max(self.nanodigital) == 2:
            plt.plot(self.greyX, (self.greyY-min(self.greyY))/max(self.greyY), 'g.')#, histtype = 'step')

        if choice == 1:

            try:
                fitonX = self.onX[self.onX > 0.008]
                fitonY = self.onY[self.onX > 0.008]
                popt, pcov = curve_fit(monoexfit, fitonX, fitonY, p0 =( 0.01, 0.03, 0.001))#, bounds =
(0,[1, 0.02, 1]))
                print(popt)
            except RuntimeError:
                print('this is not my beautiful fit!')

            plt.plot(fitonX, monoexfit(fitonX, *popt), 'r--')

        else:
            pass

        plt.show()

        return

    def fitTri(self, lifeBound):
        try:
```

```
            self.fitIntensity = self.lifeIntensity[self.lifeBins > lifeBound]
            self.fitBins = self.lifeBins[self.lifeBins > lifeBound]
            popt, pcov = curve_fit(triexfit, self.fitBins, self.fitIntensity, p0 =( 0.7, 0.070, .3, 0.03, 0.1,
0.01, self.lifeIntensity[-1]))
            #plt.plot(fitBins, fitFunc(fitBins, *popt), '-')
            self.lifepopt = popt
        except RuntimeError:
            print('unable to fit lifetime, sorry')
        return

    def fitBi(self, lifeBound):
        try:
            self.fitIntensity = self.lifeIntensity[self.lifeBins > lifeBound]
            self.fitBins = self.lifeBins[self.lifeBins > lifeBound]
            popt, pcov = curve_fit(biexfit, self.fitBins, self.fitIntensity, p0 =( 0.7, 0.070, .3, 0.01,
self.lifeIntensity[-1]))
            #plt.plot(fitBins, fitFunc(fitBins, *popt), '-')
            self.lifepopt = popt
        except RuntimeError:
            print('unable to fit lifetime, sorry')
        return

    def fitMono(self, lifeBound):
        try:
            self.fitIntensity = self.lifeIntensity[self.lifeBins > lifeBound]
            self.fitBins = self.lifeBins[self.lifeBins > lifeBound]
            popt, pcov = curve_fit(monoexfit, self.fitBins, self.fitIntensity, p0 =( 0.7, 0.070, .3))
            #plt.plot(fitBins, fitFunc(fitBins, *popt), '-')
            self.lifepopt = popt
        except RuntimeError:
            print('unable to fit lifetime, sorry')
        return

    def laser(self):
        au = self.meta['tags']['UsrPowerDiode']['value']
        opticalPower = 0.00391 * au
        print('laser power is ' + str(round(opticalPower,3)) + ' uW')
        self.opticalPower = opticalPower
        transmittance405 = 0.83
        fwhm = 250/1e9*100
        #powerDensity = 0.88*((opticalPower/1e6*transmittance405)/(fwhm**2))
        powerDensity = ((2*opticalPower/1e6*transmittance405)/(np.pi*(fwhm/1.18)**2))

        print('laser power density is ' + str(round(powerDensity,2)) + ' mW/cm^2')

        return
```

```
class blink(ptu):

    def __init__(self, path, file, resolution):
        ptu.__init__(self, path, file)
        self.path = path
        self.name = file
        #self = ptu(self.path,self.name)
        #self.loadptu()
        self.plotBlink(resolution)
        return
```